

NORTHWESTERN UNIVERSITY

Exploiting Protein Denaturation: Albumin Hydrogels Made by Electrostatic Partial Unfolding

A DISSERTATION

SUBMITTED TO THE GRADUATE SCHOOL  
IN PARTIAL FULFILLMENT OF THE REQUIREMENTS

for the degree

DOCTOR OF PHILOSOPHY

Field of Biomedical Engineering

By

Kevin Baler

EVANSTON, ILLINOIS

June 2014

© Copyright by Kevin Baler 2014

All Rights Reserved

## ABSTRACT

Exploiting Protein Denaturation: Albumin Hydrogels Made by Electrostatic Partial Unfolding

Kevin Baler

The study of protein denaturation and aggregation has a tremendous potential to spur important advances in several key biomedical fronts. For example, a better understanding of the factors influencing the folding and misfolding of proteins can help us develop new approaches for the treatment of neurodegenerative diseases such as Alzheimer's, Huntington's, Parkinson's, spongiform encephalopathies and systemic amyloidoses. But knowledge we gain from these efforts will stimulate the research and development of self-assembling biomaterials for novel commercial applications.

Because of its ubiquity and clinical potential, albumin is one of the best-characterized models in protein aggregation research; yet its properties under different conditions are not fully understood. In this work, we exploited an intrinsic denaturation mechanism of albumin to fabricate a new type of albumin hydrogel. This was achieved by altering the electrostatic charges on the albumin surface leading to interdomain repulsion that exposed buried hydrophobic regions. These regions drove new quaternary assemblies that promoted hydrogel formation while preserving some of the original protein functionality within unchanged protein domains.

Using all-atom molecular dynamics simulations we showed how electrostatic forces can affect the conformation of a single albumin molecule just prior to self-assembly. The results of these simulations suggest that hydrophobic attractions and counter ion binding interactions are key to understanding the formation of this particular hydrogel. In addition, we evaluated both

experimentally and computationally the residual binding affinity of the partially denatured albumin to all-trans Retinoic Acid, a cancer therapeutic with known affinity for normal albumin. This work provides critical new insights about the equilibrium conformation of albumin in its partially denatured state at low pH, and contributes significantly to our efforts to develop biocompatible protein hydrogel systems that are, driven by electrostatic partial denaturation and also exploit albumin's natural drug binding capacity.

## ACKNOWLEDGEMENTS

This dissertation, like many scientific endeavors, was only possible through the generous support and guidance of many dear colleagues, friends, and family. I owe a great deal of gratitude to this exemplary community and because of them, I will cherish my graduate experience forevermore.

I would like to first thank my research advisors, Dr. Igual Szleifer and Dr. Guillermo Ameer for their unfaltering support and confidence in my ability to work as a shared student in both their groups. I have been amazingly fortunate to have two advisors who gave me the freedom to explore on my own while also guiding me towards the completion of this dissertation. I would also like to take this opportunity to thank my committee members, Dr. Phil Messersmith and Dr. Kenneth Shull. I am thankful for their perceptive input and helpful advice along the way.

I also owe much to several past and current members of the Szleifer and Ameer labs. Rikkert Nap, Sung Hyun Park, Robert van Lith, Michele Jen, Marcelo Carignano, German Picasso, Claudio Narambuena, Mario Tagliazucchi, Greg Putzel, Gabriel Longo, Hiroaki Matsuda, Polina Pine, David Malaspina, Jian Yang, Bin Jiang, Zdravka Cankova, Sherry Zhu, Mazen Albaghadi, Anthony Costa, Doris Grillo, Ty Yacoub, Luay Alhamassa, Josephine Allen, Karen Lapidos, Conchi Serrano, Ryan Hoshi, Eunji Chung-Yoo, Antonio Webb. I have learned much from them through engaging conversations spanning almost every topic imaginable including European history, the intricacies of certain coding languages, deep board game strategy, interesting food pairing combinations, and many more topics. Their encouragement and lasting friendship remains a highlight of my experience at Northwestern.

I would also like to thank the others who made this work possible including; Katie Otim for her help in providing instrumentation and guidance during mechanical indentation experiments, Jorge Vila and Osvaldo Martin for developing the FAMBE-pH method and their insights into the molecular dynamics analysis, the Yerushalami-Rozen Group from Beersheva University and the Talmon research group at the Technion Israel Institute of Technology for instrumentation and guidance in obtaining Cryo-SEM images, and Miller Tsai for planting the seed of this project during his studies. To the undergraduates that worked with me, Sarah Ponte, Xing Li, and Raman Michael, whom I hope learned as much from me as I learned from them.

I would like to thank my parents Ruben and Adriana for their love and always encouraging me, but never telling me what to do (most of the time). Thanks to my sister Mila for helping me stay sane through years of graduate school. Lastly, I would like my thank my wife Amanda Messinger for her love and support over the last several years.

This work was supported in part by a NIH National Research Service Award from the National Institute of Biomedical Imaging and Bioengineering (1F31EB014698-01), by the Materials Research Science and Engineering Center program of the NSF (DMR-0520513) at Northwestern University, and by the Chemistry of Life Processes Institute. This work made use of the EPIC facility (NUANCE Center-Northwestern University), which has received support from the MRSEC program (NSF DMR-1121262) at the Materials Research Center, and the Nanoscale Science and Engineering Center (EEC-0118025/003), both programs of the National Science Foundation; the State of Illinois; and Northwestern University. This research was also supported by a grant from IMASL-CONICET PIP-112-2011-0100030 (JAV) and Project 328402 from the National University of San Luis (JAV), Argentina. Poisson

Boltzmann molecular graphics and analyses were performed with the UCSF Chimera package. Chimera is developed by the Resource for Biocomputing, Visualization, and Informatics at the University of California, San Francisco (supported by NIGMS P41-GM103311).

## LIST OF ABBREVIATIONS AND CHEMICAL NAMES

atRA – All-*trans* Retinoic Acid

$\beta$ -ME -  $\beta$ -Mercaptoethanol

BSA – Bovine Serum Albumin

CEVS – Controlled Environment Vitrification System

DMEM – Dulbecco's Modified Eagle Media

F-form Albumin – Fast conformation partially denatured albumin

FAMBE-pH – Fast adaptive multigrid boundary element analysis

HSA – Human Serum Albumin

LCFA – Long-chain fatty acids

N-form Albumin – Normal conformation folded albumin

OCT – Optimal Cutting Temperature (cryopreservative)

OsO<sub>4</sub> – Osmium Tetroxide

PBS – Phosphate Buffered Saline

PBSA – pH-induced BSA hydrogel

SDS – Sodium Dodecyl Sulfate

SEM – Scanning Electron Microscope

TBSA – Temperature-induced BSA hydrogel

TCP – Tissue Culture Plastic

TEM – Transmission Electron Microscope

## Table of Contents

<b>ABSTRACT .....</b>	<b>3</b>
<b>ACKNOWLEDGEMENTS.....</b>	<b>5</b>
<b>LIST OF TABLES .....</b>	<b>12</b>
<b>LIST OF FIGURES .....</b>	<b>13</b>
<b>CHAPTER 1: OVERVIEW .....</b>	<b>18</b>
1.1 MOTIVATION .....	18
1.2 THESIS OUTLINE .....	19
1.3 SPECIFIC AIMS .....	20
<b>CHAPTER 2: BACKGROUND .....</b>	<b>22</b>
2.1 HYDROGELS IN MEDICINE .....	22
2.2 BOVINE SERUM ALBUMIN .....	23
2.2.1 <i>BSA Composition</i> .....	23
2.2.2 <i>Secondary and Tertiary Structure</i> .....	24
2.2.3 <i>Disulphide Bonds</i> .....	25
2.2.4 <i>Charge Distribution</i> .....	26
2.2.5 <i>Binding Sites</i> .....	27
2.2.5.1 Sudlow's Site I.....	28
2.2.5.2 Sudlow's Site I.....	28
2.2.5.3 Additional albumin binding sites .....	29
2.2.5.4 All-trans Retinoic Acid albumin binding site .....	30
2.2.6 <i>Effect of pH</i> .....	32
2.2.6.1 N-F Transition.....	32
2.2.6.2 F-E Transition .....	33
2.2.7 <i>Effect of Temperature and Thermal Gelation</i> .....	34
2.2.8 <i>Additional Denaturing Mechanisms</i> .....	37
2.3 BSA GELATION SYSTEMS .....	37
2.4 CURRENT MEDICAL APPLICATIONS OF ALBUMIN.....	38
<b>CHAPTER 3: ELECTROSTATICALLY TRIGGERED PARTIAL DENATURATION OF ALBUMIN .....</b>	<b>40</b>
3.1 OBJECTIVE .....	40
3.2 EXPERIMENTAL SECTION .....	41
3.2.1 <i>Atomistic Bovine Serum Albumin Molecular Dynamics</i> .....	41
3.2.1.1 Initial protein homology determination .....	41
3.2.1.2 FAMBE-pH Calculations.....	42
3.2.1.3 Energy Minimization and molecular dynamics .....	43
3.2.1.4 Interdomain, interprotein, counter ion – residue distance calculation .....	44
3.2.1.5 Solvent accessible surface area calculation .....	44
3.2.2 <i>Circular Dichroism Experiments:</i> .....	45
3.2.3 <i>Electrostatic Potential Calculations</i> .....	45
3.3 RESULTS .....	45
3.3.1 <i>Protein protonation state at pH 3.5 .....</i>	46

	10
3.3.2 <i>Molecular dynamics simulation of partial protein unfolding</i> .....	47
3.3.3 <i>Secondary structure loss after partial unfolding</i> .....	51
3.3.4 <i>Hydrophobic solvent accessible surface area calculation</i> .....	53
3.3.5 <i>Preferential domain 3 unfolding during N-F transition</i> .....	55
3.3.6 <i>Dimeric protein interaction and molecular dynamics</i> .....	57
3.3.7 <i>Single protein electrostatic surface energy potential calculation</i> .....	58
3.3.8 <i>Two protein electrostatic surface energy potential calculation</i> .....	61
3.4 DISCUSSION .....	65
3.5 CONCLUSIONS.....	68
<b>CHAPTER 4: HYDROGEL FORMATION AND CHARACTERIZATION .....</b>	<b>69</b>
4.1 OBJECTIVE .....	69
4.2 EXPERIMENTAL SECTION .....	70
4.2.1 <i>BSA hydrogel fabrication</i> .....	70
4.2.1.1 <i>PBSA hydrogels</i> .....	70
4.2.1.2 <i>TBSA hydrogels</i> .....	71
4.2.2 <i>Hydrogel degradation</i> .....	71
4.2.3 <i>Transmission electron microscopy (TEM) Imaging</i> .....	72
4.2.4 <i>Scanning electron microscopy (SEM) Imaging</i> .....	72
4.2.5 <i>Cryo-SEM Imaging</i> .....	72
4.2.6 <i>Mechanical characterization of BSA gels</i> .....	73
4.2.7 <i>In vivo subcutaneous Rat model</i> .....	74
4.2.8 <i>Histology and evaluation of the subcutaneous implants</i> .....	75
4.3 RESULTS .....	76
4.3.1 <i>HCl-BSA titration curve</i> .....	76
4.3.2 <i>Fabrication of albumin hydrogels by electrostatically triggered self-assembly</i> .....	77
4.3.3 <i>PBSA and TBSA nanostructure observation via electron microscopy</i> .....	79
4.3.4 <i>Elastic modulus measurement by mechanical indentation</i> .....	82
4.3.4.1 Effect of ionic strength on Young's modulus .....	84
4.3.5 <i>PBSA acid neutralization and the effect of chemical environment on hydrogel integrity</i> .....	85
4.3.6 <i>In vivo biocompatibility evaluation</i> .....	87
4.4 DISCUSSION .....	90
4.5 CONCLUSIONS.....	93
<b>CHAPTER 5: FUNCTIONAL DOMAINS IN PROTEIN HYDROGELS .....</b>	<b>95</b>
5.1 OBJECTIVE .....	95
5.2 EXPERIMENTAL SECTION .....	97
5.2.1 <i>Molecular dynamics simulations</i> .....	97
5.2.2 <i>Potential of mean force calculation</i> .....	97
5.2.3 <i>atRA binding and release</i> .....	98
5.2.4 <i>Scratch test migration assay</i> .....	98
5.2.4.1 Data Analysis .....	99
5.2.5 <i>Hydrogel degradation after atRA loading</i> .....	99
5.3 RESULTS .....	100
5.3.1 <i>atRA binds to both F-form albumin and N-form albumin</i> .....	100
5.3.2 <i>atRA binding sites determined by molecular dynamics</i> .....	102
5.3.3 <i>Potential of mean force calculation for atRA binding to FSsite1 and NSite1</i> .....	107
5.3.4 <i>Released atRA inhibits HASMC migration</i> .....	109
5.3.5 <i>PBSA resistance to SDS and urea degradation due to atRA binding</i> .....	111
5.4 DISCUSSION .....	112

5.5 CONCLUSIONS.....	11 115
<b>CHAPTER 6: THESIS SUMMARY AND RECOMMENDATIONS .....</b>	<b>117</b>
6.1 SUMMARY OF THESIS WORK .....	117
6.2 RECOMMENDATIONS FOR FUTURE WORK.....	118
6.2.1 <i>Effect of urea on the binding of atRA to F-form albumin</i> .....	118
6.2.2 <i>F-form crystal structure for HSA and other drug interactions</i> .....	120
6.2.3 <i>F-form albumin microparticle fabrication for drug delivery</i> .....	121
6.2.4 <i>Summary and Outlook</i> .....	123
<b>REFERENCES .....</b>	<b>124</b>
<b>APPENDIX.....</b>	<b>145</b>
8.1 APPENDIX A: PYTHON SCRIPT TO CALCULATE ELECTROSTATIC SURFACE POTENTIAL .....	145
8.2 APPENDIX B: INTERSPECIES HOMOLOGY OF SERUM ALBUMINS .....	148
8.3 APPENDIX C: CHANGE IN DENATURATION TEMPERATURE WITH PH .....	149
8.4 APPENDIX D: PDB F-FORM BOVINE SERUM ALBUMIN .....	150
8.5 APPENDIX E: CIRCULAR DICHROISM OF ALBUMIN THERMAL DENATURATION. ....	151
8.6 APPENDIX G: SNAPSHOTS DURING ATRA – F-FORM ALBUMIN BINDING SIMULATION .....	152
8.7 APPENDIX H: SNAPSHOTS DURING ATRA – N-FORM ALBUMIN BINDING SIMULATION .....	153

## LIST OF TABLES

Table 2.1 Conformational isoforms of BSA with varying pH <sup>103</sup> .....	32
Table 2.2 Parameters from DSC curves for 2% BSA in 0.1M NaCl <sup>112</sup> .....	34
Table 7.1 Sequence identity and similarity between 18 different mammalian and avian serum albumins. Sequence identity (blue) and similarity (red) are shown where higher percentages correspond to darker shading <sup>171</sup> .....	148

## LIST OF FIGURES

Figure 2.1 Amino acid composition of BSA .....	24
Figure 2.2 Structure of BSA indicating the three protein subdomains; Domain I (orange), Domain II (green), and Domain III (purple).....	25
Figure 2.3 Effective charge on BSA as a function of solution pH determined by electrophoresis NMR <sup>47</sup> .....	26
Figure 2.4 Ribbon diagrams <sup>104,105</sup> of BSA and its proposed isoforms in acidic solutions below pH 7 <sup>38</sup> .....	33
Figure 3.1 Primary sequence of BSA <sup>44</sup> . Signal peptide is indicated in cyan, propeptide is indicated in gray, mature protein segment is in green. ....	42
Figure 3.2 CPH Model homology sequence determination and comparison to BSA crystal structure.....	42
Figure 3.3 Protonation states of titratable residues ASP, GLU, HIS, LYS, ARG at pH 7.4 and pH 3.5. Red and blue color denotes negatively and positively charged residues respectively. ....	43
Figure 3.4 Localization of ionized residues on albumin at pH 7.4 and pH 3.5. Chart shows the number of charge per residue type and the total for the entire protein at the two pH values. At pH 7.4, the protein has a total charge of -9 while at pH 3.5, the charge is +100 (including the amine terminal group). ....	47
Figure 3.5 Partial unfolding simulations of albumin with titratable residues set to pH 3.5 ionization states. Orange, green, and purple regions denote domains 1, 2, and 3 respectively. Snapshots of albumin conformations simulation during partial electrostatically-triggered denaturation. ....	50
Figure 3.6 Final simulation conformations of albumin at pH 3.5. Locations of positive charges and counter ions are represented on the right. ....	50
Figure 3.7 Distance measured between the center of mass of domain 1 and domain 3 during simulations with counter ions (red) in comparison with physiological albumin at pH 7.4 (blue). ....	50
Figure 3.8 Percentage of helices in each domain for both N- and F-forms. All F domains loose a fraction of their helical content to turn/coil structures during the partial denaturation in comparison to N conformations.....	52
Figure 3.9 Circular Dichroism data of dilute solutions of BSA (0.005 wt%) at low pH and high temperature showing the relative degree of secondary structure denaturation. Electrostatically triggered denaturation avoids the total loss of secondary structures as observed in thermal denaturation.....	52

Figure 3.10 Solvent accessible surface areas for hydrophobic moieties in the N- and F-forms represented for each domain individually. Each difference is statistically significant to p<0.0001. ....	54
Figure 3.11 Solvent accessible surface areas for hydrophilic moieties in the N- and F-forms represented for each domain individually. Each difference is statistically significant to p<0.0001. ....	54
Figure 3.12 Solvent accessible surface area for hydrophobic, hydrophilic, and all residues. N-F transition causes the protein to become more hydrophobic without change in total average surface area per residue.....	55
Figure 3.13 Solvent accessible surface areas for ASP and GLU residues in the N- and F-forms in the total protein and in for each domain. Normally hydrophilic residues ASP and GLU face the solvent at pH 7.4 but are hydrophobic when protonated at pH 3.5.....	56
Figure 3.14 Dimerization of two F conformation albumin proteins. (a) Minimum distance measured between two F-form BSA structures placed near each other and simulated with and without system neutralizing counter ions. Proteins with counter ions allowed proteins to stay within 0.25nm of each other (black line) until they separated after 36ns. Absence of counter ions allowed unscreened repulsive electrostatic interactions to rapidly overcome attractions (red line). (b) Configurations of two proteins from (a) at 10 ns. The top pair (green protein and white protein) corresponds to the no counter ion simulation and the bottom pair .....	58
Figure 3.15 Explicit counter ion and PB calculated electrostatic surface potentials for single F-form albumin. Explicit counter ion calculations result in a more negative electrostatic potential when compared to PB. Residue ARG 208 has a positive potential when calculated with PB and a negative potential when calculated with explicit counter ions. 60	
Figure 3.16 A histogram of the distances to the nearest Cl <sup>-</sup> ion for the charged N <sup>+</sup> atom on ARG 208 demonstrates that this residue is typically bound to Cl <sup>-</sup> .....	61
Figure 3.17 Explicit counter ion and PB calculated electrostatic surface potentials for two aggregated proteins. Explicit counter ion calculations (left) result in a more negative electrostatic potential when compared to PB (right). Explicit calculations that ignore counter ion contributions (center) are very similar to the positive electrostatic potentials shown by PB. Potentials at the Connolly and SAS surfaces are shown for all cases. For clarity, aggregated proteins are colored individually (inset, orange and purple) to help differentiate them in the potential surface representation.....	62
Figure 3.18 Localization of residues selected for further analysis. ARG 208 is shown in silver. Inset depicts ARG 484 (green), LYS 474 (blue), GLU 478 (red), and LYS 350 (yellow) are all located near the point of contact between the two proteins (orange and purple)... 63	
Figure 3.19 Histograms of distances to nearest Cl <sup>-</sup> ions for the four selected residues ARG 484, LYS 474, GLU 478, and LYS 350 near the point of contact in d and magnified representations of charged atoms associated with Cl <sup>-</sup> . Orange and purple coloring of residue names indicate which protein the residue is from .....	65
Figure 4.1 Constant 20 wt% BSA solution titration curve. ....	76

Figure 4.2 PBSA Gelation at varying concentrations of BSA in solution.....	78
Figure 4.3 Inverted vial depicts 20 wt% PBSA formed at 25°C. Center image depicts PBSA cylinder made in mold at 37°C. Right image depicts TBSA cylinder made in mold at 80°C.....	79
Figure 4.4 TEM image of 0.05wt% BSA solutions at pH 2.18 (a) and pH 3.94 (b) stained with uranyl acetate.....	80
Figure 4.5 SEM images of freeze dried and fractured PBSA hydrogels formed by electrostatic triggering method at pH 3.5 at 37°C.....	80
Figure 4.6 Cryo-SEM images of freeze-fractured hydrogels formed by electrostatic triggering method at pH 3.5 at 37°C (A) or by thermal denaturation at 80°C method (B). ....	82
Figure 4.7 Representative mechanical indentation plots for PBSA and TBSA hydrogels. The slope of the linear elastic regime is equal to the Young's modulus. Arrow directions indicate progression of indenter throughout the test.....	83
Figure 4.8 Mechanical properties of BSA hydrogels demonstrating PBSA hydrogels are softer than TBSA hydrogels. A, Young's modulus of BSA solutions (17 wt% BSA) with different pH values ranging from 2-7 incubated at 37°C (n=4 for each pH value). B, Young's modulus of PBSA (pH 3.5 incubated at 37°C, n=4) and TBSA (pH 7.4 incubated at 80°C, n=8) hydrogels with increasing BSA concentration measured by mechanical indentation. Error bars in A and B represent the standard deviation of the data set. BSA isoforms (E, F, N) are mapped below the plot according to their pH transition values.....	84
Figure 4.9 Effect of 1 mM added salt to BSA precursor solution on PBSA and TBSA Young's modulus. (n=4).....	85
Figure 4.10 Effect of various chemical environments on PBSA hydrogel integrity. Small cylindrical PBSA hydrogels (0.5 cm diameter), acid leached in DMEM for 3 days until the pH returned to neutral pH, were placed in different solutions and photographed over the course of three months. These images are representative of the larger sample set (n=4) and demonstrate hydrogel degradation resistance to acid, base, and salt conditions. Urea and 10% SDS degrade the gels within 17 hrs while disulphide bond reduction by β-ME results in hydrogel swelling. ....	87
Figure 4.11 Biological response to subcutaneously implanted PBSA and TBSA hydrogels. Tissues with implanted PBSA gel disks (a, e), TBSA gel disks (b, f), pH 7.4 BSA solution injection (c, g), and saline control injections (d, h) at 4 days (a, b, c, d) and 4 weeks (e, f, g, h). Samples were stained with H&E, purple:nuclei; pink:cytoplasm; pink-red/I: implant gels. Histological images are aligned to each other at the original interface (white arrow) between the implant and the tissue lining the subcutaneous pocket. Images for each time point are from the same rat and are representative of the group population overall (n=4). .....	89
Figure 5.1 atRA binding to N-form albumin and F-form albumin measured via fluorescence quenching of tryptophan residue TRP 213 at 340 nm (a). Fluorescence intensity for N-form BSA and F-form BSA is consistent before addition of atRA (b). Addition of	

increasing molar concentration of atRA quenches both N-form albumin and F-form albumin fluorescence intensity. d, A greater fraction of initial fluorescence is quenched in N-form albumin than in F-form albumin indicating altered binding affinity. c, Release of atRA into PBS at 37°C from F-form albumin and TBSA hydrogels.....	101
Figure 5.2 Time evolution of atRA binding to N-form albumin and F-form albumin measured via fluorescence quenching of tryptophan residue TRP 213 at 340 nm. Within the first two hours, the degree of fluorescence quenching increases more in N-form albumin than in F-form albumin. Addition of increasing molar concentration of atRA quenches both N-form albumin and F-form albumin fluorescence intensity and increases slightly over 24 hours. ....	101
Figure 5.3 Localization of 10 atRA molecules binding to F-form albumin and N-form albumin after fully atomistic MD simulations for 100 ns. Top panel depicts F-form albumin binding sites located primarily in domain I (orange) and II (green). Clusters of atRA also formed aggregates on the protein surface. Bottom panel depicts N-form albumin binding sites located in all three domains. ....	103
Figure 5.4 Separation distance between individual atRA molecules and their nearest protein surface residues during 100 ns MD simulations for both F-form albumin (A) and N-form albumin (B). Each individual atRA molecule is uniquely colored and becomes bound to the protein surface when the separation distance drops below 0.14 nm. atRA molecules that bind to the surface become effectively immobilized within 100 ns timescale of the simulation. At the end of the simulation, 9/10 atRA molecules are bound to F-form albumin while 10/10 atRA molecules are bound to N-form albumin.....	105
Figure 5.5 Minimum distance mapping to nearest atRA molecule throughout the simulation. Surface representation of F-form albumin and N-form albumin are colored red if atRA passed within < 0.5 nm of the .....	107
Figure 5.6 Potential of Mean Force calculations from umbrella sampling simulations for atRA molecules entering Site 1 on both F-form albumin and N-form albumin. In this particular site, the $\Delta G = -41$ kJ/mol for Site 1 on F-form albumin (a) and $\Delta G = -13$ kJ/mol for Site 1 on N-form albumin (b).....	109
Figure 5.7 atRA released from PBSA and TBSA hydrogels remains bioactive and reduces the migration of smooth muscle cells as evaluated by a 24 hr scratch wound assay. All cultures are serum starved to limit proliferation. Compared to controls, all cells exposed to atRA (direct atRA, eluted from PBSA, and eluted from TBSA) exhibited a significant ( $p<0.05$ ) reduction in cell migration. Scale bar = 100 $\mu$ m.....	110
Figure 5.8 Resistance of atRA-loaded and released PBSA and TBSA hydrogel disks to degradation by successive exposures to 6M urea, 10% SDS and 8M urea. Circles around the samples from 24 well plate are identical and are used to compare the extent of swelling.....	112
Figure 6.1 Preliminary PBSA microparticle fabrication setup. ....	122
Figure 7.1 Shifting DSC curves of 2% BSA in 0.1 M NaCl at various pH values <sup>112</sup> .....	149

Figure 7.2 Circular Dichroism data of dilute solutions of BSA (0.005 wt%) at increasing temperature showing the loss of secondary structure during thermal denaturation.....	151
Figure 7.3 Snapshots of atRA binding to F-form albumin in fully atomistic MD simulations for 100ns. F-form albumin binding sites are located primarily in domain I (orange) and II (green). Clusters of atRA also formed aggregates on the protein surface. ....	152
Figure 7.4 . Snapshots of atRA binding to N-form albumin in fully atomistic MD simulations for 100ns. N-form albumin binding sites are located in all three domains. Clusters of atRA also formed aggregates on the protein surface.....	153

## CHAPTER 1: OVERVIEW

### 1.1 Motivation

Because of its ubiquity and substantial clinical potential, albumin is one of the best-characterized models in protein aggregation research; yet its properties under different conditions are not fully understood. Additionally, the need to solubilize hydrophobic drugs for parenteral administration without the use of organic solvents is significant and has led to the development of numerous protein-based approaches and methodologies<sup>1</sup>. Albumin is a particularly versatile protein carrier because it has been shown to be nontoxic, non-immunogenic, biocompatible, biodegradable, and has high binding capacities to various therapeutic small molecules<sup>2</sup>.

Many types of protein-based hydrogels and drug delivery systems have been described in the literature that employs extreme denaturation conditions<sup>3-10</sup> or chemical crosslinking agents<sup>11-15</sup> to form hydrogels. However, these approaches can significantly alter albumin's secondary structure and as a result, it's intrinsic drug binding affinity.

In this work, we exploited an intrinsic partial denaturation mechanism of albumin to fabricate a new kind of albumin hydrogel. This was achieved by altering the electrostatic charges on the albumin surface leading to interdomain repulsion that exposes buried hydrophobic regions. These regions drive new quaternary assemblies that promote hydrogel formation while preserving some of the original protein secondary structure and functionality within unchanged protein domains.

Therefore, the main objectives of this work are to 1) develop a new crystal structure for F-form albumin to understand the effect of the N-F transition on the secondary and tertiary structure properties of albumin, 2) to determine and characterize the optimal conditions needed to fabricate partially denatured albumin hydrogels without thermal denaturation, and 3) evaluate the drug binding affinity of partially denatured albumin hydrogels.

Furthermore, the study of protein aggregation is critically important for understanding the etiology of many misfolded protein disorders such as Alzheimer's disease, Parkinson's disease, type 2 diabetes, and sickle cell anemia<sup>16</sup>. In addition to a deeper understanding of these conditions, lessons learned from protein aggregation studies have led to the fabrication of several commercially interesting self-assembling biomaterials<sup>16</sup>.

## 1.2 Thesis Outline

Chapter 2 provides a targeted overview of bovine serum albumin, its structural elements from primary to tertiary structure, effects of pH, effects of temperature, known binding sites and therapeutic molecule interactions, and current clinical applications. Chapter 3 explores the pH induced N-F conformational transition. Using all-atom molecular dynamics simulations we show how electrostatic forces can affect the conformation of a single albumin molecule just prior to self-assembly. The results of these simulations suggest that hydrophobic attractions and counter ion binding interactions are key to understanding the formation of this particular hydrogel. Chapter 4 takes lessons learned from Chapter 3 to fabricate albumin hydrogels that avoid thermal denaturation of the use of chemical crosslinking agents. Degradation studies in different chemical environments provide insight into the mechanisms behind the gel formation. In chapter

5, we evaluate both experimentally and computationally, the residual binding affinity of the partially denatured albumin to all-trans Retinoic Acid, a cancer therapeutic with known affinity for normal albumin. Chapter 6 discusses the overall impact and conclusions of the work as well as several potential future studies. This work provides critical new insights about the equilibrium conformation of albumin in its partially denatured state at low pH, and may spur significant progress in our efforts to develop biocompatible protein hydrogel systems, driven by electrostatic partial denaturation, that also exploit albumin's natural drug binding capacity.

### 1.3 Specific Aims

***Specific Aim 1. To develop a crystal structure model showing the effect of electrostatically mediated partial denaturation in albumin proteins.*** a) perform systematic atomistic molecular dynamics simulations to determine the atomistic structure of the pH-induced partially denatured albumin, b) validate secondary structure calculations from simulations by circular dichroism studies to investigate the unfolding of the protein in dilution, and c) examine early stage interactions between partially denatured proteins that lead to aggregation.

***Specific Aim 2. To determine the optimal conditions to fabricate partially denatured albumin hydrogels without thermal denaturation.*** a) evaluate the effect of pH, temperature, and protein concentration on the ability to form albumin hydrogels and b) characterize the mechanical and degradation properties of albumin hydrogels *in vitro* and *in vivo*.

***Specific Aim 3. To evaluate drug binding affinity of partially denatured albumin hydrogels.***

a) evaluate all-*trans* retinoic acid binding affinity to albumin hydrogel by measuring albumin fluorescence quenching, b) evaluate drug bioactivity after release from hydrogel system and c) quantify the drug binding strength to albumin via calculation of the potential of mean force.

## CHAPTER 2: BACKGROUND

### 2.1 Hydrogels in Medicine

The use of hydrogels for medical applications has attracted a great deal of interest due to their fundamental biocompatibility, flexible synthesis, range of constituents, and intrinsic similarities to human anatomic structures and extracellular matrices<sup>17,18</sup>. Hydrogels are three-dimensional molecular lattices made by hydrophilic homopolymers, copolymers, biomolecules, or macromers that are crosslinked to form insoluble polymer matrices<sup>18</sup>. Depending on their constituents and mechanism of synthesis, they can be used as scaffolds for engineered tissues, drug delivery vehicles, cell encapsulation, adhesives, barriers between tissues or surfaces, and also in bionanotechnology applications<sup>17,19</sup>. Typical synthetic monomers used for these applications include poly(ethylene glycol) (PEG)<sup>20</sup>, poly(vinyl alcohol) (PVA)<sup>21</sup>, poly(lactic acid) (PLA)<sup>22</sup>, poly(l-lactic acid) (PLLA)<sup>23</sup>, poly(2-hydroxyethyl methacrylate) (PHEMA)<sup>24</sup>, poly(ethylene oxide) (PEO)<sup>25</sup>, and poly (1,8-octanediol co-citrate) (POC)<sup>26</sup>. Biological hydrogels have been formed with agarose, albumin, alginate, chitosan, collagen, dextran, fibrin, gelatin, hyaluronan, and others<sup>17,18</sup>. Due to albumin's innate ability to bind to a wide variety of drugs and economical advantage over other synthetic and biological hydrogel systems, albumin-based hydrogels are an interesting category of materials for drug delivery systems<sup>27-33</sup>.

## 2.2 Bovine Serum Albumin

As one of the most abundant proteins in blood plasma (4-5g/100mL), serum albumin is one of the most widely studied proteins in the scientific literature<sup>34-36</sup>. An excellent preface to the history of albumin research in the 21<sup>st</sup> century has been recently published by Theodore Peters<sup>37</sup>, the renowned expert of serum albumin research who quite literally, wrote the book<sup>35</sup>. The serum albumin family of proteins are all water soluble and are primary carriers of various solutes in plasma including cations, bilirubin, fatty acids, and drugs<sup>35</sup>. The large wealth of literature on the subject has well characterized most of the physiological properties of the serum albumin protein family (particularly bovine serum albumin). Albumins from different mammalian species demonstrate numerous similarities in their physico-chemical properties<sup>35,38</sup>. Human serum albumin (HSA) and bovine serum albumin (BSA) have 76% homology and are both ~66 kDa. Notable differences between the two include a reduced number of tryptophan residues in HSA<sup>39</sup>, and total number of residues<sup>38</sup>. HSA shows higher thermal stability over BSA reflected in the increased thermal denaturation temperature (HSA- $T_m \sim 80^\circ\text{C}$ , BSA- $T_m \sim 69^\circ\text{C}$ ) at neutral pH with slight variances dependent on the albumin concentration<sup>40</sup>. While differences exist between the two species of albumin, BSA is more prominent in fundamental research due to its lower cost and relative similarity to HSA. For these reasons, BSA is used exclusively in this work.

### 2.2.1 BSA Composition

In mammalian species, albumin is synthesized in the liver as preproalbumin. Bovine preproalbumin has 607 residues including an 18 residue signaling peptide and a 6 residue propeptide. Once the signaling peptide and propeptide are cleaved, the resulting 583-residue

protein is the active form of BSA<sup>41</sup>. As shown in Figure 2.1, albumin has a high content of cystine and charged amino acid residues and has a low content of tryptophan and methionine residues. The glycine and isoleucine content is also lower in BSA than in average proteins<sup>35</sup>.

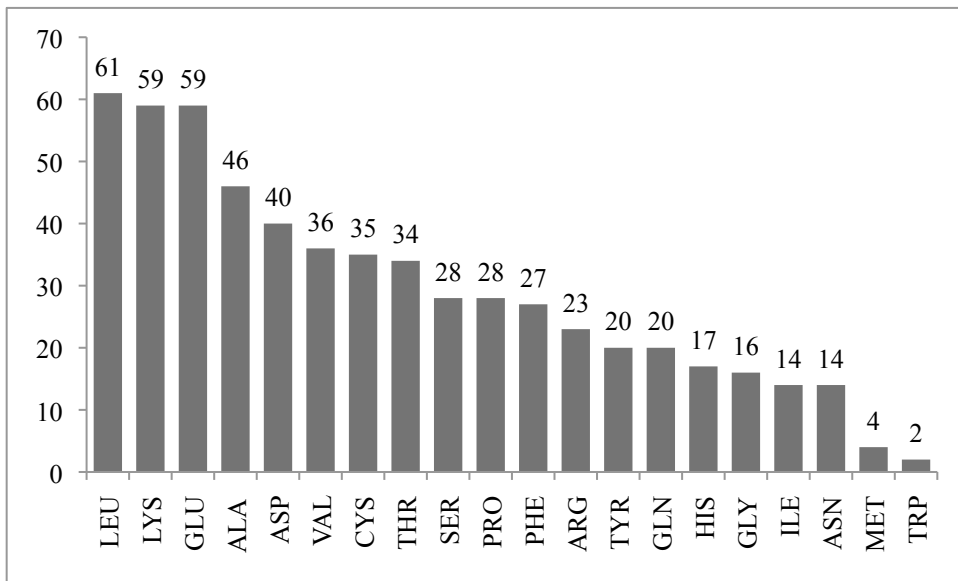


**Figure 2.1 Amino acid composition of BSA**

## 2.2.2 Secondary and Tertiary Structure

BSA is composed of three homologous domains (I, II, III), which are further divided into nine loops (L1-L9) by 17 disulphide bonds (Fig. 2.2). The single sulphydryl group at Cys-34 is exempt from these disulphide bond linkages and is a primary metal binding site. Three subdomains composed of three loops in a long-short-long arrangement form the basis for each domain (IA, IB etc.). The helical content ranges from 48%-67% varying with various environmental factors (pH, Temperature, ionic strength) with a generally accepted 67% helical content in physiological conditions<sup>35,38</sup>. Additionally, BSA contains no  $\beta$ -sheets, 10%  $\beta$ -turns, and 23% extended chains. Inner faces of helices form channels with hydrophobic surfaces that can fit long-chain fatty acid (LCFA) molecules<sup>42</sup>. In physiological conditions, the tertiary

structure of BSA resembles that of a heart structure with an  $R_g = 30.4 \text{ \AA}$  and dimensions ( $65\text{\AA} \times 74\text{\AA} \times 32\text{\AA}$ )<sup>43,44</sup>. The calculated surface area of BSA is  $7070 \text{ \AA}^2$  and its density is  $0.15 \mu\text{g/cm}^2$

<sup>35</sup>

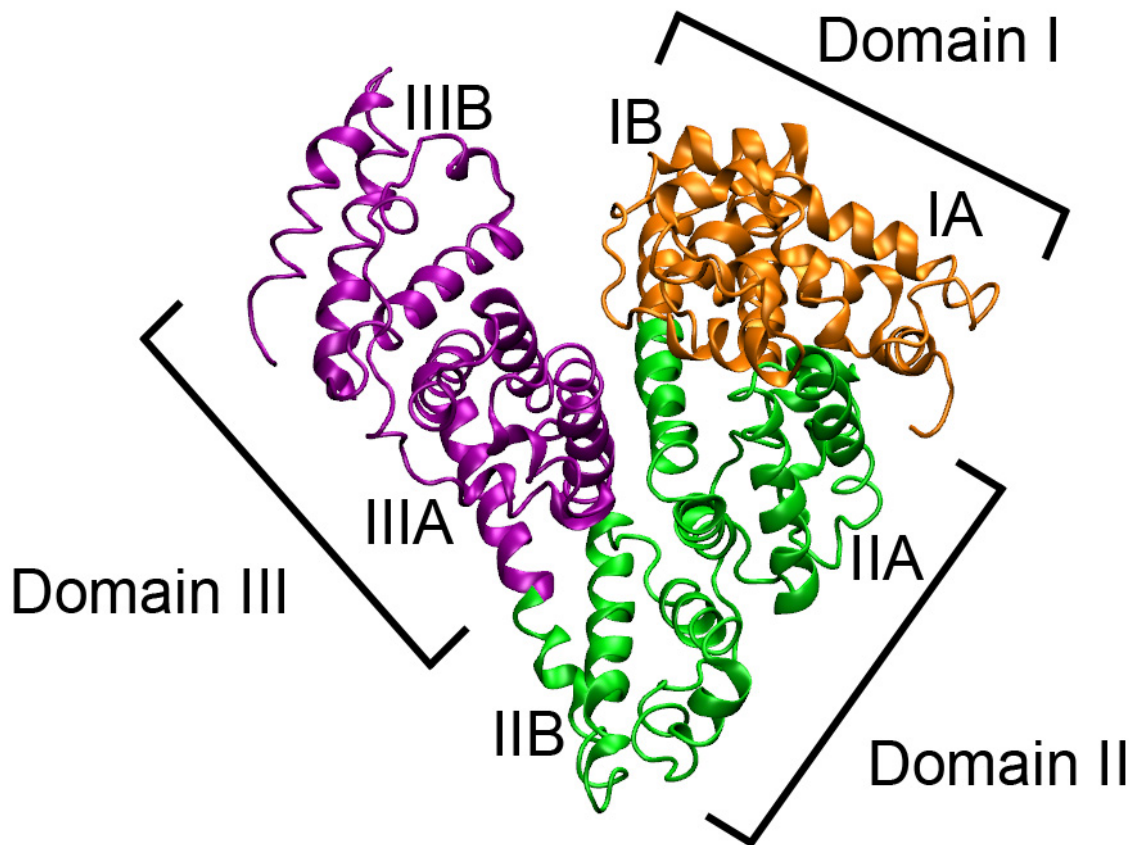


**Figure 2.2 Structure of BSA indicating the three protein subdomains; Domain I (orange), Domain II (green), and Domain III (purple).**

### 2.2.3 Disulphide Bonds

There are 17 disulphide bonds located almost exclusively between helical segments at (1) 77-86; (2) 99-115; (3) 114-125; (4) 147-192; (5) 191-200; (6) 223-269; (7) 268-276; (8) 288-

302; (9) 301-312; (10) 339-384; (11) 383-392; (12) 415-461; (13) 460-471; (14) 484-500; (15) 499-510; (16) 537-582; (17) 581-590. These disulphide bonds are well protected and not readily reducible with denaturating agents and/or salts in the pH range 5-7<sup>38</sup>. Outside this pH range, at pH 3-4 and pH 8-10, the number of reduced bonds increases rapidly<sup>35</sup>. The bonds overlap each other resulting in longer and shorter opposing segments that confer great stability. Cleavage of all 17 disulphide bonds yields albumin molecules that behave hydronymically as long strings ~2140Å in length<sup>35</sup> and lose a great deal of their secondary structure in the process<sup>45,46</sup>. The disulfide bonds are all reducible by 2-mercaptoproethylamine or β-mercaptoproethanol.

## 2.2.4 Charge Distribution

Charges on BSA are not uniformly distributed among the three domains. At neutral pH, BSA has a net charge of -10, -8, and 0 for domains I, II, and III respectively<sup>35</sup>. The isoionic point and isoelectric (pI) point of BSA are at pH 5.2 and 4.7 respectively. Recent analysis by electrophoresis NMR has quantified the effective charge on BSA as a function of the solution pH (Fig. 2.3)<sup>47</sup>.

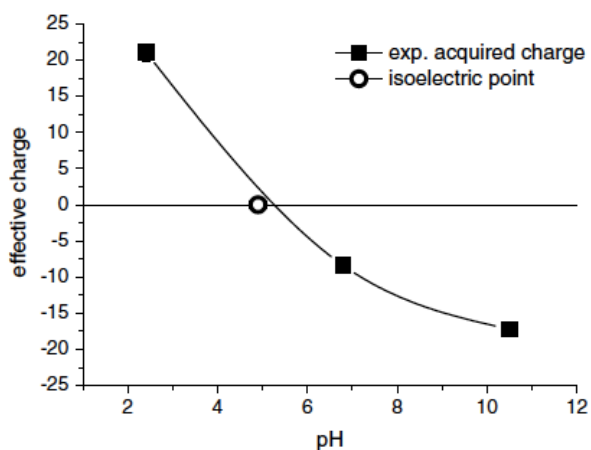


**Figure 2.3 Effective charge on BSA as a function of solution pH determined by electrophoresis NMR<sup>47</sup>.**

Knowledge of the effective charge on BSA at different pH values illuminates the effect of electrostatic interactions and their role in the albumin gelation mechanisms.

### **2.2.5 Binding Sites**

In addition to buffering blood pH, one of the key functions of serum albumin is that of a carrier for other insoluble species in the circulatory system. Six binding sites have been identified on BSA for LCFAs of which the strongest three are located at Lys-474, Lys-350, and Lys-116 ( $\Delta G = -10$ ,  $\Delta H = -18$ ,  $T\Delta S = -8$  kcal/mol)<sup>35,42,48</sup>. Removal of LCFA's from albumin is called defatting. BSA that has been defatted is more sensitive to changes in pH far away from neutral and is also more protected by the presence of salts. The presence of fatty acids stabilize its binding affinity for bilirubin<sup>35</sup>. For these reasons, defatted albumin was used exclusively in this study. The most common defatting procedure involves bringing the solution to pH 3, which disrupts the hydrophobic helical channels that bind to LCFAs. Apart from LCFAs, other hydrophobic organic anions, in the 100-600 Da range (e.g bilirubin, hematin) bind most strongly to BSA. With an average accessible hydrophobic area of  $130 \text{ \AA}^2$ , circulating albumin (0.06 mM) typically carries 1-2 LCFA molecules (1 mM)<sup>35</sup>. Also of note, pure albumin is colorless, however due to residual binding to bilirubin, carotene, and hematin after purification protocols confer a yellowed tint to albumin.

Bilirubin most likely binds to a single primary site by carbamidate to Lys-220 ( $\Delta G = -11$ ,  $\Delta H = -13.5$  kcal/mol,  $\Delta S = -8.4$  cal/mol\*deg) at physiological conditions. Bilirubin binding increases with pH and decreases with increasing chloride concentration. The shape of the bilirubin binding pocket is somewhat flexible due to chiral differences in the binding pocket between HSA and BSA and also at various pH values<sup>35</sup>. Like the LCFA binding sites, the

bilirubin binding site is strongly hydrophobic. The bilirubin binding site is located just outside Sudlow's Site I. The fluorescent marker fluorescein also binds just outside Site I to the Tyr-137 where it has a stabilizing effect similar to LCFA<sup>49,50</sup>.

#### 2.2.5.1 *Sudlow's Site I*

Sudlow's Site I is located in domain IIA and includes residues from Lys-199 through Glu-292. The site is hydrophilic near the entrance and hydrophobic at its furthest depth<sup>38</sup>. Bulky heterocyclic anions with centrally located charges are frequent visitors of this site. If the space permits, it can bind to multiple molecules and is responsible for albumin's ability to bind to a large number of substances including bilirubin, warfarin (for anticoagulation treatment)<sup>51</sup>, phenylbutazone (nonsteroidal anti-inflammatory)<sup>51</sup>, azapropazone (nonsteroidal anti-inflammatory)<sup>52</sup>, indomethacin (nonsteroidal anti-inflammatory)<sup>53,54</sup>, tolbutamide (diabetes mellitus treatment)<sup>55</sup>, iodipamide (contrast enhancement)<sup>51</sup>, iophenoxic acid (contrast enhancement)<sup>55</sup>, furosemide (diuretic treatment)<sup>56</sup>, buclome (nonsteroidal anti-inflammatory)<sup>56</sup>, sulfisoxazole (antibiotic)<sup>57</sup>, and some bile salts.

#### 2.2.5.2 *Sudlow's Site I*

Sudlow's Site II is similar to Site I in that it can bind to a large number of substances. Site II is located in domain IIIA and some neighboring helices with a hydrophobic pocket measuring 8x25Å. Site II also binds to bile salts and non-steroidal anti-inflammatory agents with ionized carboxyl groups<sup>35</sup> such as diazepam (anxiolytic)<sup>51</sup>, diflunisal (nonsteroidal anti-inflammatory)<sup>58</sup>, ibuprofen (nonsteroidal anti-inflammatory)<sup>51</sup>, ketoprofen (nonsteroidal anti-inflammatory)<sup>59</sup>, naproxen (nonsteroidal anti-inflammatory)<sup>60</sup>, 6-MNA (nonsteroidal anti-

inflammatory)<sup>61</sup>, diclofenac(nonsteroidal anti-inflammatory)<sup>61</sup>, etodolac(nonsteroidal anti-inflammatory)<sup>62</sup>, clofibrate (fibrate)<sup>63</sup>, and iopanoic acid (contrast enhancement)<sup>55</sup>. The drug propofol (hypnotic anesthetic)<sup>64</sup> has been shown to bind to both Sudlow's Site II as well as subdomain IIIB. Subdomain IB has shown binding affinity for fusidic acid (bacteriostatic antibiotic)<sup>65</sup> and lidocaine (anesthetic)<sup>66</sup>. Typically, drug binding events at Sudlow's Site I and Site II can be monitored by spectroscopic fluorescence quenching<sup>67</sup>.

#### 2.2.5.3 Additional albumin binding sites

Another important binding site involves the free sulphydryl group in residue Cys-34. Cys-34 binds to NO, and to many pharmaceutical drugs including D-Penicillamine (gold toxicity treatment), meso 2,3-dimercaptosuccinic acid (lead intoxication treatment), N-2-mercaptopethyl-1,3-diaminopropane (captopril used for antihypertension), disulfiram (chronic alcoholism), cis-dichlorodiammineplatinum(II)<sup>68</sup> (cisplatin, for chemotherapy) via nucleophilic entering group, cryoglobulin, IgA, mutant antithrombin, and mutant fibrinogen<sup>35</sup>. Of the total circulating NO in plasma (7μM), 82% is carried by albumin as S-nitrosoalbumin that is detectable by HPLC or GC followed by a photolysis step yielding chemiluminescence<sup>69</sup>. Other sulphydryl compounds and certain oxidants also bind to Cys-34.

There are several additional chemotherapeutics that bind to albumin including bicalutamide<sup>32</sup>, camptothecin<sup>32</sup>, 9-amino camptothecin<sup>32</sup>, idarubicin<sup>32</sup>, teniposide<sup>32</sup>, and etoposide<sup>32</sup>. Therapeutics such as probenecid (antacid)<sup>70</sup>, amitriptyline (tricyclic antidepressant)<sup>70</sup>, debrisoquine (antihypertensive)<sup>70</sup>, digitoxin (anti-arrhythmic)<sup>71,72</sup> are also known to bind to albumin but their binding site remains unknown.

A number of ions also bind to albumin at various locations throughout the protein.

Chloride ions bind with a  $K_a = 720 \text{ M}^{-1}$  with approximately 7-8  $\text{Cl}^-/\text{albumin}$  at physiological conditions (100mM  $\text{Cl}^-$  and pH 7.4)<sup>73</sup>. Cu(II) and Ni(II) bind to the N terminus if the third residue is a histidine. The first four BSA residues (Asp-Thr-His-Lys) have the flexibility to form the square-planar bipyramidal Cu(II) binding site with a  $K_a = 11.2\text{-}16.2^{35}$ . Ni(II) binds in a similar fashion but ~30% is held in an octahedral structure and since Ni(II) is slightly larger than Cu(II), it will eventually get replaced by Cu(II).  $\text{Ca}^{2+}$  has a weaker binding affinity with a pKa of 2.65 (pH 7.4 and ionic strength 0.15) resulting in only 1-2  $\text{Ca}^{2+}/\text{albumin}^{35}$ . Studies with Tb(III) as a fluorescent probe for  $\text{Ca}^{2+}$  binding indicate that the carboxyl side chains of Asp and Glu aspartic and glutamic acids are the major groups involved in  $\text{Ca}^{2+}$  binding to albumin<sup>74</sup>. Most Asp/Glu residues are located in DI (contributing to its overall larger negative charge).  $\text{Mg}^{2+}$  is bound with less affinity than  $\text{Ca}^{2+}$ , having a pKa = 2.0 resulting in <1  $\text{Mg}^{2+}/\text{albumin}$ . Zn(II) (pKa 7.3), Cd (pKa 5.3), Mn(II) (pKa 4.24), Hg(II), and Co(II) also bind to albumin with the later two binding to the single thiol group at Cys-34 and Cu(II)-Ni(II) site respectively<sup>35</sup>. Polymeric forms of BSA exhibit little or no fatty acid binding, 50% less bilirubin binding, and 75% less antibody binding<sup>35</sup>.

#### 2.2.5.4 All-trans Retinoic Acid albumin binding site

All-trans Retinoic Acid (atRA) is a clinically available therapeutic molecule with a specific binding affinity for albumin<sup>75</sup>. It is currently being evaluated for use in the treatment of various cancers such as acute promyelocytic leukaemia<sup>76-79</sup>, Kaposi's sarcoma<sup>80</sup>, head and neck squamous cell carcinoma<sup>81</sup>, ovarian carcinoma<sup>82</sup>, bladder cancer<sup>83</sup>, neuroblastoma<sup>84</sup>

myelodysplastic syndrome<sup>85</sup>, metastatic breast cancer<sup>86</sup>, and in other diseases like emphysema<sup>87,88</sup>. It is the main biologically active derivative of vitamin A and an essential factor involved in the regulation of angiogenesis. As a potent regulator of gene transcription, atRA plays an important role in the regulation of cell growth, embryonic development, apoptosis, and homeostasis<sup>75</sup>, and has a well-established ability to inhibit malignant cell growth. As such, it is the only clinically effective therapy used for treatment of acute promyelocytic leukaemia<sup>77,89</sup>. The potential of atRA use in other cancer therapies has driven the development of novel delivery systems<sup>90</sup> for atRA beyond the topical<sup>91</sup> and oral<sup>77-79,89,92,93</sup> formulations currently available. Several pharmacotherapies currently in clinical trials or on the market to deliver other bioactive therapeutic molecules like paclitaxel or interferon utilize albumin as a component of their formulations yet do not utilize albumin's intrinsic binding capability for loading drugs<sup>94,95</sup>.

Maiti et al.<sup>75</sup> performed fluorescence quenching and circular dichroism studies to investigate the binding site of atRA on albumin. From CD analysis, they conclude that atRA binding causes a minor conformational change in albumin leading to a small 1% loss in alpha helical content. Computational docking studies determined that the atRA binding pocket is located within the subdomains IIA and IIIA. This binding involved specific residue interactions on TRP 214 LYS 195, LYS 436, CYS 448 and ASP 451 measured by decreases in solvent accessible area<sup>75</sup>. The inside of this binding pocket is primarily hydrophobic in nature, which is consistent with atRA's own hydrophobicity, with a maximum solubility of 0.21μM in water<sup>96</sup>. Thermodynamic analysis of albumin-atRA binding found that the major contribution to the free energy came from the entropy rather than the enthalpy. Binding is a spontaneous process (-31 kJ/mol) that may be driven by an initial hydrophobic association followed by electrostatic

interactions<sup>75</sup>.

## 2.2.6 Effect of pH

The ability of serum albumin to undergoes reversible conformational isomerization with changes in solution pH (Table 2.1) has been well documented in the literature<sup>38,97-103</sup>. Ribbon diagrams<sup>104,105</sup> of the N-form and the proposed F-form and E-form are shown in Fig. 2.4<sup>38</sup>.

**Table 2.1 Conformational isoforms of BSA with varying pH<sup>103</sup>.**

	E	↔	F	↔	N	↔	B	↔	A
pH		2.7		4.3		8		10	
Name	Expanded		Fast		Normal		Basic		Aged
%Helix	35		45		55		48		48

### 2.2.6.1 N-F Transition

Transitions away from the N-form result in decreases in  $\alpha$ -helical content and expansion of the tertiary structure. The N-F transition begins with expansion in DIII followed by expansion of its three subdomains. DI and DII do not begin to lose their helical structure until pH falls to 3.5<sup>35</sup>. At this stage, the unfolding of the protein is still fully reversible. A modified BSA molecule (BSA Fraction V with a single cleaved peptide bond in DIII, Gln-393 – Phe-394) forms a transparent gel at pH 4 with concentrations at >70 mg/mL<sup>106</sup>. The F-form is practically insoluble (<<1 mg/mL) in 3.0M KCl, a solution that would solublize the N-form. Mildly acidic conditions at pH 4.2 results in protein dimerization with contact points at the free Cys-34 residue as observed by increased BSA weight in F-spin column experiments, gel electrophoresis, or ultra-centrifugation<sup>107</sup>. Modification of the Cys-34 residues with blocking agents longer than the

6Å cleft results in the prevention of the dimerization. In comparison to the native N-form albumin, dimmers of BSA have an altered surface hydrophobicity<sup>107</sup>.

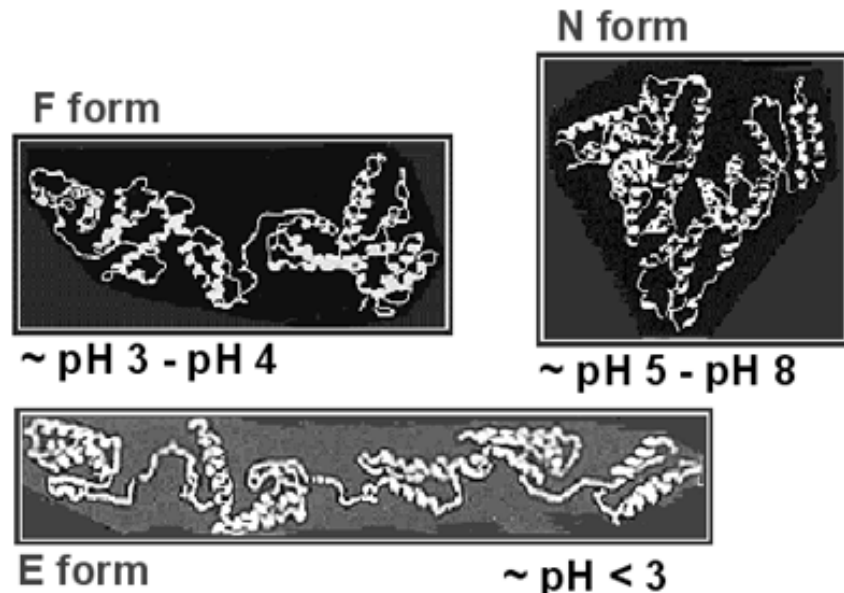


**Figure 2.4** Ribbon diagrams<sup>104,105</sup> of BSA and its proposed isoforms in acidic solutions below pH 7<sup>38</sup>.

#### 2.2.6.2 F-E Transition

There is further unfolding of albumin conformation from pH 3.5 to pH 2.5 with an increase in viscosity near the pH 1.7<sup>35,103</sup>. Helical content decreases an additional 10% from the F-form. The reported absolute helical percentages vary somewhat between groups (N>F>E, 55%>45%>35%<sup>103</sup> and 73%>65%>52%<sup>106</sup>) but generally follow the same amount of relative decline. Expansion can be suppressed by increasing ionic strength of the solution. When all carboxyl groups are protonated, domains and subdomains are all repelled by Lys, Arg, and His residues. The charge distribution at this stage is +34,+36,+32 for each domain respectively and charge densities are +1.9, +1.8, +1.6 per 10 amino acid residues. Unfolding at low pH causes

disulphide bond changes from the normal gauche-gauche-gauche to gauche-gauche-trans forms but does not increase the availability of the disulphide bonds to reduction upon return to pH 6<sup>108,109</sup>. Due to its well-characterized pH transitions, BSA is often used as a model protein to investigate acidification of other synthetic polymer systems such as PLGA<sup>110</sup>.

### 2.2.7 Effect of Temperature and Thermal Gelation

Of the different methods of BSA denaturation, the most widely studied is thermal denaturation<sup>4,35,111,112</sup>. Between 42°C and 50°C in physiological conditions, conformational changes induced by thermal denaturation are reversible. In the range 50°C to 60°C, these conformational changes are only partially reversible. Differential scanning calorimetric studies of thermal denaturation have demonstrated that the thermal denaturation temperatures are strongly influenced by the solution pH and ionic strength (Table 2.2)<sup>112</sup>. The DSC curves identify a decreasing shift in thermal denaturation temperature ( $T_d$ ) and onset of thermal denaturation ( $T_i$ ) to lower temperatures with decreasing pH (Appendix C). NaCl has a protective effect on the thermal denaturation temperature, requiring higher temperatures with increasing ionic strength. Maximal denaturation is achieved at 110°C – 120°C<sup>113</sup>.

**Table 2.2 Parameters from DSC curves for 2% BSA in 0.1M NaCl<sup>112</sup>.**

pH	$T_i$ (°C)	$T_d$ (°C)	$\Delta H$ (kJ·mol <sup>-1</sup> )
2.99	—	—	—
3.51	28.6	46.8	155
4.05	43.1	53.1	185
4.20	29.7	44.2 57.3	510
4.49	34.0	51.8 60.1	620
4.99	41.6	59.8 shoulder	783
5.25	47.7	61.8 shoulder	786
5.61	50.1	63.9	785
7.00	51.9	64.3	839
8.01	43.8	60.9	709
9.03	43.8	61.2	607
10.01	45.7	60.8 81.3	—
11.00	—	—	—

Thermal denaturation generally leads to significant loss in secondary structure content and protein aggregation; this process is dependent on the initial concentration and ionic strength of the solution<sup>114</sup>. The rate of aggregate growth increases with increasing temperature but whenever the free Cys-34 is blocked, aggregation is slower and becomes dependent on conformational changes at the tertiary level for aggregates to form<sup>35,50,115</sup>. Thermal denaturation observed by CD at 70°C shows the evolution from double  $\alpha$ -helix peaks to a  $\beta$ -rich structure where the most notable shifts in spectra occur in the first 70 minutes after which time aggregation is driven mainly by conformational changes at the tertiary level<sup>50</sup>.

The mechanism behind thermal aggregation is believed to occur due to three processes; 1) liquid-liquid demixing (LLD), 2) conformational changes in BSA structure, and 3) cross-linking of proteins<sup>50,116,117</sup>. The argument for LLD follows the observation that the self-assembly of biopolymeric gels can often occur at concentrations below the random cross-link percolation threshold<sup>10</sup>. While conformational changes at elevated temperatures increase the availability of cross-linking sites, it alone is insufficient for self-assembly. A mesoscopic symmetry break from the initially homogenous sol due to concentration fluctuations enable the onset of solute-solute correlations<sup>118</sup>. These correlations lead to the spinodal demixing of the sol and provide the basis for the thermal gel network. In a system based on Lysozyme protein, a similar effect was observed and viscoelastic phase separation preceded the formation of percolating gel networks<sup>119</sup>. The self-association of BSA in these altered conformations has also been used as a model to better understand the aggregation of other protein precipitates, such as hemoglobin<sup>120,121</sup>.

The observation of the structure of heat-induced BSA aggregates by TEM imaging shows a string of linearly oriented globules<sup>8,122-124</sup> similar to those formed by ovalbumin<sup>125</sup>. When the protein concentration is larger than a critical value, a gel will form. Heat-induced BSA gels have a critical concentration wt% of 5-7%<sup>8,126</sup>. 6% BSA solutions made at pH 7.5 with a 85°C heating method would only gel with an NaCl concentration > 20mM. These same gels made in the absence of NaCl would only form in the pH range 4.0-6.5<sup>8</sup>. The addition of various salts (1-30mM Cu<sup>2+</sup>/Zn<sup>2+</sup>, 5mM CuSO<sub>4</sub>/MgSO<sub>4</sub>/FeSO<sub>4</sub>/ZnSO<sub>4</sub>) into the BSA solutions (5-6.6 wv%) also forms random and spherical aggregates<sup>9,127</sup>.

Differences in the opacity of these gels have been reported and result from the equilibrium between attractive and repulsive interactions between denatured proteins, which in turn depends on the net charge of the protein and ionic strength of the solvent<sup>8,126,128</sup>. These two variables are controlled by the solution pH and the ionic strength respectively. Based on this equilibrium, two variants of globular protein gels are possible primarily evidenced by electron microscopy<sup>122,129</sup>. Strong electrostatic repulsions (low electrostatic screening) lead to a linear aggregation process resulting in a transparent fine-stranded gel while at low electrostatic repulsions (high electrostatic screening), the sticking of large compact aggregates prevail and result in an inhomogeneous opaque coagulate with a coarse lumpy structure<sup>3,8,115,126,129,130</sup>. Increasing the ionic strength increases the length, ease of cross-link formation, and interaction of the linear BSA monomers by decreasing electrostatic repulsions leading to lower percolation concentrations around 6 wt%. Once heat-induced BSA gels are formed, their sensitivity to solution pH is dependent on the pH of the initial solution, generally swelling in high pH solutions (pH > pI)<sup>131</sup>.

### 2.2.8 Additional Denaturing Mechanisms

BSA can also be denatured by various other chemical substances and techniques such as urea, guanidium chloride (GuCl), organic solvents, and UV irradiation. Urea and GuCl denature BSA by weakening hydrophobic interactions by causing water to act as a better solvent for nonpolar residues. There is little denaturing effect on BSA with <4M urea or <1.8M GuCl. The midpoint of optical changes during denaturation occurs with urea concentrations ~6M and rapid changes occur at 8M<sup>35</sup>. In addition to disrupting hydrophobic interactions, 8M urea at pH 5 fully reduces the 17 disulphide bonds<sup>132</sup>. The effects of 8M urea or 4M GuCl at pH 5, 25°C for 5 days are completely reversible as long as the concentration of albumin is <2.5mg/mL. At higher concentrations, oligomers have been reported to form, which were attributed to disulphide bond interactions (preventable by blocking the free Cys-34 residue)<sup>132-134</sup>. Organic solvents cause irreversible denaturation with increasing temperature and pH. Albumin form aggregates in ethanol at low pH but aggregation is again preventable by blockage of the free Cys-34 residue<sup>135</sup>. UV irradiation results in covalent changes and peptide bond cleavage with a loss of immune reactivity<sup>134</sup>.

## 2.3 BSA gelation systems

There are a number of additional gelation systems that take advantage of the thermal gelation properties of BSA for fabrication of polymer blends with other synthetic polymers<sup>12,13,136-138</sup>. One technique for the incorporation of BSA into polymer blends involves the conjugation of methacrylic anhydride (BSA-MA)<sup>138</sup>. The BSA-MA can then participate in a

variety of copolymerization schemes such as with N,N-dimethylacrylamide (DMAA) or N-isopropylacrylamide (NIPAAm)<sup>13,136-138</sup>. In both procedures, BSA microspheres were formed by a radical copolymerization technique involving *n*-hexane and either carbon tetrachloride or chloroform in a round-bottom reaction vessel at 40°C under constant stirring. Copolymerization with NIPAAm conferred thermo-responsive properties on the BSA microspheres while maintaining the water-soluble properties of the BSA<sup>136</sup>. Previously, the incorporation of BSA into a poly(tetraethylene glycol-co-citrate) gel was achieved and demonstrated to form transparent gels which do not degrade *in vivo*<sup>139</sup>.

## 2.4 Current Medical Applications of Albumin

HSA is used medically (Plasbumin®, Plasmanate®) in a variety of applications to treat shock, burns, correct blood volume deficiency, and raise low blood protein content<sup>35</sup>. In these treatments, albumin is delivered intravenously. Other uses for albumin include filtration/removal of toxins, imaging (Albunex, CARDIOSphere®, Myomap, Optison™, Quantison), and drug delivery. For some imaging applications, gelled microspheres are formed with glutaraldehyde and labeled with <sup>125</sup>I. These microspheres are < 10 µm and they segregate to the reticuloendothelial system (RES) while larger aggregates (10-40 µm, formed by autoclaving 5% HSA at pH 5-6, 121°C) segregate to the lung capillaries<sup>35</sup>. Albunex (Infoson in Europe), CARDIOSphere®, Myomap, Optison™, and Quantison are a variety of ultrasound contrast agents composed of HSA microbubbles that consist of air-filled spheres ( $d = 4\mu\text{m}$ ) of HSA. Albunex is produced by sonication at 20 kHz of heated commercial 5% albumin in a flowing stream<sup>140,141</sup>. These microbubbles trigger no immune response and are supported by a thin shell

of denatured albumin 150 Å thick. The denatured albumin is composed of several protein layers in parallel alignment with 35 Å ridges<sup>142,143</sup>. Other formulations of albumin microbubbles are proprietary. For drug delivery applications, gelled microspheres formed by heat or glutaraldehyde denaturation with high concentrations ~ 50% w/v are used<sup>144</sup>. Coupling agents such as formaldehyde and carboiimide are occasionally used to bind anti-tumor drugs such as adriamycin, doxorubicin, deoxyfluorouridine, cisplatin, and cyclophosphamide to the HSA microsphere<sup>35,145</sup>. Incorporation of magnetite during their formation enables delivery via magnetic controls<sup>146</sup>. In the treatment for malignant melanoma, it is also known that delivery of albumin with IL-2 and  $\alpha$ -interferon reduces the toxicity and enhances treatment response although the mechanism behind this effect is unknown<sup>147</sup>.

## CHAPTER 3: ELECTROSTATICALLY TRIGGERED PARTIAL DENATURATION OF ALBUMIN

### 3.1 Objective

Understanding the behavior of albumin at low pH begins with observing and characterizing the atomistic structure of albumin. Human and bovine serum albumin structures at pH 7.4 are well characterized to 2.5Å resolution<sup>148</sup> and 2.47Å resolution<sup>149</sup>, respectively. While hypothetical structures of albumin at low pH can be found in the literature as early as 1966, these are deduced from small-angle X-ray scattering and hydrodynamic radii determination, which result in very low resolution models<sup>102</sup>. Scrutiny of more recent literature indicates the existence of several additional characteristics of the N-F albumin transition including changes in adiabatic compressibility<sup>150</sup>, NMR chemical shifts<sup>101</sup>, degree of partial denaturation by domain region<sup>151</sup>, and updated small-angle X-ray scattering studies<sup>43,152</sup>. While these elements are very helpful, the best structural determination of albumin at pH 3.5 remains a low-resolution 3D model<sup>38</sup>. In order to better understand the albumin hydrogel system, **our primary objective is to determine the atomistic structure of albumin at low pH.** To do this, we carried out detailed all-atom molecular dynamics simulations of albumin using FAMBE-pH to determine the protonation probability for each titratable residue. We then analyzed these simulations to understand how electrostatic interactions, bought on by the lowering of the protein pH, can affect the conformation of a single albumin molecule. We then analyzed the tertiary structure and solvent-accessible surface area of albumin after electrostatically-triggered partial denaturation. **We**

**hypothesize that this approach will generate the first high-resolution atomistic structure of albumin at low pH that reproduces features predicted by others.** After the determination of this new structure, we can then use this model to investigate the early stages of protein aggregation in this system. Molecular dynamics simulations with two partially denatured proteins are used to investigate how this aggregation may occur in such a highly charged system. The electrostatic potential was calculated from both the single and double protein simulations to investigate the effect of electrostatic interactions between two proteins.

## 3.2 Experimental Section

### 3.2.1 Atomistic Bovine Serum Albumin Molecular Dynamics

F-form bovine serum albumin models were developed by simulating an N-form albumin model from the primary bovine serum albumin sequence set to the charged state of F-form albumin at pH 3.5.

#### 3.2.1.1 Initial protein homology determination

Determination of the tertiary N-form structure of BSA was obtained by submitting the primary BSA amino acid sequence (GenBank: CAA76847.1) in FASTA format to a protein homology modeling server (CPHmodels 3.0) (Fig. 3.1)<sup>44,153,154</sup>. CPHmodels identified HSA as the closest existing protein structure to BSA and the result matches well (RMSD = 1.39Å) with recent crystallographic BSA structures (Fig. 3.2)<sup>149</sup>. The resulting output file was used as the basis for all subsequent atomistic simulations of BSA.

```
>gi|3336842|emb|CAA76847.1| bovine serum albumin [Bos taurus]
MKWVTFISLLLLFSSAYSRGVFRRDTHKSEIAHRFKDLGEEHFGLVLIAFSQYLQQCPFDEHVKLVNEL
```

```

TEFAKTCVADESHAGCEKS LHTLFGDELCKVASLRETYGDMADCC EKQE PERNECFLSHKDDSPDLPKLK
PDPNTLCDEFKADEKKFWGKYLYE IARRHPYFYAPELLYYANKYNGVFQECCQAEDKGACCLPKIETMRE
KVLTSSARQRLRCASI QKFGERALKAWSVARLSQKFPKAEFVEVTKLVTDLTKVHKECCHGDLLECADDR
ADLA KYICDNQDTI SS KLK E C D K P L L E K S H C I A E V E K D A I P E N L P P L T A D F A E D K D V C K N Y O E A K D A F L
G S F L Y E Y S R R H P E Y A V S V I L R L A K E Y E A T L E E C C A K D D P H A C Y S T V F D K L K H L V D E P Q N L I K Q N C D Q F E K
L G E Y G F Q N A L I V R Y T R K V P Q V S T P T L V E V S R S L G K V G T R C C T K P E S E R M P C T E D Y L S L I L N R L C V L H E K T
P V S E K V T K C C T E S L V N R R C F S A L T P D E T Y V P K A F D E K L F T F H A D I C T L P D T E K Q I K K Q T A L V E L L K H K P
K A T E E Q L K T V M E N F V A F V D K C C A A D D K E A C F A V E G P K L V V S T Q T A L A

```

**Figure 3.1 Primary sequence of BSA<sup>44</sup>. Signal peptide is indicated in cyan, propeptide is indicated in gray, mature protein segment is in green.**

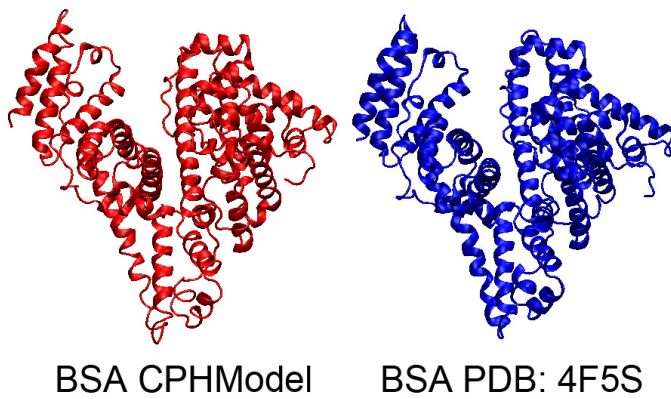


**Figure 3.2 CPH Model homology sequence determination and comparison to BSA crystal structure.**

### 3.2.1.2 FAMBE-pH Calculations

FAMBE-pH, a program that calculates the total solvation free energies of proteins as a function of pH, was used to calculate the ionization state of titratable residues (ASP, GLU, HIS, LYS, ARG) on BSA at pH 7.4 and 3.5<sup>155</sup>. These titratable residues are represented in Figure 3.3 for both pH values. The FAMBE-pH program employs a combination of approaches to calculate these free energies and involves (i) solving the Poisson equation with a fast adaptive multigrid boundary element method (FAMBE); (ii) calculating electrostatic free energies of ionizable residues at neutral and charged states; (iii) defining a precise dielectric surface interface; (iv) tessellating the dielectric surface with multisized boundary elements; and (v) including 1:1 salt effects<sup>155</sup>. This 1:1 salt effect is included, indirectly, in the FAMBE-pH method as was done for the salt-dependent generalized Born method. The computation of the free energy of solvation by

FAMBE-pH includes the following terms: (1) the free energy of creation of a molecular cavity in the water; (2) the free energy of van der Waals interactions between the protein and the water solvent; (3) the free energy of polarization of the water solvent by the protein; and (4) the free energy of equilibrium titration of protein for a given pH and conformation<sup>156</sup>. Since the number of ionizable groups in albumin ( $n = 198$ ) is more than ~20-25, the Tanford-Schellman integral was used to calculate the equilibrium proton binding/release<sup>155</sup>. After the calculation, the protonation states for each titratable residue was fixed to the model.

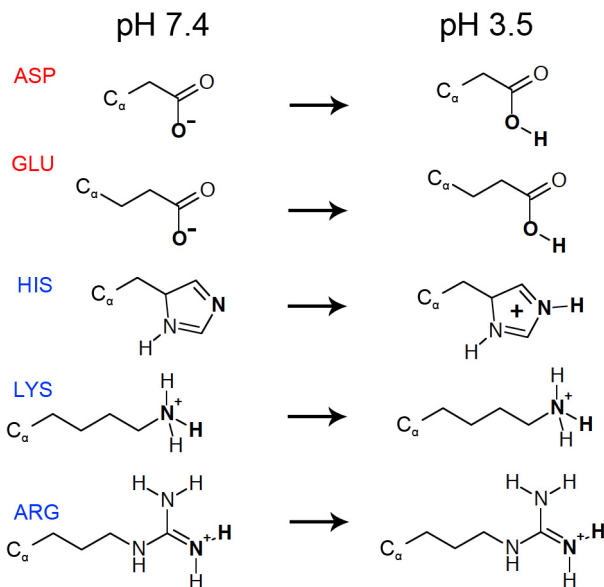


**Figure 3.3 Protonation states of titratable residues ASP, GLU, HIS, LYS, ARG at pH 7.4 and pH 3.5. Red and blue color denotes negatively and positively charged residues respectively.**

### 3.2.1.3 Energy Minimization and molecular dynamics

The protonated albumin model was then solvated in a  $17 \times 7 \times 7 \text{ nm}^3$  box with ~300,000 SPC water molecules<sup>157</sup> and neutralizing counterions (100 Cl<sup>-</sup>), energetically stabilized by steepest descent algorithm, and equilibrated for at least 1 ns in water at 300 K. The long axis of the simulation box was chosen to allow room for expected protein expansion. Fully atomistic

molecular dynamics simulations were performed using the GROMACS 4.5.4 simulation package<sup>158-161</sup>. The all-atom optimized potential for liquid simulations (OPLS/AA) force field parameters<sup>162</sup> were used to describe interactions among the atoms. A simulation was run for production for 64 ns in canonical (NVT) ensemble at constant temperature 300 K with Nose-Hoover temperature coupling method<sup>158,162</sup>. Analysis of protein secondary structures was performed by the STRIDE webserver<sup>163</sup>.

#### *3.2.1.4 Interdomain, interprotein, counter ion – residue distance calculation*

The expansion of the protein during partial denaturation was quantified with the built in GROMACS g\_dist command using the centers of mass for domain 1 and domain 3 on albumin as endpoints. This same command was also used to determine the distance between counter ions and the charged atoms of specific residues on the protein surface. The GROMACS g\_mindist command was used to calculate the minimum distance between the two proteins in the dimer simulations.

#### *3.2.1.5 Solvent accessible surface area calculation*

The GROMACS g\_sas command was used to calculate the solvent accessible surface (SAS) area for each residue. Each residue was categorized as hydrophobic or hydrophilic according to the scale determined by Serada et al.<sup>164</sup>. We normalized measured SAS areas by the number of atoms contained within each category (domain 1/2/3 and hydrophobic/hydrophilic) for both N- and F-forms and report the absolute area values.

### 3.2.2 Circular Dichroism Experiments:

Dilute solutions (0.005 wt%) of essentially fatty acid free bovine serum albumin (A6003, Sigma, St. Louis, MO) in deionized water were titrated to different pH levels near the N-F transition (3.5, 4, 4.5) with HCl. Solutions were loaded into triple rinsed quartz cuvettes and evaluated by Circular Dichroism spectrography (J-815, JASCO Inc, Easton, MD) with a wavelength scan from 190-260 nm in triplicate. Internal heating elements in the J-815 were used to thermally denature dilute albumin solutions (0.005 wt%) at pH 7.4 to 60°C and 80°C.

### 3.2.3 Electrostatic Potential Calculations

A Python script was written to compute the electrostatic potential explicitly (including all water and counter ion molecules) at each point along the Connolly surface of the protein with the following equation:

$$\sum_i \frac{1}{4\pi\epsilon_0} \cdot \frac{Q}{r} \quad \text{Equation 3-1}$$

The Connolly surface was computed using the built in GROMACS g\_sas command with settings identical to those used by the program APBS<sup>165</sup> embedded in Chimera<sup>166</sup> that was used to generate the Poisson Boltzmann potential surface. The radius of the solvent probe was 1.4Å with 20 dots per sphere on the surface. A 3nm radius cutoff was used in calculating the electrostatic potential contribution of every atom near each mesh point. Visualizations of molecular structures are performed with the VMD 1.9.1 software package<sup>167</sup>.

## 3.3 Results

### 3.3.1 Protein protonation state at pH 3.5

Using the FAMBE-pH program, we calculated the ionization state of titratable residues (ASP, GLU, HIS, LYS, ARG) at pH 3.5. Residues with carboxylic acid groups that increase in charge state from -1 to 0 (ASP and GLU) between pH 7.4 and pH 3.5 are shown in red while residues with primary and secondary amines (LYS, ARG, and HIS) that increase in charge from 0 to +1 are shown in blue (Fig. 3.4). At pH 7.4, FAMBE-pH correctly predicted the deprotonation of all ASP and GLU residues: the protonation of all ARG and LYS residues, and a balance of protonated and deprotonated HIS residues and was consistent with an expected overall net charge of -9<sup>47</sup>. At pH 3.5, FAMBE-pH predicted that all ASP and GLU residues become protonated and that the remaining HIS residues also be protonated, while LYS and ARG residues remain unchanged (Fig. 3.4). The locations of these residues on BSA are distributed uniformly over the tertiary structure and represent the ionization state of BSA at pH 3.5 (net charge of +100). While these results effectively set the protein pH to 3.5, the conformational structure was still that of the N-form. This predicted net charge was higher than the net charge (+65) and effective charge (+13) for albumin molecules at pH 3.5, as determined by experimental titration and electrophoresis NMR experiments<sup>47,168</sup>, but this may be due to the fact that the structure of the protein was not yet in its ideal conformation. This difference can also be explained by the fact that any observable measurement should be computed from an ensemble of structures via a Boltzmann average; however, this is not feasible with the existent computational resources.

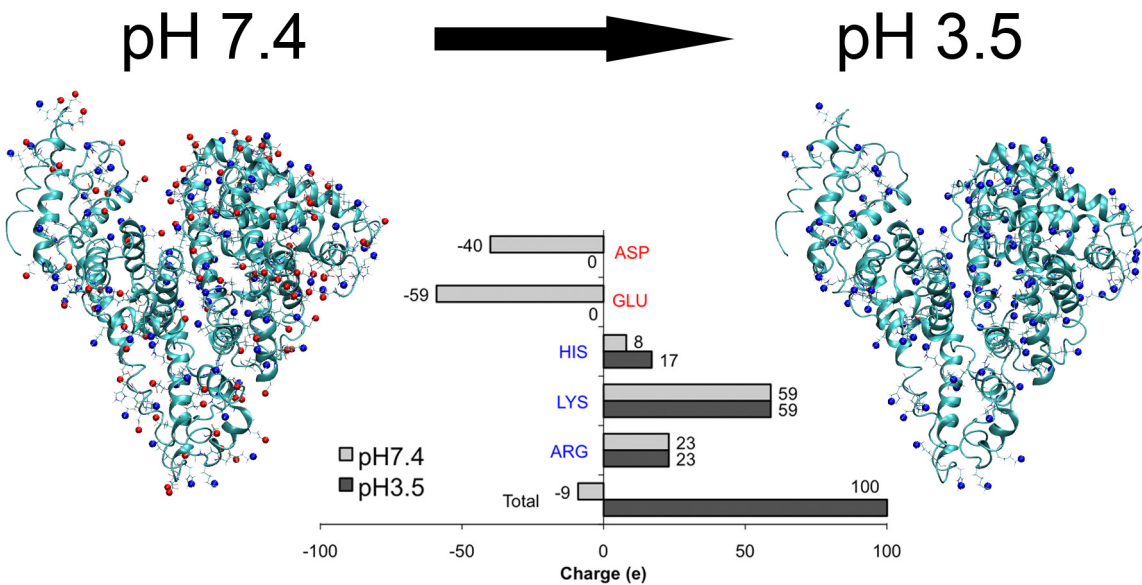


**Figure 3.4 Localization of ionized residues on albumin at pH 7.4 and pH 3.5. Chart shows the number of charge per residue type and the total for the entire protein at the two pH values. At pH 7.4, the protein has a total charge of -9 while at pH 3.5, the charge is +100 (including the amine terminal group).**

### 3.3.2 Molecular dynamics simulation of partial protein unfolding

Protonation of albumin to pH 3.5 placed many positive charges on both side of the interior of the globin fold between domains 1 and 3. During the simulation, we observed that these electrostatic repulsions between the three domains in the protein induced a conformational transition from the N-form to a conformation that appears very similar to the F-form. This is shown in the simulation snapshots for the time evolution of this process for the case where counter ions were present (Fig. 3.5). Within tens of nanoseconds, the distance between domains 1 (orange) and 3 (purple) has increased, with the area between domain 2 (green) and domain 3 acting as a hinge for the expansion as predicted in the literature<sup>169,170</sup>. After the initial expansion within this time, the conformation remained stable for up to 64 ns without significant conformational change (Fig. 3.6). A sample of the PDB file for F-form albumin can be found in

Appendix D. To quantify the simulated expansion, we measured the interdomain distances between center of mass of domain 1 and domain 3. Consistent with the simulation snapshots, the initial rate of protein expansion was ~1.2 nm/ns. Final interdomain spacing of albumin was found to increase from  $3.47 \pm 0.12$  nm (N-form) to  $7.26 \pm 0.32$  nm (F-form) (Fig. 3.7).

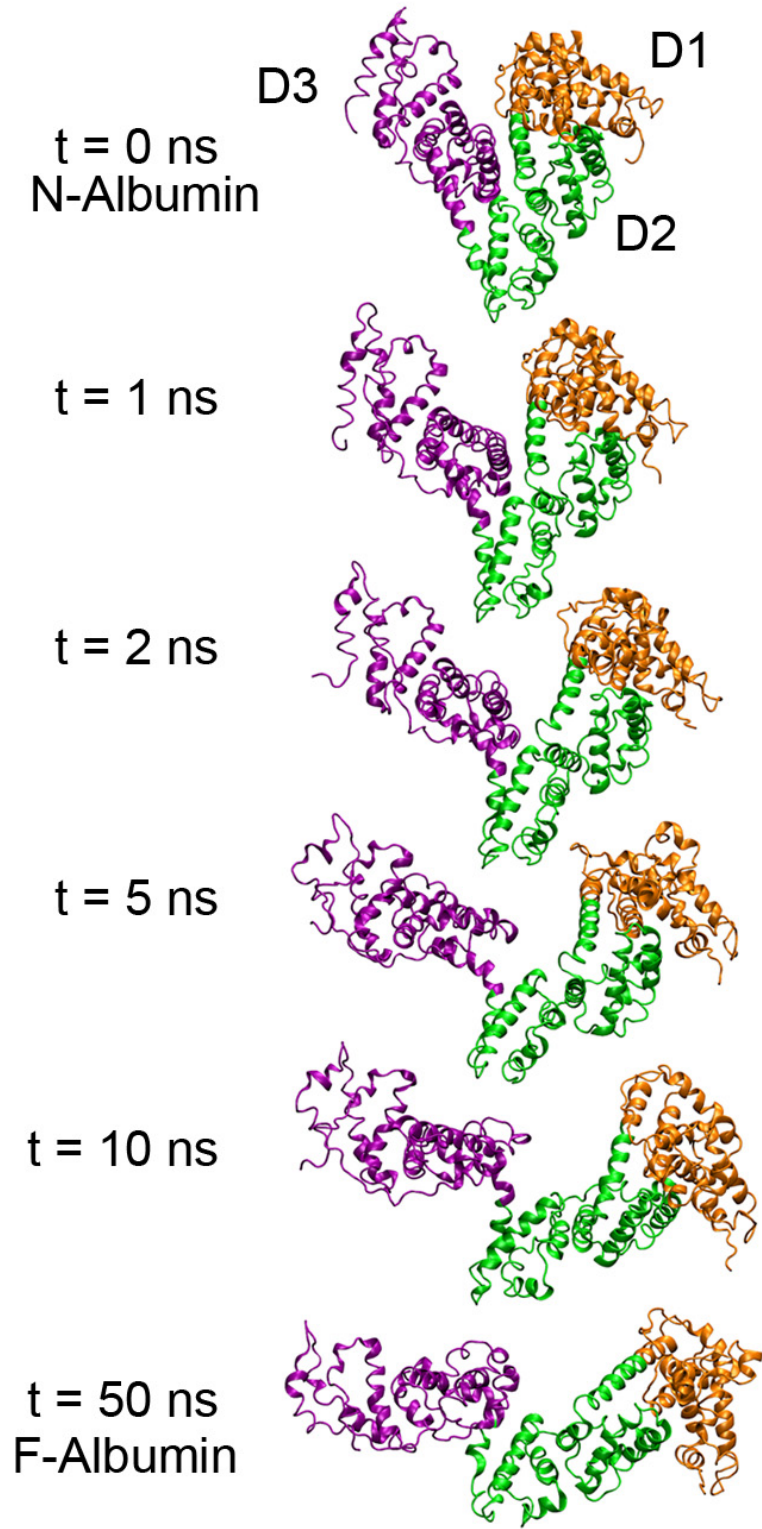


**Figure 3.5** Partial unfolding simulations of albumin with titratable residues set to pH 3.5 ionization states. Orange, green, and purple regions denote domains 1, 2, and 3 respectively. Snapshots of albumin conformations simulation during partial electrostatically-triggered denaturation.

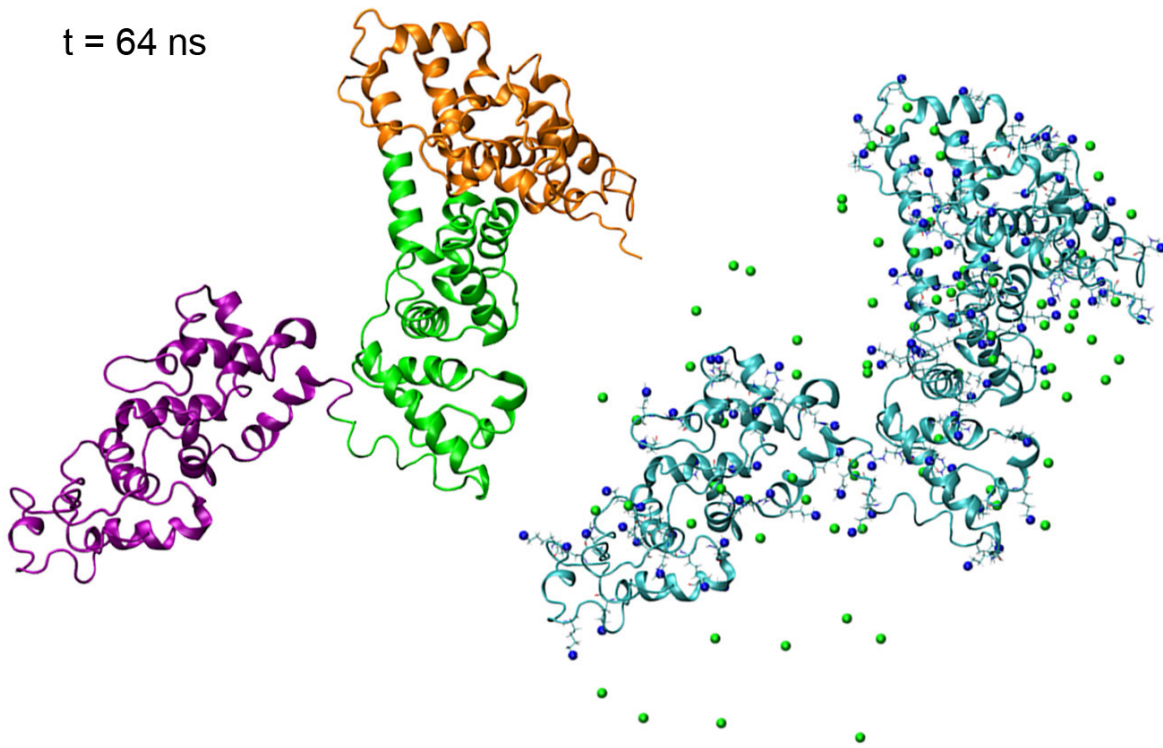


**Figure 3.6** Final simulation conformations of albumin at pH 3.5. Locations of positive charges and counter ions are represented on the right.

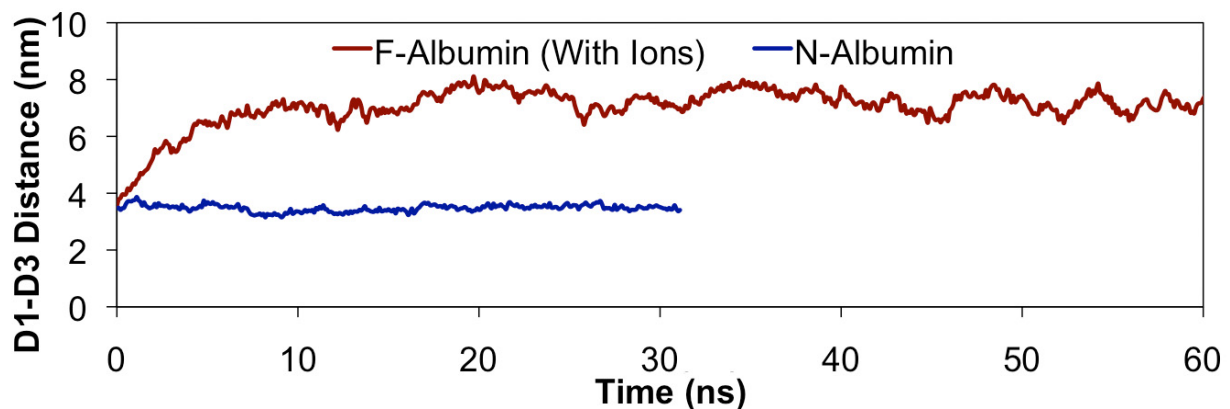


**Figure 3.7** Distance measured between the center of mass of domain 1 and domain 3 during simulations with counter ions (red) in comparison with physiological albumin at pH 7.4 (blue).

### 3.3.3 Secondary structure loss after partial unfolding

In addition to tertiary structural changes, the partial denaturation also resulted in a net loss of alpha helical secondary structure, from  $62.9\% \pm 2.9\%$  in the N-form to  $53.2\% \pm 2.2\%$  in the F-form (Fig 3-8). When resolved by domain, differences in the degree of secondary structure preservation emerged. Domain 1 was the most preserved with a non-significant ( $p>0.05$ ) decrease in alpha helical content from  $58.6\% \pm 3.8\%$  in the N-form to  $55.8\% \pm 2.4\%$  in the F-form. In contrast, both domains 2 and 3 had significant ( $p<0.01$ ) decreases in helical content (domain 2: N= $69.3\% \pm 3.8\%$  to F= $57.7\% \pm 3.7\%$  and domain 3: N= $61.0\% \pm 2.8\%$  to F= $46.6\% \pm 3.9\%$ ). Alpha helical signatures calculated from simulations was consistent with the presence of alpha helical signatures measured experimentally *via* circular dichroism spectroscopy at different pH values (3.5, 4, and 4.5) in the F-form range (Fig. 3-9, blue curves). In contrast, circular dichroism data for thermally denatured albumin near the limit ( $60^\circ\text{C}$ ) and above ( $80^\circ\text{C}$ ) albumin's denaturation temperature, revealed complete or near complete loss of all native secondary structures (Fig 3-9, red curves). Complete thermal denaturation curves can be found in Appendix E. Persistent secondary structural content in pH denatured albumin supports the notion that this partial denaturation pathway does not require disruption of the entire protein as in the case for thermally denatured albumin.

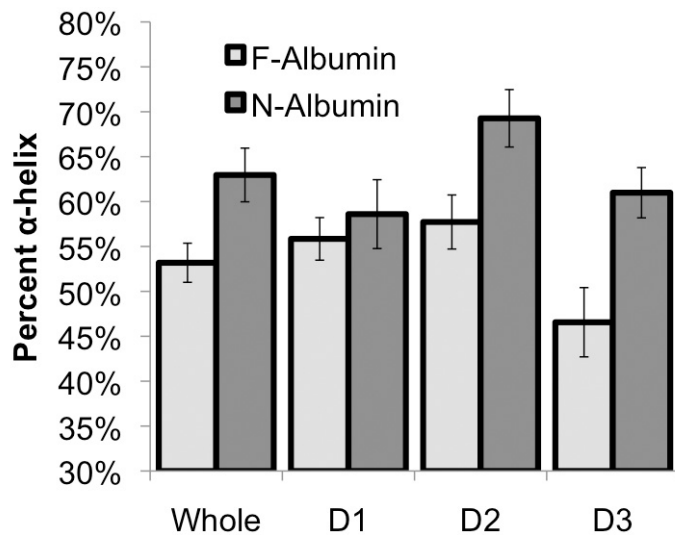


**Figure 3.8 Percentage of helices in each domain for both N- and F-forms. All F domains loose a fraction of their helical content to turn/coil structures during the partial denaturation in comparison to N conformations.**

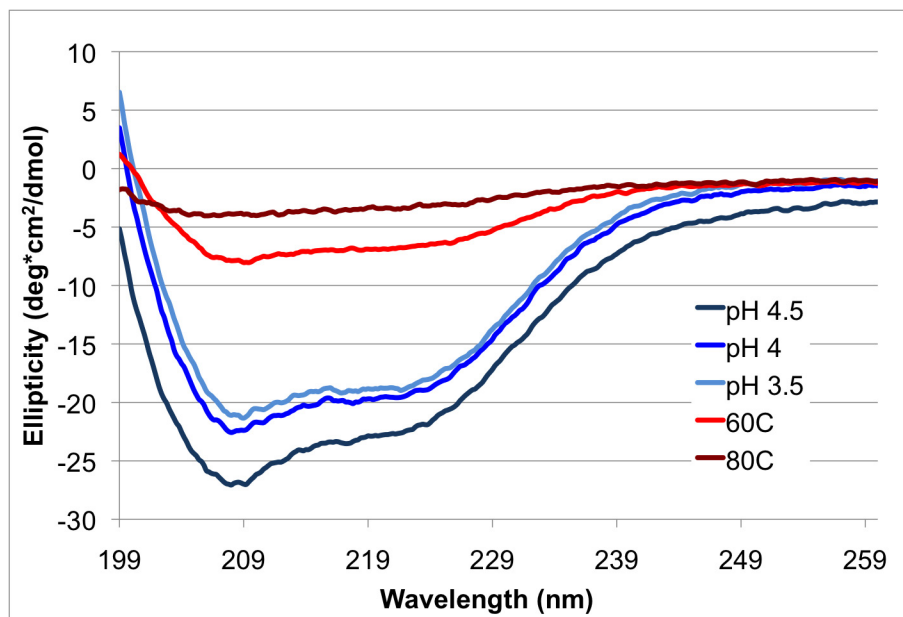


**Figure 3.9 Circular Dichroism data of dilute solutions of BSA (0.005 wt%) at low pH and high temperature showing the relative degree of secondary structure denaturation. Electrostatically triggered denaturation avoids the total loss of secondary structures as observed in thermal denaturation.**

### 3.3.4 Hydrophobic solvent accessible surface area calculation

We explored the effects of the N-F transition at the individual residue level by measuring the change in solvent exposed area of hydrophobic residues. This analysis provided insight to changes in hydrophobic surfaces that could help explain the observed protein aggregation. The hydrophobic SAS for domains 1, 2, and 3 in the F-form was  $0.0362 \pm 0.0007 \text{ nm}^2/\text{atom}$ ,  $0.0406 \pm 0.0009 \text{ nm}^2/\text{atom}$ , and  $0.0388 \pm 0.0011 \text{ nm}^2/\text{atom}$  respectively. In the N-form, the hydrophobic SAS for domains 1, 2, and 3 was  $0.0333 \pm 0.0008 \text{ nm}^2/\text{atom}$ ,  $0.0361 \pm 0.0008 \text{ nm}^2/\text{atom}$ , and  $0.0355 \pm 0.0007 \text{ nm}^2/\text{atom}$  respectively. The analysis showed that all three domains have a statistically significant ( $p < 0.0001$ ) increase in the SAS area of hydrophobic residues during the N-F transition (Fig. 3.10). The increases for each domain was domain 1:  $0.0028 \pm 0.0016 \text{ nm}^2/\text{atom}$ ; domain 2:  $0.0045 \pm 0.0018 \text{ nm}^2/\text{atom}$ ; domain 3:  $0.0033 \pm 0.0019 \text{ nm}^2/\text{atom}$  during the N-F transition. In contrast, the SAS area of hydrophilic residues decreased significantly during the N-F transition. Hydrophilic SAS for domains 1, 2, and 3 in the F-form was  $0.0550 \pm 0.0010 \text{ nm}^2/\text{atom}$ ,  $0.0549 \pm 0.0012 \text{ nm}^2/\text{atom}$ , and  $0.0524 \pm 0.0011 \text{ nm}^2/\text{atom}$  respectively. In the N-form, hydrophilic SAS for domains 1, 2, and 3 was  $0.0576 \pm 0.0010 \text{ nm}^2/\text{atom}$ ,  $0.0548 \pm 0.0010 \text{ nm}^2/\text{atom}$ , and  $0.0760 \pm 0.0009 \text{ nm}^2/\text{atom}$  respectively (Fig. 3.11). For the protein overall, the hydrophobicity increased by 16% and the hydrophilicity decreased by 13%.

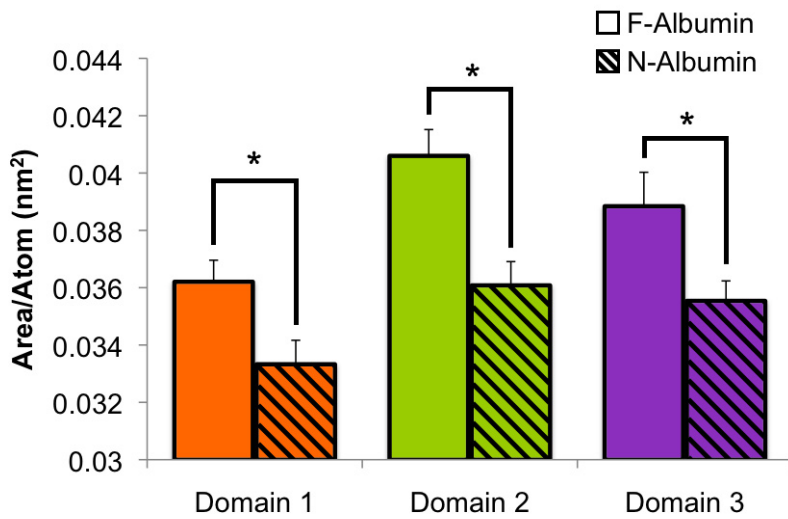


**Figure 3.10** Solvent accessible surface areas for hydrophobic moieties in the N- and F-forms represented for each domain individually. Each difference is statistically significant to  $p < 0.0001$ .

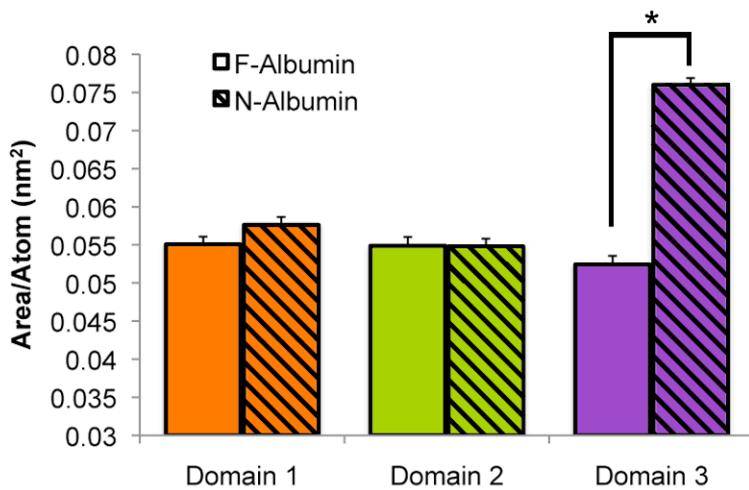


**Figure 3.11** Solvent accessible surface areas for hydrophilic moieties in the N- and F-forms represented for each domain individually. Each difference is statistically significant to  $p < 0.0001$ .

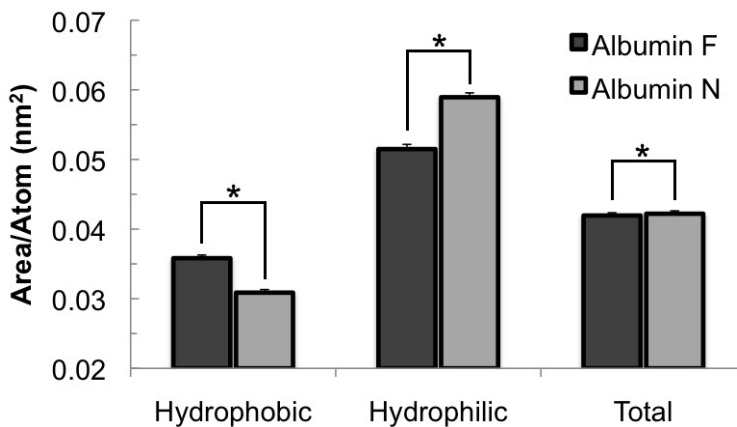


**Figure 3.12 Solvent accessible surface area for hydrophobic, hydrophilic, and all residues. N-F transition causes the protein to become more hydrophobic without change in total average surface area per residue.**

The total SAS area measurements when both hydrophobic and hydrophilic residues are taken together can be used to infer whether the individual domains are expanding or collapsing (Fig. 3.12). The difference in domain 1 was modest ( $N=0.0429 \pm 0.0007 \text{ nm}^2/\text{atom}$ ,  $F=0.0436 \pm 0.0007 \text{ nm}^2/\text{atom}$ ). This small change is consistent with the earlier result that the change in alpha helical content was not significantly different between the two isoforms (Fig. 3.8). However, the domain 2 expanded ( $N=0.0435 \pm 0.0007 \text{ nm}^2/\text{atom}$ ,  $F=0.0462 \pm 0.0009 \text{ nm}^2/\text{atom}$ ) and domain 3 collapsed ( $N=0.0524 \pm 0.0006 \text{ nm}^2/\text{atom}$ ,  $F=0.0441 \pm 0.0009 \text{ nm}^2/\text{atom}$ ) to a greater degree during the transition. The greatest loss in hydrophilicity was found in domain III, consistent with large structural changes observed in this domain both visually (Fig. 3.6) and in helical content (Fig. 3.8).

### 3.3.5 Preferential domain 3 unfolding during N-F transition

The loss of structure in domain 3 is likely due to several reasons; first, is the fact that ASP and GLU residues are protonated at pH 3.5 and thus, less hydrophilic, and second, is the

greater loss of secondary structure in domain 3. Taken together, these two effects allow ASP and GLU residues to become buried, reducing their SAS area contribution (Fig. 3.13). While ASP and GLU residue SAS areas decrease in every domain, they account for a larger fraction of SAS in domain 3 as they are disproportionately represented in this domain, making these effects more noticeable. On the whole, the protein is more hydrophobic in the F-form than in the N-form. The increases in hydrophobic SAS area and decreases in hydrophilic SAS area suggest that aggregation of F-form BSA molecules in high concentrations may be due to intermolecular hydrophobic interactions.

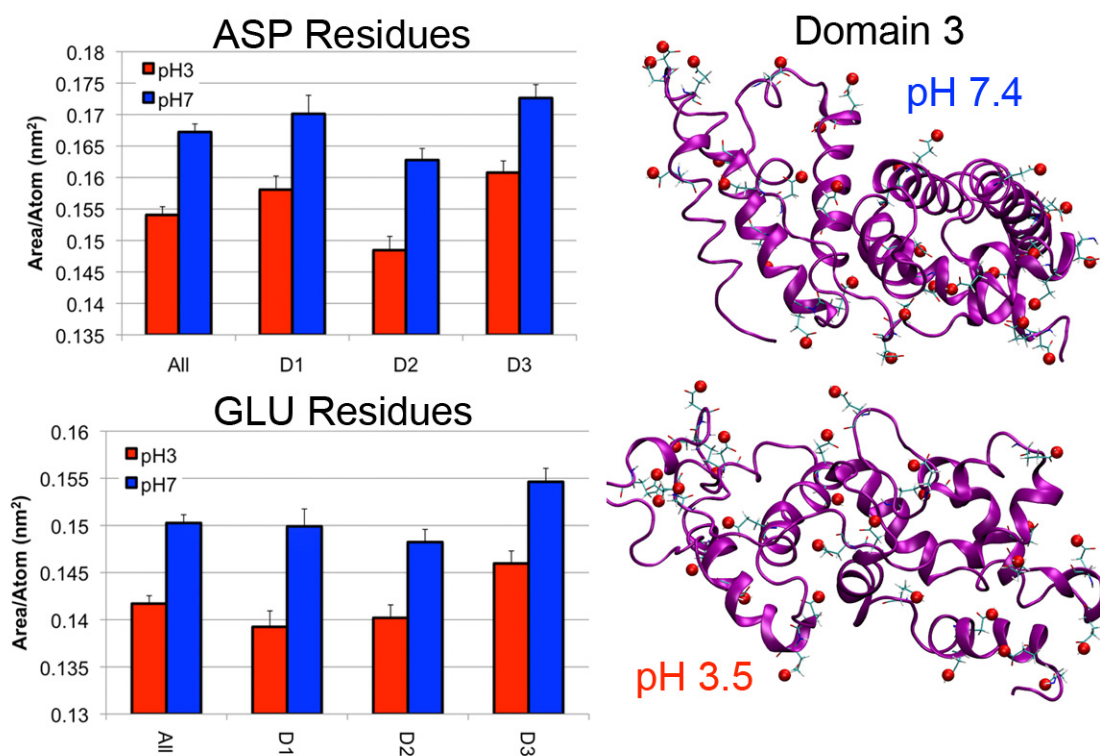


**Figure 3.13 Solvent accessible surface areas for ASP and GLU residues in the N- and F-forms in the total protein and in each domain. Normally hydrophilic residues ASP and GLU face the solvent at pH 7.4 but are hydrophobic when protonated at pH 3.5.**

### 3.3.6 Dimeric protein interaction and molecular dynamics

To explore the early stages of protein aggregation, we investigated the interactions between two proteins using our new F-form albumin models. We placed two of these configurations in contact such that their newly exposed hydrophobic surfaces (located primarily along the globin fold), as determined by the increase in local hydrophobic SAS, were facing each other (Fig. 3.14). We used the presence or absence of counter ions in the system to screen out electrostatic interactions between the proteins. As expected, in the absence of counter ions, large electrostatic repulsions between the proteins forced them to move away from each other soon after overcoming the initial contact attraction (Fig. 3.14a, red). In the presence of counter ions necessary to maintain system electroneutrality ( $200 \text{ Cl}^-$ ), the two proteins stayed within  $0.25\text{nm}$  of each other, as indicated by the minimum distance measured between the two proteins (Fig. 3.14a, black). The persistent point of contact between the two proteins was located in domain 2 but this may be an artifact of the initial protein placement and nearby available contacts (Fig. 3.14b, blue arrow). Interestingly, after 36 ns, the two proteins separated from each other. This suggests that the attraction observed between the two proteins may be the result of a local minimum in the free energy as a result of the increased hydrophobicity. However, this would have to be corroborated through additional simulations.

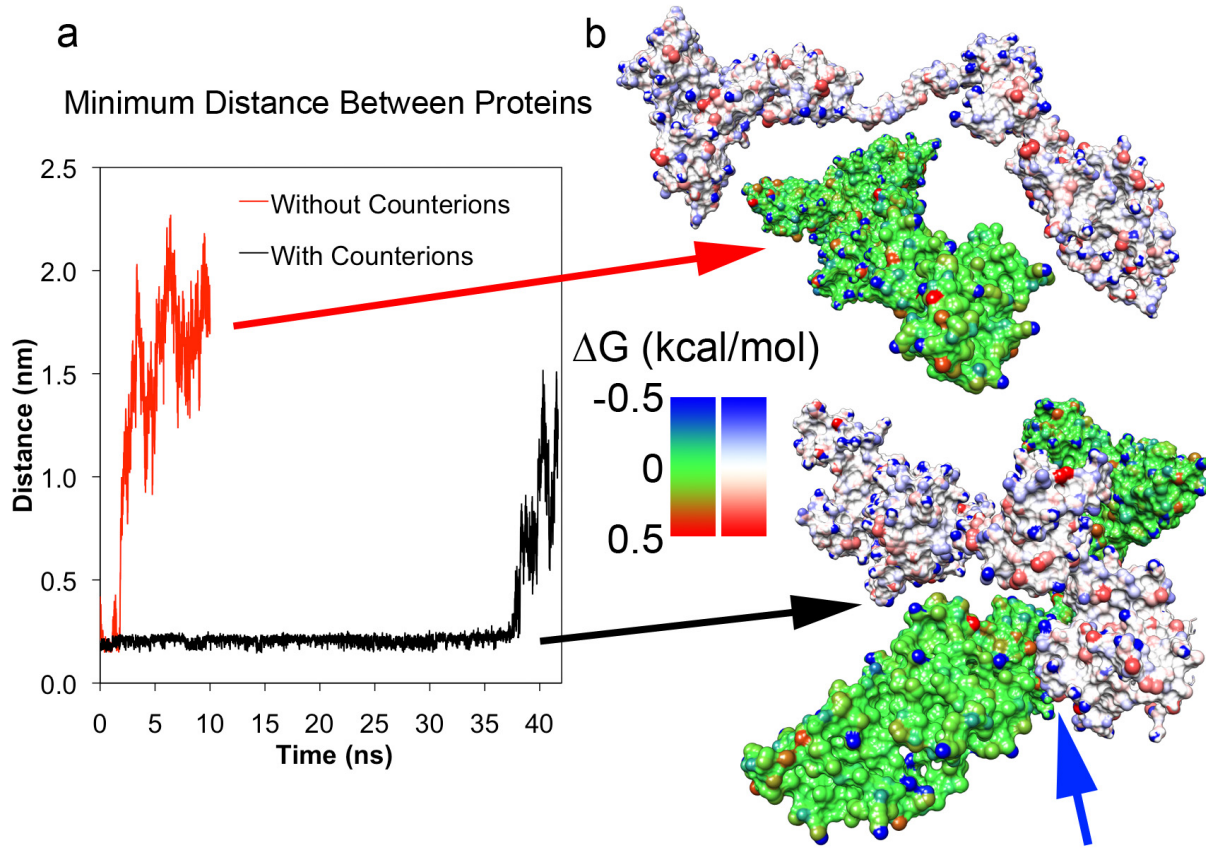


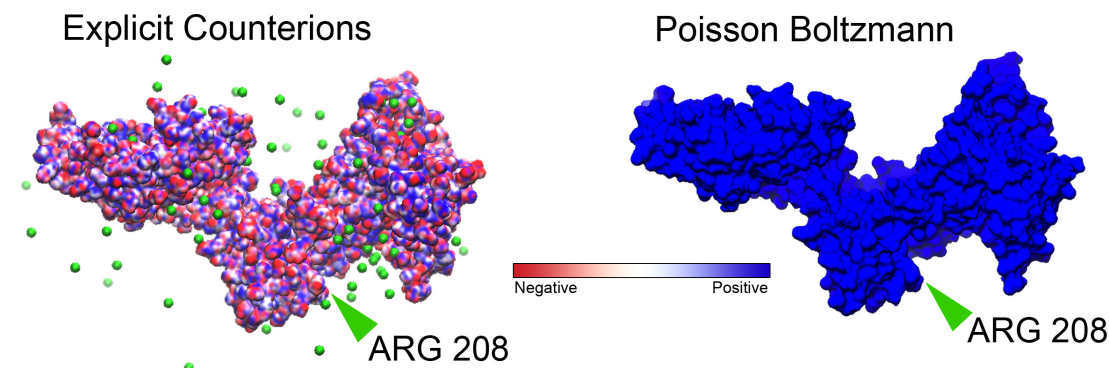
**Figure 3.14 Dimerization of two F conformation albumin proteins.** (a) Minimum distance measured between two F-form BSA structures placed near each other and simulated with and without system neutralizing counter ions. Proteins with counter ions allowed proteins to stay within 0.25nm of each other (black line) until they separated after 36ns. Absence of counter ions allowed unscreened repulsive electrostatic interactions to rapidly overcome attractions (red line). (b) Configurations of two proteins from (a) at 10 ns. The top pair (green protein and white protein) corresponds to the no counter ion simulation and the bottom pair corresponds to the counter ion simulation. Individual surface atoms are colored by the change in free energy due to solvation in water (kcal/mol). Hydrophobic and hydrophilic atoms are colored red and blue respectively. The blue arrow indicates the point of contact between the two proteins.

### 3.3.7 Single protein electrostatic surface energy potential calculation

Calculation of the electrostatic surface energy potential provides another method for evaluating the intermolecular interactions. The usual way to determine electrostatic potentials in proteins is by solving the Poisson-Boltzmann (PB) equation. However, it is not clear how good the mean-field approximation would be in a system with such larger number of charges.

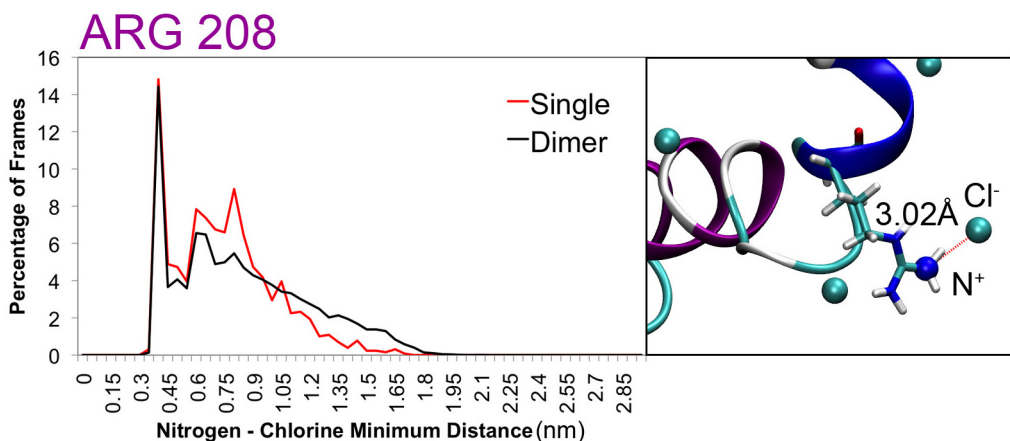
Therefore, we performed PB calculations and explicit determination of the electrostatic potentials from the findings of the positions of all the molecules, including the ions, from the simulations. The python script for this calculation can be found in the Appendix A. Use of this script requires a PDB file which explicitly states the partial charge for every atom in the system. Explicit electrostatic potential calculations that factor in the contribution of counter ions in the system results in surface potentials that are more negative when compared to the result from PB (Fig. 3.15). Particularly interesting is the fact that in the scale shown in Figure 3.15, the PB results show an almost constant, relatively high, positive potential that directly reflects the charge on the proteins, i.e. the +100 that result from the low pH. In sharp contrast, the explicit calculations demonstrated relatively large, variations of the electrostatic potential across the protein surface, showing that the explicit positions of the counter ions plays a dramatic role in determining the structure and interactions of proteins. This is very important since the PB calculations would suggest strong attractive interactions between the protein (anywhere on its surface!) and negatively charged molecules, or surfaces. On the other hand, the full calculations show a much more complex surface that could lead to a variety of possible interactions.

## Single Protein



**Figure 3.15 Explicit counter ion and PB calculated electrostatic surface potentials for single F-form albumin. Explicit counter ion calculations result in a more negative electrostatic potential when compared to PB. Residue ARG 208 has a positive potential when calculated with PB and a negative potential when calculated with explicit counter ions.**

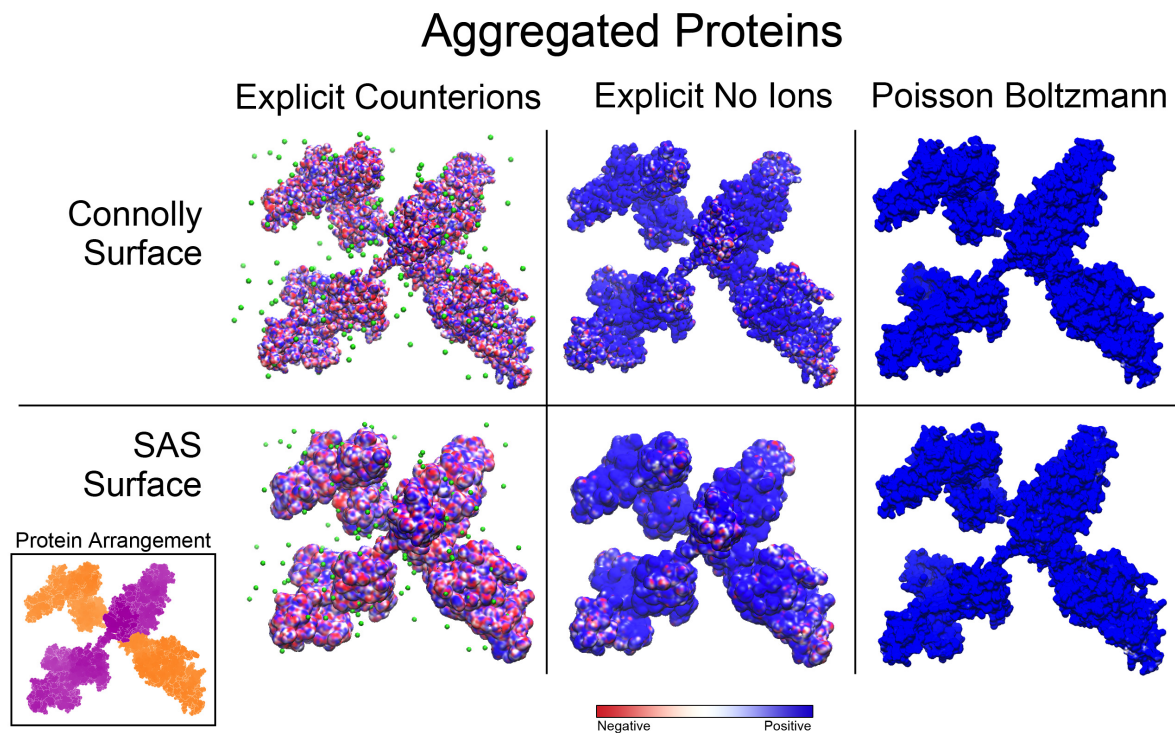
While in many cases the PB calculation is sufficient, it misses many important details regarding the effect of individual counter ions in highly charged systems. For example, at residue ARG 208 (Fig 3.15, green arrow), PB predicts the nitrogen atom to have a positive electrostatic potential. In fact, the explicit calculation indicates the potential is negative due to the attraction of a neighboring  $\text{Cl}^-$  counter ion (Fig 3.16). A histogram of the distances to the nearest  $\text{Cl}^-$  ion for the charged  $\text{N}^+$  atom on ARG 208 demonstrates that this residue is typically bound to a counter ion throughout the simulation (Fig. 3.16).



**Figure 3.16** A histogram of the distances to the nearest  $\text{Cl}^-$  ion for the charged  $\text{N}^+$  atom on ARG 208 demonstrates that this residue is typically bound to  $\text{Cl}^-$ .

### 3.3.8 Two protein electrostatic surface energy potential calculation

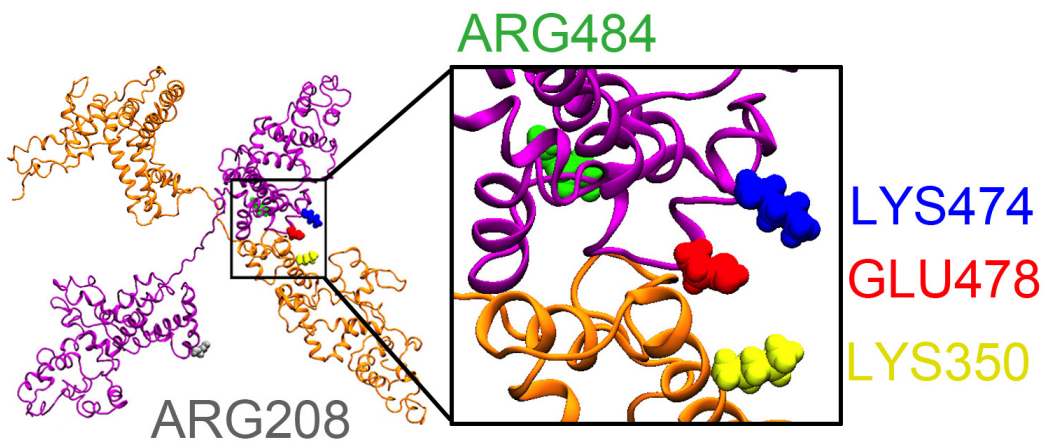
In the case of two proteins interacting with each other, we observed similar effects of the electrostatic surface potential calculation as in the single protein case (Fig. 3.17). To underscore the important contribution of these counter ions to the interpretation of the electrostatic potential, we also computed the explicit electrostatic potential while ignoring the counter ions present (Fig. 3.17, center). This counter ion-free explicit calculation resulted in a relatively high, positive potential similar to the one calculated by PB (Fig. 3.17, right). We also show the potentials calculated at two different distances from the protein surface; the Connolly surface (0.14nm) and the SAS surface (1.4nm) to demonstrate how the potential becomes more negative as we move away from the positive charges on the protein. This detail is largely lost in the PB calculation where the effects of numerous positive surface charges persist for greater distances.



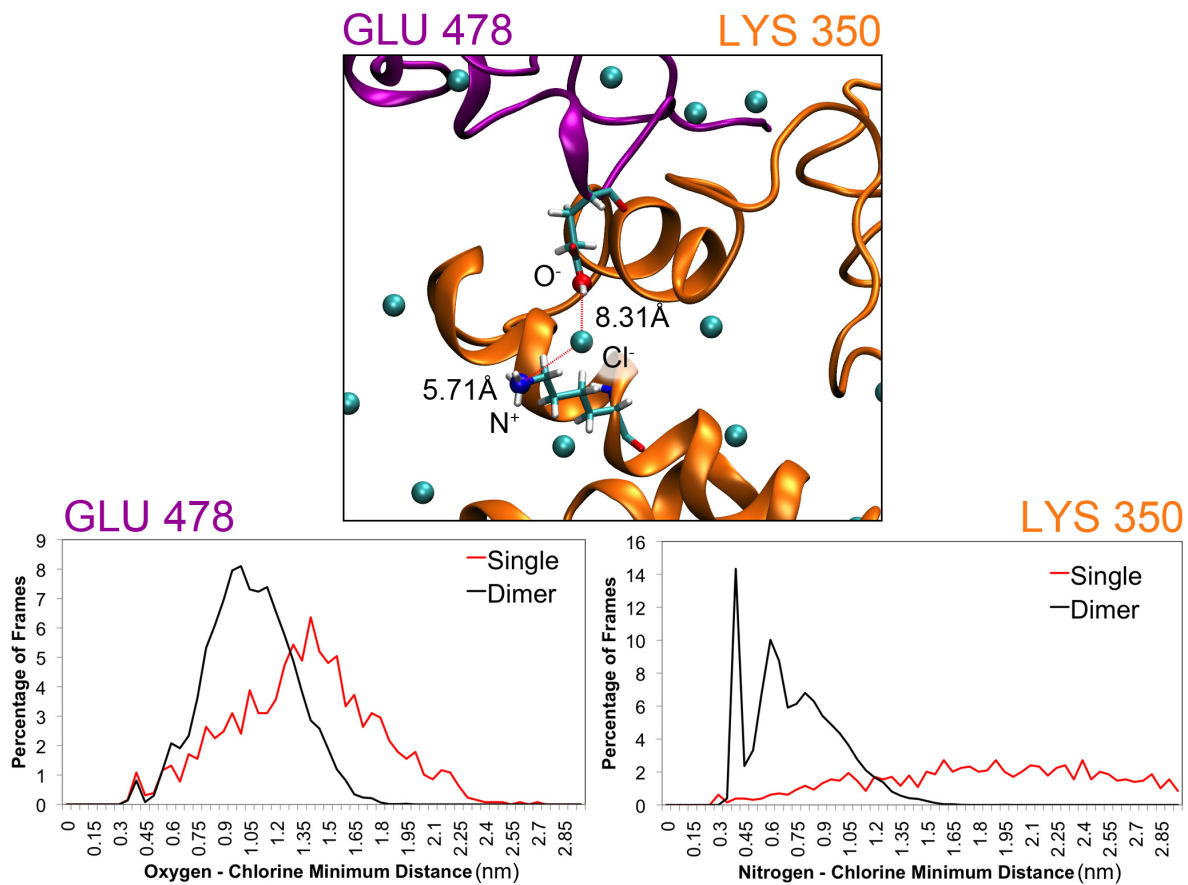
**Figure 3.17** Explicit counter ion and PB calculated electrostatic surface potentials for two aggregated proteins. Explicit counter ion calculations (left) result in a more negative electrostatic potential when compared to PB (right). Explicit calculations that ignore counter ion contributions (center) are very similar to the positive electrostatic potentials shown by PB. Potentials at the Connolly and SAS surfaces are shown for all cases. For clarity, aggregated proteins are colored individually (inset, orange and purple) to help differentiate them in the potential surface representation.

Four additional residues at the point of contact between the two proteins are highlighted for further analysis (Fig. 3.18). All four (and two in particular, LYS 350 and LYS 474) rarely had any associated counter ions in the single protein case. But, when brought into contact with another highly charged protein, all four residues were substantially more likely to have counter ions present (Fig. 3.19). Both LYS 350 and LYS 474 were rarely seen without a counter ion present after dimerization. In the case of GLU 478 and LYS 350, a chlorine ion was found close to both proteins (orange and purple). While there are many other positively charged surface

residues on both proteins, not all of them recruited counter ions as was the case for LYS 350 and LYS 474. This is due to the inherent entropic cost of binding every free counter ion with every positively charged residue but it becomes more likely when the proteins are dimerized. The increased likelihood of finding nearby counter ions in the dimerized state suggests the attraction of these counter ions is necessary to neutralize residue charges and promote protein aggregation.



**Figure 3.18 Localization of residues selected for further analysis. ARG 208 is shown in silver. Inset depicts ARG 484 (green), LYS 474 (blue), GLU 478 (red), and LYS 350 (yellow) are all located near the point of contact between the two proteins (orange and purple).**



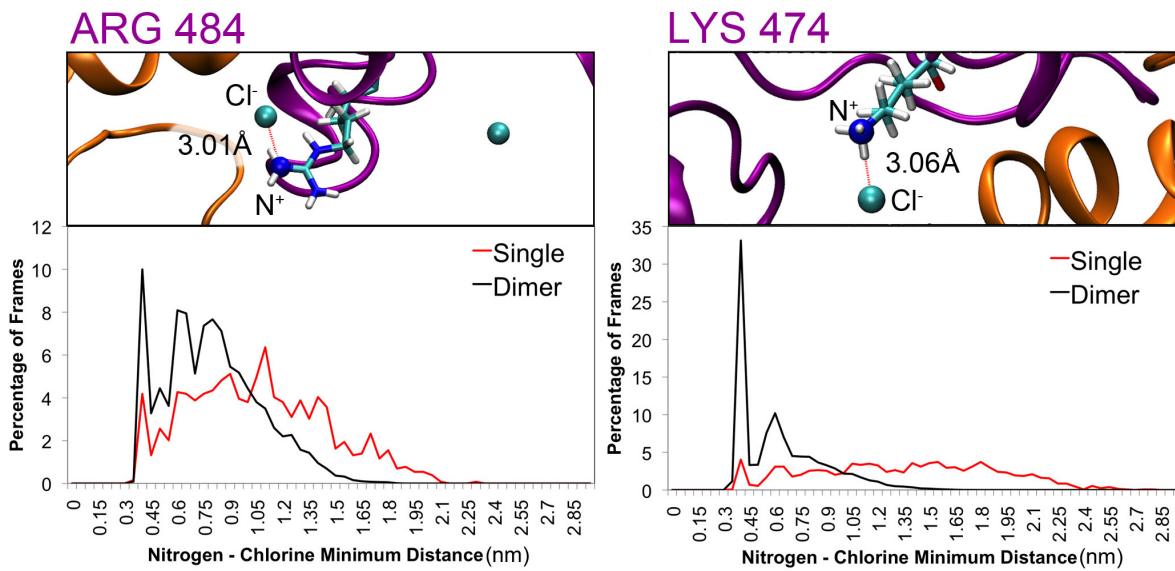


**Figure 3.19** Histograms of distances to nearest  $\text{Cl}^-$  ions for the four selected residues ARG 484, LYS 474, GLU 478, and LYS 350 near the point of contact in d and magnified representations of charged atoms associated with  $\text{Cl}^-$ . Orange and purple coloring of residue names indicate which protein the residue is from.

### 3.4 Discussion

While the atomic structure of human albumin at pH 7.4 had been determined at a  $2.5\text{\AA}$  resolution<sup>148</sup>, the atomic structure of pH 7.4 bovine albumin was elucidated to a  $2.47\text{\AA}$  resolution only recently<sup>149</sup>. Much is known about the behavior of both albumins at this physiological pH ranging from 78 separate reports of named site mutations<sup>34</sup> to interspecies allergenic potential<sup>171</sup>. However, outside this physiological pH condition, only low-resolution 3D models, based on small angle X-ray scattering (SAXS) data exist for the F-form<sup>43</sup>. Literature reports of albumin at the low pH range typically describe only the fact that there exists an N-F transition as described in early work by Foster<sup>103</sup> and characterize elements of this transition such as the hydrodynamic

radius of certain fragments<sup>102,151</sup>, adiabatic compressibility<sup>150</sup>, NMR chemical shifts<sup>101</sup>, and secondary structure content by circular dichroism<sup>151</sup>.

It has been noted that the conserved homology between albumins in several species<sup>40,171,172</sup> (Appendix B) has exhibited the conservation of the N-F transition which is itself suggestive of an important physiological role<sup>150</sup>. Since there is no albumin crystal structure available at low (or even high) pH value, the community's understanding of the conformational changes is limited. This work addresses that gap by developing an accurate crystal structure for albumin at pH 3.5 using molecular dynamics simulations and studying protein aggregation of F-form bovine serum albumin. Recent advances in computational power, MD software<sup>159</sup>, and theoretical methods to calculate titration states of residues in large proteins<sup>155</sup> now enable us to simulate these conformational changes from first principles. Since the size of the simulations required to model pH atomistically in this system remains prohibitively expensive, we utilized a program called FAMBE-pH to calculate the total solvation free energies of proteins as a function of pH<sup>155</sup>.

The resulting crystal structure of F-form bovine serum albumin captures many elements detailed and predicted in the literature. Several groups first predicted and then showed direct evidence that the initial denaturation occurs primarily in domain 3<sup>35,38,169,170,173</sup>. Later, Dockal et al.<sup>151</sup> proved that the N-F transition originates in the structural destabilization at the C-terminus in domain 3 based on circular dichroism and fluorescence spectra analysis of albumin domain fragments. This feature of the N-F transition is captured in our simulations (Fig. 3.5) and confirms the experimental observations by other groups.

The loss of secondary structural content has also been described in the literature<sup>35,38,151</sup>.

Analysis of the secondary structure content for our F-form BSA model captures the loss in secondary structure content in domains 2 and 3 while conserving it in domain 1 (Fig. 3.8). For the purpose of designing a drug delivery system, the preservation of these secondary structures bodes well for their retained functionality to binding therapeutic molecules, particularly for drugs that utilize binding sites in domain 1 (See Chapter 5 for studies involving drug interactions).

Two protein simulations described the potential early stages of F-form aggregation. Over time, the proteins remained close together and recruited counter ions to charge concentrated regions between them (Fig. 3.19). However, with the two protein arrangement, the effective concentration of albumin in water in this simulation was ~7mg/mL, substantially lower than the experimentally observed threshold for gelation (15 mg/mL, see Chapter 4) but sufficient for examining the early interaction between two proteins. Extended simulations after 36 ns showed separation of two proteins suggesting a local free energy minimum for the aggregated state with two proteins at sub-threshold concentrations. Larger simulations with more than 4 interacting proteins would be necessary to meet the threshold concentration but are computationally demanding to perform.

Thus far, these observations support the notion that hydrophobic interactions from the protein core and counter ion association to charged residues at the proteins point of contact drives the self-assembly of the hydrogel network. As hypothesized, the electrostatically driven denaturation observed in these fully atomistic BSA simulations captures the conformational structures and denaturation behavior predicted by others in the literature<sup>38,43</sup> but with a much greater accuracy.

### 3.5 Conclusions

Our results provide insights into what are the interactions necessary to overcome the highly charged nature of the F-form in forming protein aggregates. When the individual proteins are highly charged, strong intramolecular electrostatic repulsions trigger a partial denaturation of the protein. We used FAMBE-pH to calculate the total solvation free energy of the protein as a function of pH and determined the probability of residue ionization on albumin. Lowering the solution pH to 3.5 and simulating with molecular dynamics enables albumin to make the N-F transition in a manner that is driven by electrostatic repulsions and that results in the exposure of core hydrophobic regions. These hydrophobic regions are critically involved in the aggregation of the proteins despite the electrostatic repulsions still present between proteins. Interprotein electrostatic repulsions are mitigated by the attraction of counter ions to charged residues at the point of contact. An explicit counter ion calculation of electrostatic surface potentials provides new insights that were missed by conventional PB calculations. Solving the electrostatic surface potential with explicit consideration of counter ions may be a useful approach in other protein and drug binding studies. Analysis of the protein conformation reveals that alpha helical structures in domain 1 are preserved and that the total secondary structural content is more preserved when compared to thermally denatured albumin gels. This improved understanding of partially denatured albumin conformations, puts us in a better position to harness these electrostatically triggered hydrophobically self-assembled protein gelation mechanisms to reveal new solutions to longstanding problems in drug delivery and unwanted protein self-assembly, e.g. amyloid formation.

## CHAPTER 4: HYDROGEL FORMATION AND CHARACTERIZATION

### 4.1 Objective

The process of protein aggregation is governed by the balance between repulsive and attractive interactions between proteins<sup>126</sup>. In this Chapter, we build upon the work others have done on early stage low pH albumin aggregation in concentrations below 10 wt%<sup>107,123,174,175</sup>. We have shown in Chapter 3 how protonated residues generate repulsive electrostatic forces that partially denature albumin. This process then increases the protein's solvent exposed hydrophobic surface area, which then serves as an attractive force between two or more proteins in solution. Others have reported on similar balances between repulsive and attractive forces that induce aggregation by modifying surface charges, salt concentrations, or temperature<sup>126,176</sup>. While these systems form aggregates and gels (when above a critical concentration), they all require a thermal denaturation step as a requisite for aggregation<sup>3,126,177</sup>. In doing so, we have shown that residual alpha helical secondary structure in the protein will be lost (Fig. 3.9). The loss of these structures can lead to a loss in the intrinsic binding affinity of albumin for specific therapeutic molecules. **Our objective in Chapter 4 is to find the optimal conditions to fabricate albumin hydrogels without thermal denaturation.** By avoiding thermal denaturation approaches, the resulting hydrogel should only be fabricated from partially denatured albumins and retain secondary structure content. Early stage aggregation between partially denatured albumin moieties will eventually form a percolating network once the concentration of the system increases past a critical concentration. We hypothesize that by increasing the

concentration of protein in solution, we will be able to form albumin hydrogels via the electrostatically-mediated mechanisms described in Chapter 3.

## 4.2 Experimental section

### 4.2.1 BSA hydrogel fabrication

BSA hydrogel precursor solutions were formed by adding deionized water to essentially fatty acid free bovine serum albumin (A6003, Sigma, St. Louis, MO) in concentrations ranging from 9-20 wt% (1.4-3 mM). Solutions were stirred at 200-300 RPM until complete dissolution (~2-4 hours). After complete dissolution of the albumin, the solution was transferred to a fresh beaker to eliminate any bubbles.

#### 4.2.1.1 PBSA hydrogels

To form pH-induced bovine serum albumin (PBSA) hydrogels, the pH of the precursor solution was lowered to pH 3.5 by dropwise addition of 2M HCl with constant stirring. Immediately after addition of an HCl drop, the turbidity of the solution rises sharply. Since this turbidity can promote the formation of bubbles and stable white aggregates of denatured albumin, a wait time of several seconds was introduced until the turbidity of the solution dissipated before adding more HCl. The acidic BSA solution will slowly form a gel if left undisturbed for 48 hours. This gelation process is normally sped up to approximately 30 minutes when placed in a water bath at 37°C.

#### 4.2.1.2 TBSA hydrogels

To make the thermally denatured bovine serum albumin (TBSA) hydrogel, the BSA precursor solution was neutralized to pH 7.4 by dropwise addition of 2M NaOH followed by submersion in a water bath at 60°C or 80°C.

To eliminate any change in mechanical properties due to evaporative water loss during heating, gels fabricated for mechanical characterization were protected by overlaying the solution with a layer of pump oil (VWR, West Chester, PA) dyed with Oil red O (Sigma, St. Louis, MO). Precursor solutions intended for use *in vitro* and *in vivo* implantation were sterilized by passing them through a 0.2 µm nylon syringe filter (Fisher Scientific, PA).

#### 4.2.2 Hydrogel degradation

A 1 cm thick layer of PBSA was fabricated, acid leached in DMEM, and cut into cylinders with a .75 cm cylindrical punch. The cylinders were placed in different solvents (DI H<sub>2</sub>O, HCl-H<sub>2</sub>O, PBS, NaOH-H<sub>2</sub>O, 8M urea, 10% SDS, β-ME, and 10% BSA solution) to measure the degradation rate of the PBSA gels over time. Batches of 4 cylinders each were placed in individual wells of a 24-well plate and incubated with the different solvents. Solutions were changed repeatedly as adsorbed DMEM from the PBSA gels leached out into the solvents. Photographs were taken over a period of three months to document the extent of PBSA gel degradation.

#### **4.2.3 Transmission electron microscopy (TEM) Imaging**

Dilute solutions of BSA (2 wt%) at different pH values were imaged using a JEOL 1230 TEM system (JEOL Ltd., Tokyo, Japan) to evaluate any conformational changes of the BSA protein. Drops of BSA solutions were added onto formvar coated copper TEM grids and wicked off with filter paper. Uranyl Acetate (2%) was used as a negative stain for the protein. Images were captured with an Orius SC 1000 CCD camera system (Gatan, Inc. Pleasanton, CA).

#### **4.2.4 Scanning electron microscopy (SEM) Imaging**

PBSA gel samples were made following the standard procedure at 20 wt%, dehydrated through a series of graded ethanol solutions, and lyophilized (FreeZone Plus, Labconco, Kansas City, MO). Desiccated PBSA gels were loaded onto SEM sample stubs and coated with an 8 nm layer of OsO<sub>4</sub> (Osmium Plasma Coater Model OPC-60A, Filgen, SPI, West Chester, PA) before imaging with a Hitachi S-4800 FE-SEM (EPIC, Northwestern University, IL).

#### **4.2.5 Cryo-SEM Imaging**

Traditional SEM imaging requires desiccation of samples to prevent contamination of the SEM system. Unfortunately, compliance with this requirement leads to a collapsed hydrogel structures that may no longer resemble the original hydrated gel. Thus, a Cryo-SEM system at the Technion was used to observe the conformational structure of the BSA gel after formation while preserving the hydrated state of the gel<sup>178</sup>. PBSA and TBSA gels were vitrified with a CEVS (custom built courtesy of the Talmon Group, Technion, IL), freeze fractured and freeze

etched (BAL-TEC BAF060, Austria). Cryo-SEM imaging was performed on a Zeiss Ultra plus HR-SEM (Thornwood, NY).

#### 4.2.6 Mechanical characterization of BSA gels

A custom built microindenter (Shull Group, Northwestern University, IL) was used to measure the Young's modulus of BSA gels<sup>179,180</sup>. A flat-ended cylindrical stainless steel punch with a radius  $a = 0.44$  mm was used to indent the surface of the gel with a Burleigh inchworm motor (Rochester, NY) attached to a Sensotec 1 kg load cell (Columbus, OH) while the displacement was measured with a Philtec optical displacement sensor (Annapolis, MD). As the probe indented the sample at a fixed rate (10  $\mu\text{m/s}$ ), the load was recorded on a computer. The following relationship between the load and displacement in the linear regime of the curve:

$$\frac{P}{\delta} = \frac{8aE}{3f_c(a/h)}$$
Equation 4-1

This relationship can be used to convert the recorded loads into stresses for determination of the Young's modulus. The term,  $f_c$  is a geometric confinement factor determined by the ratio of the indenter radius to the gel thickness  $h$  which, in this work, is  $\sim 1$ . Rewriting Equation 4-1 yields an expression for the average stress  $\sigma_{\text{avg}}$  under the indenter:

$$\sigma_{\text{avg}} = \frac{P}{\pi a^2} = \frac{8E}{3\pi} \left( \frac{\delta}{a} \right) \frac{1}{f_c(a/h)}$$
Equation 4-2

The slope of the curve in the linear regime can be used to calculate the Young's modulus during the indentation. For low values of  $a/h$ , where  $f_c = 1$ , the quantity  $\delta/a$  functions as the effective strain. Mechanical indentations were performed in 6 different locations per sample at a rate of 10

μm/s. The Young's modulus of the gels were obtained by a linear regression of the stress vs strain plots and analyzed for statistical significance with a two-tailed t-test.

#### 4.2.7 In vivo subcutaneous Rat model

Eight female Sprague-Dawley rats (Harlan Laboratories, Inc.) weighing 150-175g were used for *in vivo* biocompatibility testing of the BSA gels. Four rats were randomly assigned into two groups for explant time points at 4 days and 4 weeks for evaluation of the acute and chronic inflammatory response. Animals were anesthetized using the inhalant machine Impact 6 (Vetequip Inc., Pleasanton, CA). Isofluorane was administered at a concentration of 2% with an oxygen flow rate of 2 L/min. Following anesthesia; the backs of the animals were shaved and then disinfected with butadiene followed by alcohol and a second butadiene wipe. Two incisions of approximately 1.5 cm in length were made at the implantation sites and subcutaneous pockets were created by blunt dissection in each location. In one location, an acid leached 20 wt% PBSA gel disk was implanted into the subcutaneous pocket far from the incision site. At the other incision site, a 20 wt% TBSA gel disk was implanted. A control saline injection and pH 7.4 (20 wt%) BSA solution was injected into the back of the rat in the two remaining implantation sites. Each disk or injection had a volume of 0.5mL. In all, each rat received all four treatments (PBSA, TBSA, BSA solution, saline) in four different rotating locations (anterior right, anterior left, posterior right, posterior left) for both time points (4 day and 4 week). The wounds were closed with surgical staples and implants were subsequently removed after 4 days. At the 4 day and 4 week time point, four animals were anesthetized and subsequently euthanized via CO<sub>2</sub> asphyxiation. Cervical dislocation was performed as a secondary euthanasia method and the

explants were harvested. The explants, which included the tissues surrounding the implanted material, were snap-frozen in a dry ice/acetone mixture. Explants were stored at -80°C until sectioning and H&E staining. Stained sections were photographed in series and in adjacent regions along the dorsoventral axis from the interior of the implant to the skin surface. *The Institutional Review Board and the Office for the Protection of Research Subjects at Northwestern University approved all the protocols used to collect donated human blood samples for in vitro hemocompatibility experiments. The Northwestern University Animal Care and Use Committee approved all animal procedures used in this thesis.*

#### **4.2.8 Histology and evaluation of the subcutaneous implants**

Frozen explants were embedded in optimum cutting temperature (TissueTek® OCT) compound (VWR, West Chester, PA) and subsequently cryosectioned into 6-10 µm sections (Microtome Cryostat HM525, Microm International, Walldorf, Germany). Sections were kept at -20°C and then stained with haematoxylin and eosin (H&E) for histological analysis. Stained samples were examined under a light microscope (Nikon Eclipse TE2000-U) and images were captured using Image Pro 5.0 software (MediaCybernetics, Bethesda, MD). Adjacent regions of the microscopic field were digitally matched, arranged, and color/luminosity corrected (for uniformity across the regions) with Photoshop Elements 6 (Adobe Systems Inc., CA) and ImageJ 1.43r (NIH, USA) to generate composite images. ImageJ was used with a 2D/3D photo stitching plugin written by Stephan Preibisch.

## 4.3 Results

### 4.3.1 HCl-BSA titration curve

The dropwise addition of 2M HCl to concentrated BSA solutions (~20 wt%) resulted in transient changes in turbidity of the solution during mixing. Throughout the titrations, BSA solutions were constantly stirred with a stir bar at 200-300 RPM. Immediately after addition of an acid drop, the turbidity of the solution rose sharply, but then dropped a few seconds later upon further mixing. During the period of increased turbidity, thin (<1 mm) translucent strands of material could be seen spinning in solution that disappeared after continued mixing. Drops were added in 25  $\mu$ l increments to establish a concentrated BSA solution titration curve (Fig. 4.1).

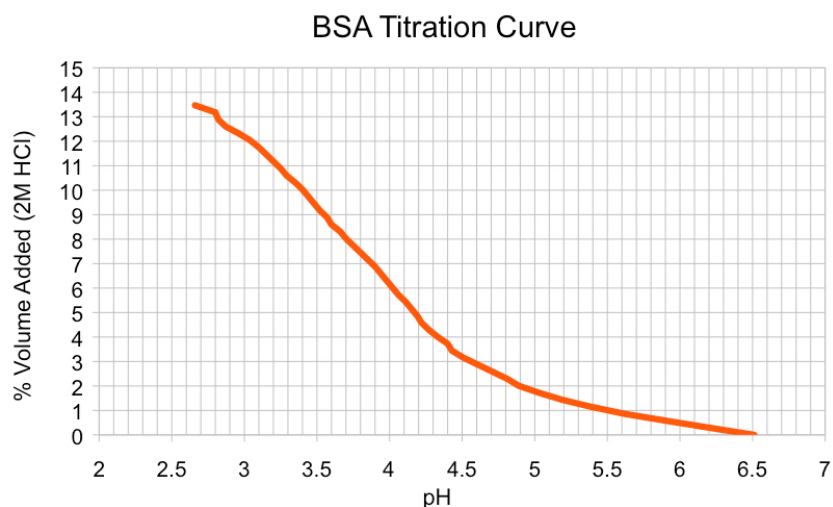


**Figure 4.1 Constant 20 wt% BSA solution titration curve.**

The concentration of the BSA solution in the titration curve was recalculated to correspond to a constant 20 wt% fraction of BSA in DI H<sub>2</sub>O. For example, to make a 20 wt% BSA precursor solution with a final of pH 3.5, Figure 4.1 indicates that 9% of the final solution volume desired

will come from the 2M HCl diluent. Increasing the molar concentration of the acid to reduce the volume of diluent is entirely possible but is not recommended. The immediate total denaturation and aggregation of albumin that comes in contact with a >2M HCl drop dissolves very slowly and greatly extends the time required to prepare the precursor solution. The effect of decreasing the volume delivered to avoid large aggregates is to approach a constant rate of acid delivery per molecule of albumin in solution. These results assist in the fabrication of future PBSA hydrogel synthesis by allowing us to calculate the volume needed for BSA precursor solutions. Care must be taken to avoid excess HCl that requires the addition of any NaOH. Base correction generates NaCl salt, which increases the ionic strength of the solution and can significantly alter the properties of the resulting hydrogel (See section 4.3.4.1).

Below pH 3.2, the increasing BSA solution viscosity began to interfere with the degree of solution homogeneity from poor mixing. The speed of the stir bar was raised to 600 RPM at pH 3.2, and raised to 800RPM at pH 3.04. This titration curve was used for fabrication of subsequent 20 wt% PBSA gels by adjusting initial concentrations of BSA in solutions by the expected amount of added 2M HCl from the curve.

### **4.3.2 Fabrication of albumin hydrogels by electrostatically triggered self-assembly**

Albumin dissolved in de-ionized water formed a clear yellow solution due to residual binding of albumin to bilirubin and other molecules (See section 2.7). There exists a critical minimum concentration of BSA required for the formation of BSA gels of approximately 15 wt%. This critical concentration was demonstrated by placing pH 3.5 BSA precursor solutions in glass vials that have been tilted to one side (Fig. 4.2). A layer of VWR pump oil (2 mL) was

deposited over the liquid BSA solutions prior to submersion in a water bath at 37°C to minimize evaporation of water which would effectively increase the initial concentration of BSA by an unknown amount. All BSA solutions were derived from the same pH 3.5 BSA precursor solution described in the methods. Concentrations of solutions were calculated from the initial BSA concentration (20 wt%), volume of added 2M HCl, and diluent DI H<sub>2</sub>O. When placed vertically, the angle of the tilt is preserved in the surface angle of the solutions that solidified into a PBSA hydrogel. Highly viscous BSA solutions that did not solidify reverted to a horizontal interface.

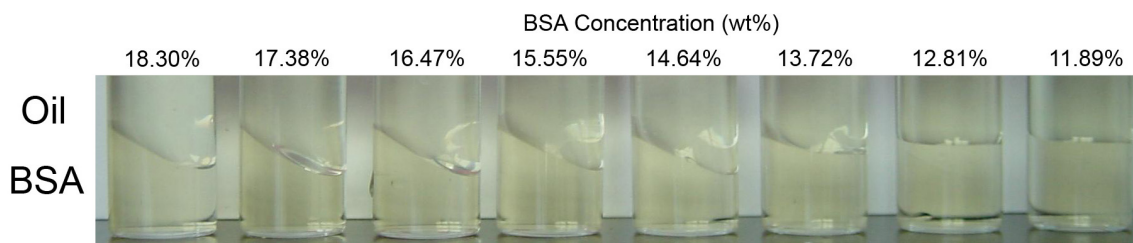


**Figure 4.2 PBSA Gelation at varying concentrations of BSA in solution.**

This result indicates the presence of a critical concentration at ~15 wt% identifiable by the observation of solid BSA gels >15 wt% and viscous BSA solutions <15 wt%. Solidification of the gels was evaluated every 5 minutes. The gel at 18.30 wt% formed in 28 minutes after submersion in the water bath. BSA solutions with concentrations above the critical concentration have been observed to form PBSA gels at room temperature after 2 days (Fig. 4.3, left). Since the thermal denaturation of BSA at pH 3.5 is known to occur at 46.8°C<sup>123</sup>, the effect of the water bath set at 37°C serves only to accelerate the time to gelation rather than affect the primary mechanism of gel formation. BSA precursor solutions at pH 7.4 do not exhibit any gelation behavior unless the temperature rises above 62°C to achieve thermal denaturation of the N-form.

Placing precursor solutions in thin 2 mm glass cylinder molds prior to gelation allowed accelerated equilibration with the water bath and resulted in PBSA gelation at 10 minutes (Fig. 4.3, center) and TBSA gelation at 1 min (Fig. 4.3, right).

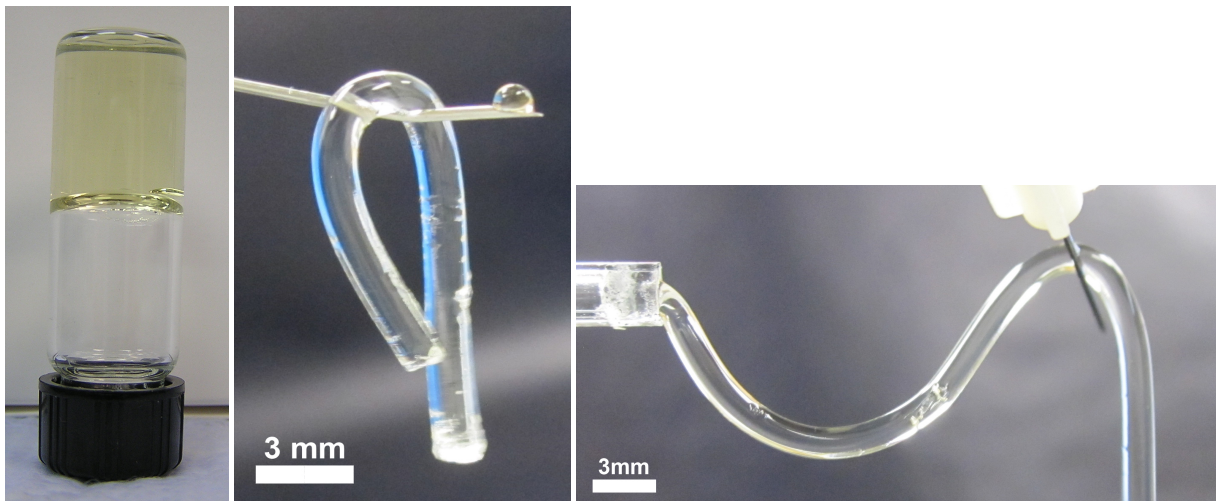


**Figure 4.3** Inverted vial depicts 20 wt% PBSA formed at 25°C. Center image depicts PBSA cylinder made in mold at 37°C. Right image depicts TBSA cylinder made in mold at 80°C.

#### 4.3.3 PBSA and TBSA nanostructure observation via electron microscopy

Transmission and scanning electron microscopy techniques were employed to observe the structures formed by BSA gel networks. TEM imaging of dilute (0.05wt%) acidic BSA solutions was performed using 2% uranyl acetate to negatively stain the proteins. At pH 2.18, the TEM images show a network of sharply stained white fibers connected together while pH 3.94 shows a more diffuse staining (Fig. 4.4). The white fibers at pH 2.18 had an average thickness of  $13.07 \pm 3.73\text{nm}$ , which is approximately the thickness of 3-5 expanded albumin proteins placed side by side. The pH 3.94 solution had an average ‘fiber’ thickness of  $54.47 \pm 12.15\text{nm}$  ( $\sim 13$  partially denatured albumin proteins) measured between adjacent dark spots on the image. While the TEM provides great spatial resolution, the limitation on the types of samples (dilute

concentration or very thin sections) that can be imaged limits the ability to easily observe the 3D structure of the PBSA.

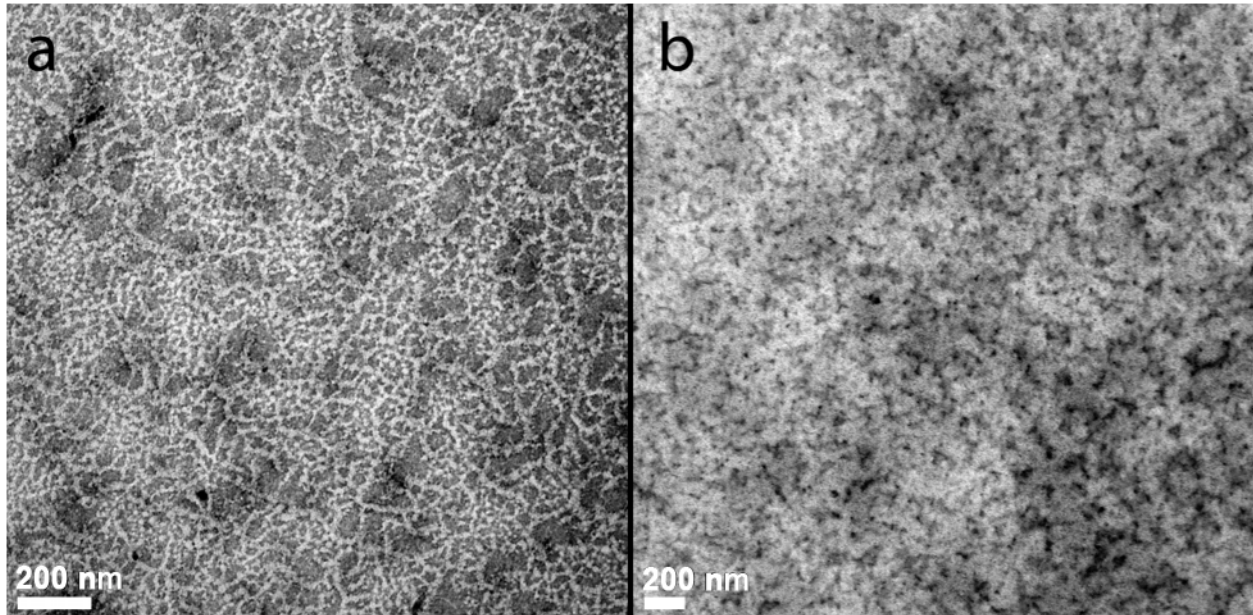


**Figure 4.4** TEM image of 0.05wt% BSA solutions at pH 2.18 (a) and pH 3.94 (b) stained with uranyl acetate.

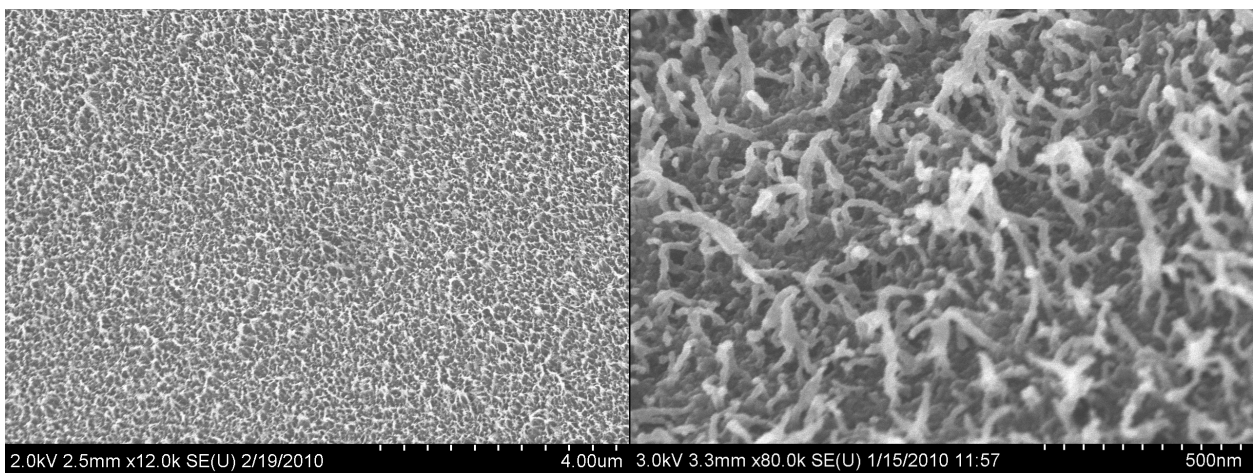


**Figure 4.5** SEM images of freeze dried and fractured PBSA hydrogels formed by electrostatic triggering method at pH 3.5 at 37°C

Imaging by SEM provided additional information about the 3D structure of the hydrogel. Figure 4.5 depicts a fracture surface of a freeze-dried PBSA hydrogel. Once again, fibers formed by protein can be seen with an average thickness of  $29.73 \pm 6.95\text{nm}$ , equivalent to approximately 6-9 expanded albumin proteins.

A new technique has recently become available which enables the preservation of the hydrated state for SEM imaging and involves vitrification of the gel sample prior to imaging in a Cryo-SEM system. The vitrification of the gel at a sufficiently fast rate ( $100,000^\circ\text{C/s}$ ) resulted in an amorphous water phase that appeared uniformly grey in the SEM. Vitrified gels were then freeze fractured to expose clean surfaces to the SEM and could also be plasma-etched to expose deeper layers of the sample.

While the PBSA and TBSA hydrogels appeared identical at the macroscale (Fig. 4.3), Cryo-SEM imaging revealed stark differences between the two hydrogels. TBSA and PBSA gels were imaged after freeze-fracture and a 30 second etching procedure. Surfaces of 20 wt% PBSA and TBSA hydrogels depict what is most likely amorphous water in grey and thin white strands of albumin in a network structure (Fig. 4.4). The images show PBSA hydrogels to have a more compact structure with small pores while TBSA hydrogels display an expanded structure with larger pores.

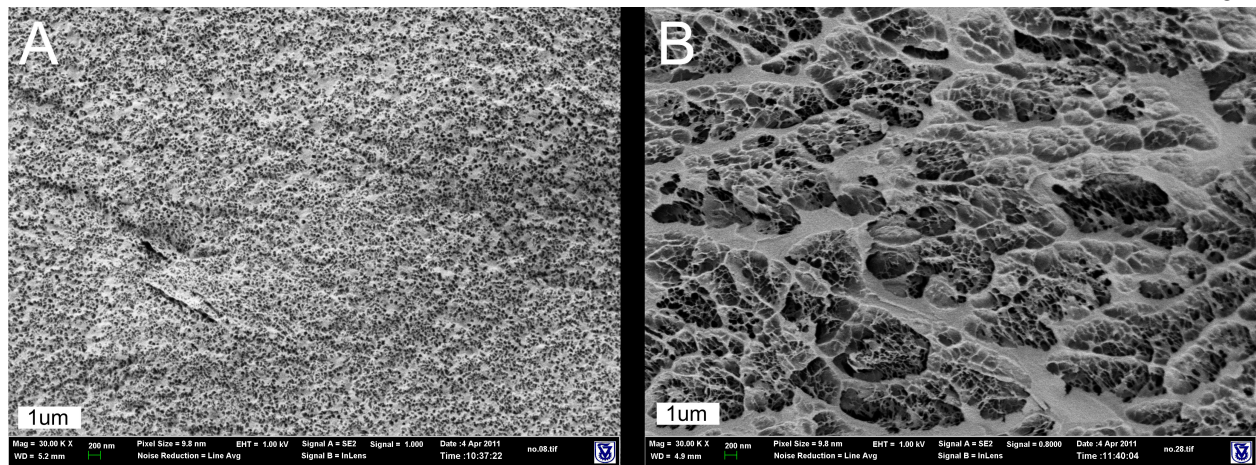


**Figure 4.6 Cryo-SEM images of freeze-fractured hydrogels formed by electrostatic triggering method at pH 3.5 at 37°C (A) or by thermal denaturation at 80°C method (B).**

#### 4.3.4 Elastic modulus measurement by mechanical indentation

The Young's modulus was measured with a custom mechanical indentation system and performed under a protective layer of Oil Red O dyed oil so that the boundary between the gel surface and oil layer could be observed. Representative indentation plots are reproduced in Figure 4.7. As the indenter moves toward the surface of the gel, no stress is recorded (Fig. 4.7, stage 1). Upon impact, the regime where the stress increases linearly with increasing strain (Fig. 4.7, stage 2) is defined as the elastic deformation. The slope of this line is known as the Young's modulus. Further increase in strain resulted in fracture of the PBSA hydrogel at 55 kPa as indicated by the drop in recorded stress. As the indenter continues to push into the PBSA hydrogel, it meets additional resistance from unfractured hydrogel regions that continually fracture until the indenter is pulled out (Fig. 4.7, stage 3). In the final stages, the indenter was pulled out of the hydrogel and retracted back to its original position (Fig. 4.7, stage 4-6). In stage 5, the indenter experienced a negative stress of -25 kPa, representing the suction of the hydrogel

on the indenter as it is removed. The TBSA test, performed in the same manner, exhibited a steeper Young's modulus slope and a significantly higher recorded maximal stress (250 kPa) with reduced suction (-5 kPa).

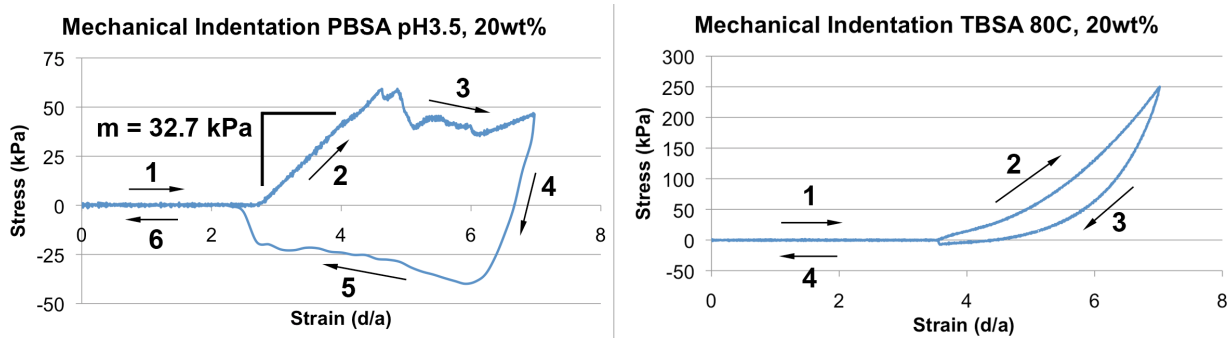


**Figure 4.7 Representative mechanical indentation plots for PBSA and TBSA hydrogels. The slope of the linear elastic regime is equal to the Young's modulus. Arrow directions indicate progression of indenter throughout the test.**

From these indentation plots, the Young's modulus was extracted for comparison between initial hydrogel synthesis conditions. 17 wt% PBSA hydrogels were formed at intervals of pH 0.5 or smaller from pH 2 through pH 7.5 (Fig. 4.8A). The strongest PBSA hydrogels were formed in the F-form pH range between 3.0 and 4.0 with a maximal gel modulus of 34 kPa at pH 3.5. Above pH 4, the transition from the N-form albumin to the F-form albumin was incomplete and these solutions did not form solid gels. Below pH 3.0, BSA gel solutions became highly viscous but never formed a solid gel even after submersion in 37°C for 2 days. This was a surprising result because it has been reported in the literature that oligomerization can form tetramers of albumin con also form at pH 2<sup>181</sup>. However, these other studies were performed in concentrations below our 15 wt% critical gelation concentration and on much longer time scales, days as opposed to minutes. It is possible that our low pH solutions may also be forming albumin oligomers but that large degree of charge causes the aggregates to become repulsive to each other after a certain size preventing further aggregation and hydrogel formation.

As expected, the Young's modulus of both PBSA and TBSA hydrogels increased with increasing concentration (Fig. 4.8B). At each concentration however, PBSA hydrogels were weaker than the TBSA hydrogels. The maximal Young's modulus recorded in these experiments at 20 wt% PBSA and TBSA were 46 kPa and 67 kPa respectively. The concentration of PBSA hydrogels used for the remainder of this work in this thesis are 20 wt% unless otherwise indicated. For PBSA hydrogels, we have also identified a critical minimum concentration of ~15wt% albumin in the precursor solution required for gel formation.

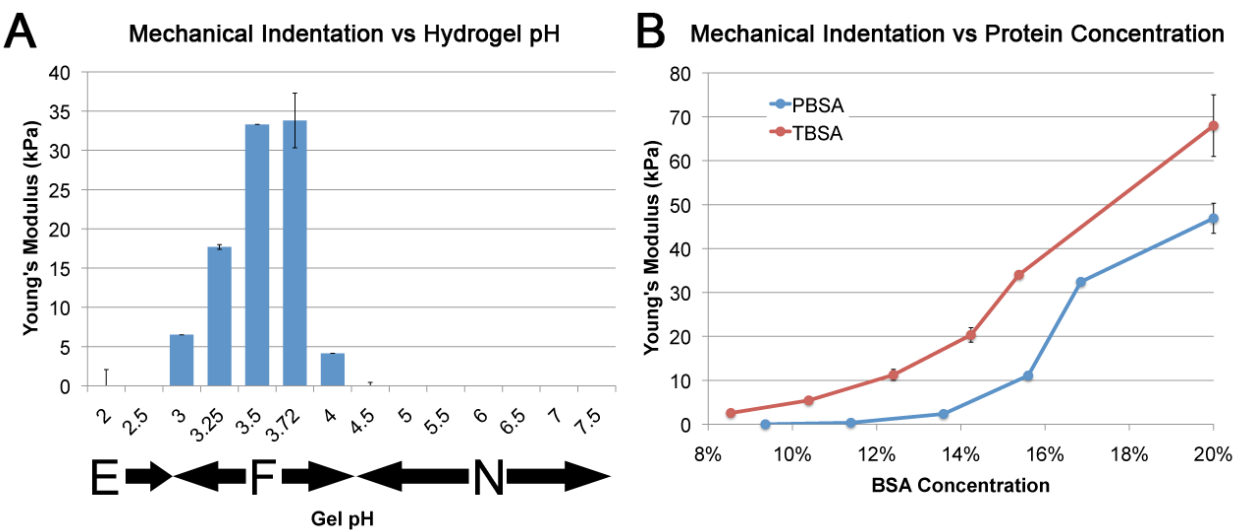


**Figure 4.8 Mechanical properties of BSA hydrogels demonstrating PBSA hydrogels are softer than TBSA hydrogels. A, Young's modulus of BSA solutions (17 wt% BSA) with different pH values ranging from 2-7 incubated at 37°C (n=4 for each pH value). B, Young's modulus of PBSA (pH 3.5 incubated at 37°C, n=4) and TBSA (pH 7.4 incubated at 80°C, n=8) hydrogels with increasing BSA concentration measured by mechanical indentation. Error bars in A and B represent the standard deviation of the data set. BSA isoforms (E, F, N) are mapped below the plot according to their pH transition values.**

#### 4.3.4.1 Effect of ionic strength on Young's modulus

Several groups have shown a positive correlation between ionic strength and the propensity of a protein to aggregate<sup>111,112,123,125,128,182</sup>. When the ionic strength of the BSA precursor solution is increased to 1 mM NaCl, the electrostatic repulsions between the proteins

are screened out. At the macroscale, this effect leads to the formation of higher Young's modulus as shown in mechanical indentation tests on PBSA and TBSA hydrogels with and without added salt (Fig. 4.9). PBSA hydrogels formed in 1 mM NaCl had a Young's modulus of  $84.8 \pm 5.9$  kPa in comparison to PBSA hydrogels with no added salt with a Young's modulus of  $43.5 \pm 3.8$  kPa. Similarly TBSA hydrogels demonstrated a similar increase in Young's modulus with the addition of salt ( $321 \pm 14$  kPa and  $116 \pm 2.5$  kPa).

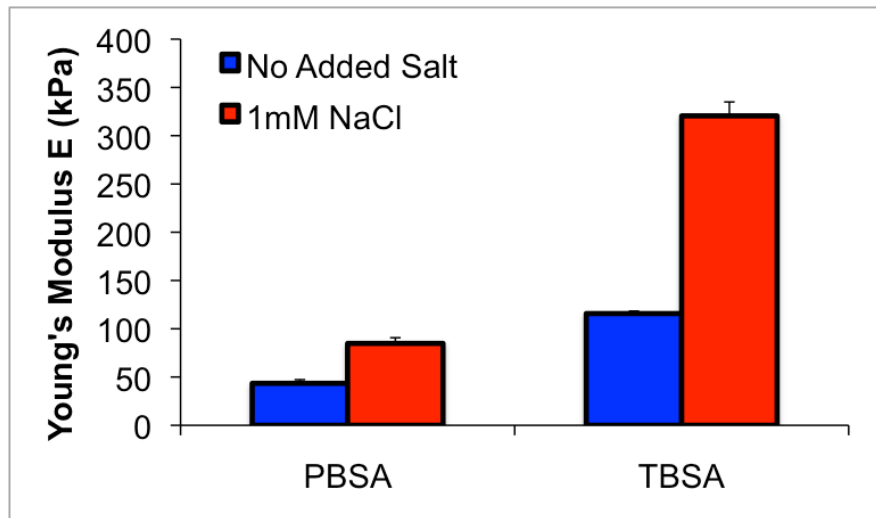
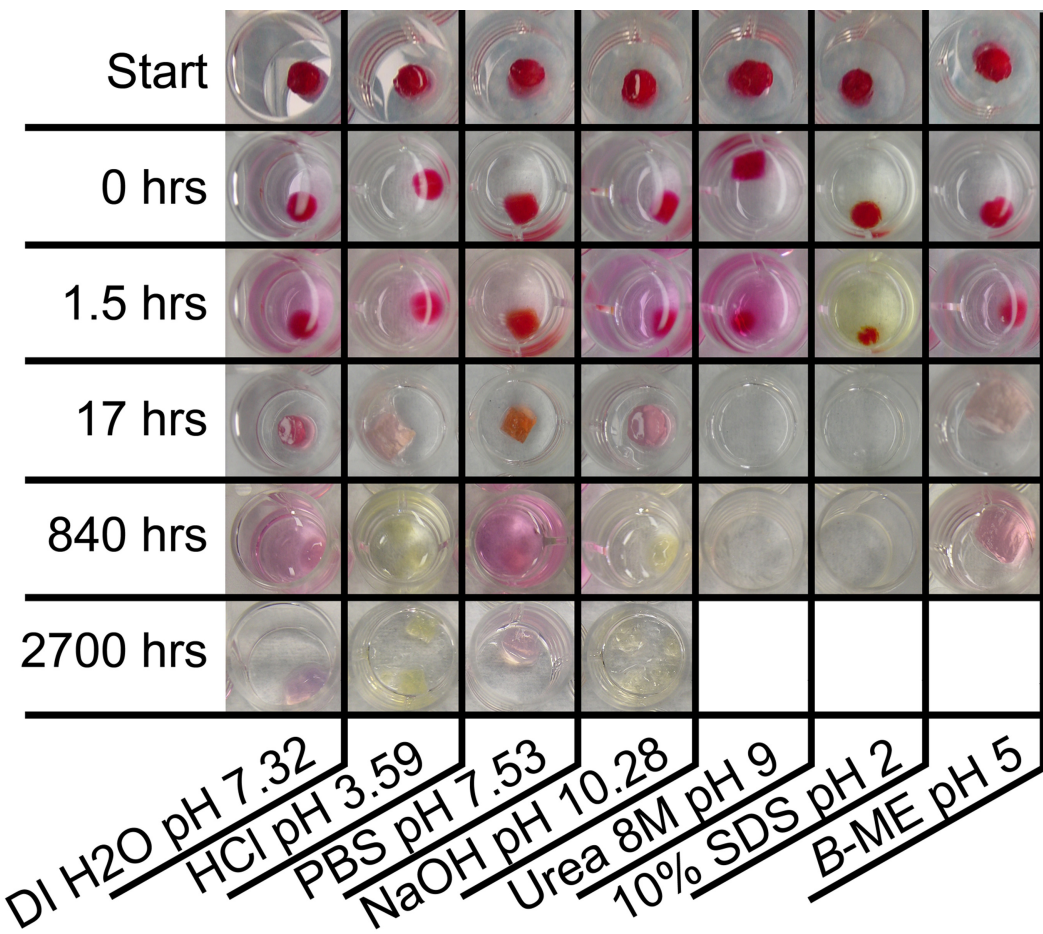


Figure 4.9 Effect of 1 mM added salt to BSA precursor solution on PBSA and TBSA Young's modulus. (n=4)

#### 4.3.5 PBSA acid neutralization and the effect of chemical environment on hydrogel integrity

To assess the nature of the interactions within the gel network, 20 wt% PBSA gel samples (pH 3.5) were incubated in different chemical environments (Fig. 4.10). Stability of PBSA hydrogels in water enabled neutralization of acid required during hydrogel formation. Phenol red added to neutralizing PBS buffer colored the PBSA hydrogels red over three days and served as a visual marker for bulk hydrogel pH. Images at 0hrs, 1.5hrs, and at 840hrs (1 month)

were taken with solvent in the wells to demonstrate the leaching of phenol red dye from the gel. Images at the 0hrs, 17hrs, and 2700hrs (3 months) are shown without the solvent to show the degradation of the gel. PBSA hydrogels were stable for up to three months in deionized H<sub>2</sub>O (pH 7.32), HCl-H<sub>2</sub>O (pH 3.59), NaOH-H<sub>2</sub>O (pH 10.28), and in PBS (pH 7.53) indicating a resistance to degradation by acidic or basic conditions. PBSA gels submerged in 8M urea or 10% SDS were completely degraded within 17 hours indicating that a primary mechanism of PBSA hydrogel formation is non-covalent and probably driven by hydrophobic interactions. Due to complete dissolution of the PBSA gels, the 8M urea and 10% SDS samples were not photographed beyond 840 hours. Reduction of intermolecular disulphide bonds by  $\beta$ -Mercaptoethanol ( $\beta$ -ME) solvent resulted in hydrogel swelling.



**Figure 4.10 Effect of various chemical environments on PBSA hydrogel integrity.** Small cylindrical PBSA hydrogels (0.5 cm diameter), acid leached in DMEM for 3 days until the pH returned to neutral pH, were placed in different solutions and photographed over the course of three months. These images are representative of the larger sample set ( $n=4$ ) and demonstrate hydrogel degradation resistance to acid, base, and salt conditions. Urea and 10% SDS degrade the gels within 17 hrs while disulphide bond reduction by  $\beta$ -ME results in hydrogel swelling.

#### 4.3.6 In vivo biocompatibility evaluation

To evaluate the acute (4 day,  $n=4$ ) and chronic (4 week,  $n=4$ ) inflammatory potential of the BSA hydrogels *in vivo*, TBSA and acid-leached PBSA gel disks were implanted subcutaneously. After removal of surgical staples day 4; all wounds had healed showing some residual scab formation. Both TBSA and PBSA implants still left visible bumps at the

implantation site while the BSA solution and PBS injection left none. Gross observation of the explants at 4 days and 4 weeks showed that the tissue had grown around the implants. H&E staining of the sections revealed stark differences between the degradation patterns of the PBSA and the TBSA implants *in vivo* (Fig. 4.11). Cells infiltrating the PBSA hydrogels were seen at both time points, and correlated with significant gel degradation (Fig. 4.11A and E). The PBSA hydrogels were noticeably more degraded at 4 weeks than at 4 days although both displayed complete degraded channels traversing the entire length of the implant. In contrast, TBSA hydrogels showed no sign of degradation and were intact at both time points (Fig. 4.11B and F). A fibrous capsule surrounding the TBSA hydrogels became denser and thicker at 4 weeks relative to 4 days. Control 20 wt% BSA solutions (pH 7.4) injected into subcutaneous pockets resulted in an increased general inflammatory response judged by relative increase in number of cells in the subcutaneous pocket (Fig. 4.11C) at 4 days when compared to the saline control injection (Fig. 4.11D). At 4 weeks, the inflammatory response of the BSA injection has decreased significantly (Fig. 4.11G) and was closer to the saline control (Fig. 4.11H).

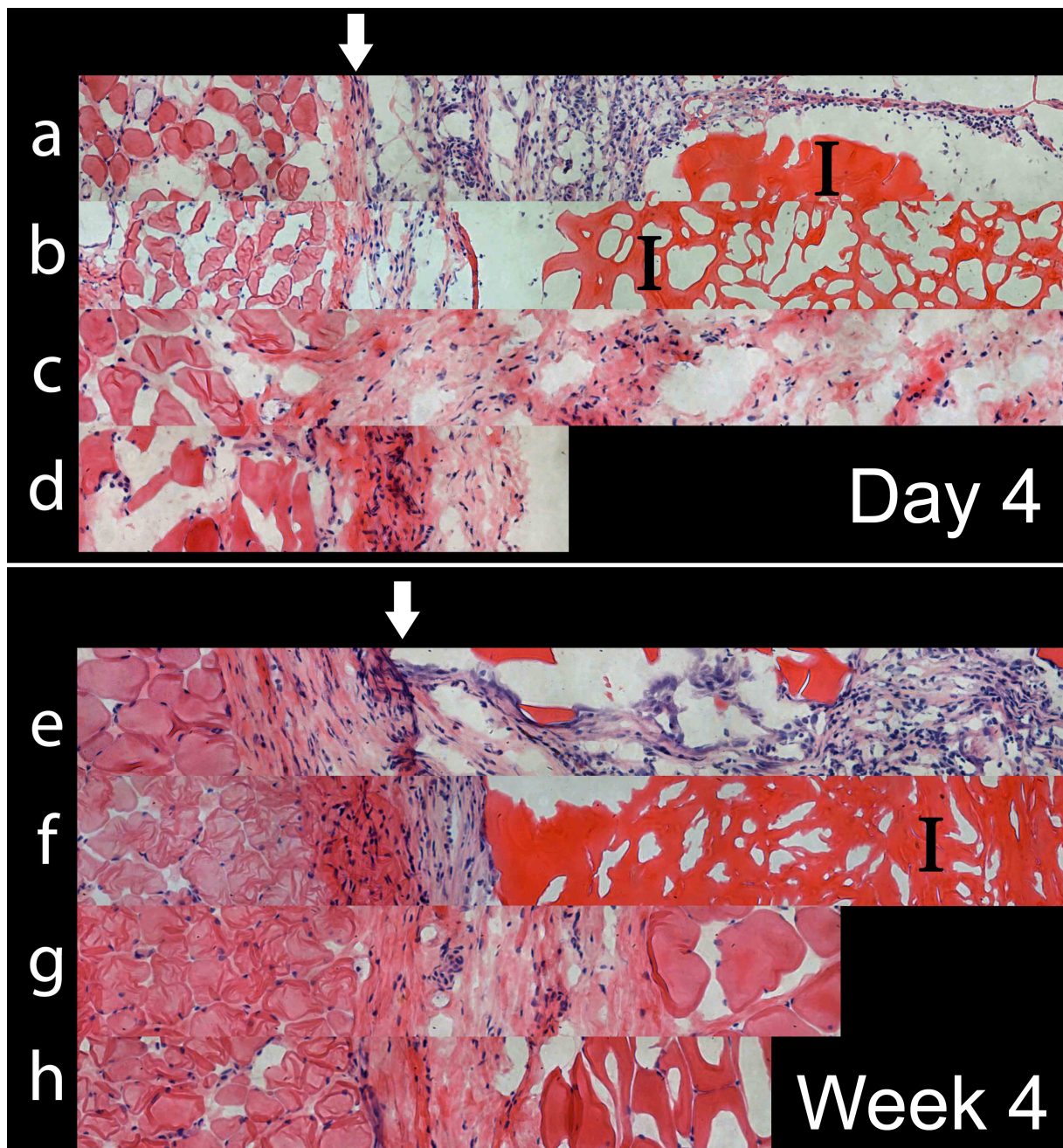


Figure 4.11 Biological response to subcutaneously implanted PBSA and TBSA hydrogels. Tissues with implanted PBSA gel disks (a, e), TBSA gel disks (b, f), pH 7.4 BSA solution injection (c, g), and saline control injections (d, h) at 4 days (a, b, c, d) and 4 weeks (e, f, g, h). Samples were stained with H&E, purple:nuclei; pink:cytoplasm; pink-red/I: implant gels. Histological images are aligned to each other at the original interface (white arrow) between the implant and the tissue lining the subcutaneous pocket. Images for each time point are from the same rat and are representative of the group population overall (n=4).

#### 4.4 Discussion

It is known that the denaturation temperatures of BSA vary as a function of the pH and ionic strength of the solution<sup>112</sup>. The PBSA gels described here were all formed at temperatures at or below 37°C, which, at a pH of 3.5 is below the peak of thermal denaturation ( $T_d=46.8^\circ\text{C}$ ) but still above the onset of thermal denaturation ( $T_i=28^\circ\text{C}$ )(Table 2.2). However, because of the lack of a distinctive peak at low pH values in DSC values (Appendix C), it is unclear whether BSA experiences any additional denaturation at 37°C apart from that already caused by the acidic environment. Previous studies by Alizadeh et al.<sup>183</sup> and Takeda et al.<sup>184</sup> investigated the effect of additional heating on the hydrophobicity and secondary structure content of albumin at low pH. At low pH 3, heating albumin to 80°C (above thermal denaturation temperature) causes no further changes to protein hydrophobicity (beyond the changes already induced by low pH) as determined by aromatic (1-anilinonaphthalene-8-sulfonic acid, ANS), aliphatic (cis-parinaric acid, CPA), and uncharged (6-propionyl-2-(dimethylamino)-naphthalene, PRODAN) fluorescent hydrophobicity probes<sup>183,185</sup>. In contrast, the alpha helix content of BSA at low pH 2.8 (alpha helix content at 25°C was 46%) that was heated to 65°C decreased significantly to 31% while heating to 37°C only decreased alpha helix content to 45% as measured by circular dichroism measurments<sup>184</sup>. These results suggest that the additional heat treatment of PBSA hydrogels at 37°C did not induce a significant loss in secondary structure content nor increase in hydrophobicity. Furthermore, PBSA gels could also form at 25°C in 2 days (Fig. 4.3), a temperature that is below  $T_i$ , which would imply that the gelation of PBSA is primarily pH-driven rather than temperature driven. Moderate thermal heating used in several experiments

may have accelerated the speed of the PBSA gelation, as evidenced by the 10-minute gelation at 37°C in a glass mold compared to the 2 day gelation at 25°C.

Veerman et al.<sup>123</sup> have published detailed phase diagrams on the formation of fibrillar BSA gels with varying concentrations (1.5 - 8 wt%), ionic strength (0.0003 – 0.35 M), heating times (1 – 40 hours), and pH (2 – 3.5) all in water baths at 60°C. Their findings indicate that increasing ionic strength allows the formation of hydrogels with decreased protein concentration. While all their studies required thermal denaturation at 60°C, an extension of this result would imply that increased ionic strength should enable the formation of stronger hydrogels. This expectation was confirmed in the mechanical indentation test of PBSA and TBSA hydrogels with low or high ionic strengths (Fig. 4.9). These results corroborated an apparent role of counter ions in solution that serve to neutralize highly charged albumin residues (Fig. 3.19).

The previously reported critical concentrations for TBSA hydrogels are 6 wt% while PBSA hydrogels form above a much higher critical concentration, around 15 wt%<sup>8,128</sup>. The difference in critical protein concentrations required to form PBSA or TBSA hydrogels suggests that the protein denaturation pathways that lead to gelation are substantially different. Others have shown that TBSA gelation is caused by a viscoelastic phase separation that locally increases the gel concentration that precedes the formation of percolating gel networks in TBSA<sup>186</sup>. This viscoelastic phase separation can be visualized by the large pores seen in the Cryo-SEM images for TBSA. In contrast, Cryo-SEM images show that PBSA hydrogels are more homogenous and do not exhibit this same phase separation (Fig. 4.6).

With increasing concentrations, the Young's Modulus of the gels increases as demonstrated with TBSA gels by Lefebvre et al.<sup>126</sup>. The maximal Young's modulus of the gels

was shown to occur at pH 3.5 with a decrease in modulus above this point closer to pI (Fig. 4.3). Below pH 3, BSA solutions became highly viscous (as described in Section 4.1) and did not gel properly. This effect could be explained by acidic hydrolysis of the BSA proteins resulting in shorter segments of albumin that cannot gel at 20 wt%.

Qualitative degradation studies of PBSA demonstrate the stability of the gel in solvents at different pH (3.59, 7.53, 10.28) and ionic strength (Fig. 4.10). Surprisingly, PBSA hydrogels were able to be acid leached to pH 7.4 without loss in hydrogel stability (Fig. 4.10, PBS). Fortunately, this ability greatly expands the clinical potential of PBSA hydrogels. An explanation for this ability comes from the SEM images (Fig. 4.5), which showed fiber formations that incorporated several F-form albumins in each bundle. These higher level structures allow the partially denatured proteins to become stabilized within the new quaternary structure. Degradation of the hydrogel would require dissolution of these constructs, which are now stabilized by the numerous interprotein hydrophobic attractions. In fact, dissolution of the gel was achieved by disrupting these hydrophobic interactions by 8M urea and 10% SDS (Fig. 4.10). The disruption of the hydrophobic and non-covalent interactions by 8M urea and 10% SDS demonstrate that these interactions are critically important for the maintenance of PBSA gel integrity. Acid leaching serves to remove excess acid that is no longer required since the partially denatured albumin was irreversibly locked into a new microstructure.

The observed swelling of the PBSA gels in the  $\beta$ -ME solvent suggests that the 17 disulphide bonds remain intact during the fabrication of the gel and are not involved in the intermolecular interactions between the proteins. In the Cryo-SEM images (Fig. 4.6), the structures appear very compact which corroborate the results of molecular dynamics simulations

for the F-form albumin conformation (Fig. 3.6)<sup>187</sup>. The observed swelling effect could be explained by increased protein flexibility and expansion due to reduced disulphide bonds that enable the gel to absorb more water. The swelling behavior of the PBSA gels could be exploited and used as a drug loading mechanism. Replacement of the  $\beta$ -ME solvent with DI H<sub>2</sub>O and drugs could diffuse into the larger pores while the gel slowly contracts and molecularly entrapping drugs within.

Biocompatibility of the PBSA and TBSA gels was observed in vivo by histological examination of rat tissues, which were implanted with PBSA and TBSA gels (Fig. 4.11). The difference in the in vivo degradation rate was surprising and likely attributed to differences in the mechanisms of hydrogel formation, which lead to the different gel structures. TBSA gels did not degrade and became encased in a fibrous capsule while the PBSA gels degraded rapidly and allowed the infiltration of cellular infiltrates deep inside the scaffold. It is also possible that the higher Young's modulus of the TBSA gels (Fig. 4.8) may have affected the cellular biodegradation process. It is well known that matrix stiffness plays an important role as a mediator of cellular behavior. Preferential migration of cells towards stiffer substrates on 2D substrates leads to proliferation and fibrogenesis<sup>188</sup>. Overall, the PBSA hydrogel was more conducive to cell infiltration than the TBSA hydrogel.

## 4.5 Conclusions

All-protein based hydrogels were fabricated from concentrated pure BSA solutions by employing a new method based on an acidic pH environment to partially denature albumin. PBSA gels exhibited properties that differ from those reported in the current literature and lend

credence to the hypothesis of an alternate gelation mechanism based primarily on intermolecular hydrophobic interactions rather than cross-linking mechanisms. PBSA hydrogels could be acid leached to pH 7.4 without loss in hydrogel stability due to new quaternary structural self-assembly. These structural elements lock the partially denature protein structures into larger self-assembled constructs that do not require the acid used to fabricate them. The critical concentration for gelation is approximately 15 wt% and the strongest gels are formed at pH 3.5 within 10 minutes. PBSA gels degrade faster *in vivo* than TBSA gels as shown in a subcutaneous rat model at both 4 days and 4 weeks.

## CHAPTER 5: FUNCTIONAL DOMAINS IN PROTEIN HYDROGELS

### 5.1 Objective

Albumin's capacity to bind a range of clinically relevant therapeutic molecules has been well documented for the N-form albumin<sup>28-33,189</sup>. Several approaches have been explored to exploit albumin as a drug depot to extend a therapeutic molecule's half-life, including non-covalent binding, covalent attachment, and genetic fusion<sup>29</sup>. However, the majority of these studies focus entirely on the drug interactions with N-form albumin.

A thorough literature search using the search terms, "albumin, protein, partial denaturation, unfolded, acid, drug, binding, and affinity" with combinations thereof discovered only a single publication that discussed the drug binding affinity to pH-induced partially denatured albumin by Ahmad et al.<sup>190</sup>. In their work, circular dichroism and fluorescence measurements were used to quantify the binding affinity of Ciprofloxacin to acetic acid denatured albumin at pH 3.5<sup>190</sup>. There was one additional related study that investigated the binding of three fluorescent probes (with resemblance to therapeutics that bind to region IIA) after denaturation by guanidine hydrochloride (GdnHCl)<sup>191</sup>. Albumin denaturation by GdnHCl has been studied by SAXS and shown to have a similar denaturation pathway as the low pH transitions<sup>152</sup>. However, the inverse sequence (i.e., binding drug first and then testing resistance to denaturation) has been studied extensively for many different compounds<sup>94,192-197</sup>. These studies report increased stabilization and higher denaturation temperatures after binding with

their respective molecules. The earliest report of albumin stabilization by binding is to the well-known long-chain fatty acid binding sites<sup>42,198</sup>. In fact, two main commercially available formulations of albumin are provided either fatty or fatty acid free due to this difference in protein stability.

Although many studies exist that investigate the effect of binding on denaturation, our work described in Chapter 5 may be one of very few that investigate the effect of denaturation on binding affinity. The anticancer therapeutic atRA has a well-characterized binding affinity for albumin in a domain that is protected during the N-F transition<sup>75</sup>. **Our objective in Chapter 5 is to determine whether F-form albumin has any binding affinity for the therapeutic molecule atRA and determine whether the bound drug retains its bioactivity.** Based on the large collection of data demonstrating drug affinity under denaturating conditions and the presence of substantial secondary structural content in partially denatured albumin, we hypothesize that there will be some residual binding affinity for atRA. In this chapter, we also explore the effect of the drug interactions on the stability of the hydrogel network. Studies have shown that LCFA bound albumin has increased resistance to denaturation in solution<sup>35</sup>. In Chapter 4, we observed the dissolution of the PBSA hydrogels (using pH sensitistive defatted albumin) when exposed to urea and SDS. The inclusion of a hydrophobic drug like atRA may provide a same stabilizing effect on the hydrogel as LCFA does in the single protein case. Stabilization to degradation upon drug binding may confer additional properties beneficial to drug delivery systems such as tunable degradation kinetics or multimodal drug release mechanisms (first by short-term diffusion of unbound drug, second by long-term degradation of the hydrogel network).

## 5.2 Experimental section

### 5.2.1 Molecular dynamics simulations

The structure of partially denatured BSA was obtained from previous work described in Chapter 3<sup>187</sup>. After randomly adding 10 molecules of atRA to the system, molecular dynamics simulations were performed using the GROMACS simulation package at constant temperature (300 K) and pressure (1 atm)<sup>158-161</sup>. The OPLS/AA force field was used to simulate the atomistic BSA model (9336 atoms) solvated with ~94,000 SPC water molecules, 100 counterions, and 10 atRA molecules<sup>158,162</sup>. The atRA-BSA models were equilibrated by a steepest descent algorithm followed by a 100ns NVT production run with periodic boundary conditions.

### 5.2.2 Potential of mean force calculation

The potential of mean force was calculated from a series of umbrella sampling<sup>199</sup> simulations ( $n=30$ ) where configurations of bound atRA molecules were placed at linearly increasing distances ( $\Delta z = 0.5 \text{ \AA}$ ) from their self-selected preferred binding pocket after 100 ns of unconstrained molecular dynamics. The center of mass of the atRA molecule and the center of mass of neighboring binding pocket residues were used as the anchor points to determine the separation distance  $z$  between the BSA binding site and atRA. The potential of mean force was then calculated on the output of the 30 simulations after 5 ns using the a weighted histogram analysis method (g\_wham) embedded in the GROMACS software<sup>200</sup>. The number of configurations and separation distances were selected such that the entire phase space was sufficiently sampled until  $z$  is at least 2 nm from the binding site where  $z = 0$  is the preferred binding distance after 100 ns.

### 5.2.3 atRA binding and release

atRA (R2625, Sigma, St. Louis, MO) was added to solutions of BSA with molar ratio concentrations ranging from 0 to 2:1 (atRA:BSA). atRA binding to BSA was assessed by measuring the fluorescence intensity on BSA at 340 nm with excitation at 295 nm as reported in the literature<sup>75</sup> using the plate reader Tecan Safire II (Tecan, Maennedorf, Switzerland). A molar ratio concentration of 8:1 (atRA:BSA) was used when incorporating atRA into BSA precursor solutions before gelation. Precursor solutions were processed as normal to fabricate atRA-loaded PBSA and TBSA hydrogel disks that were cut into cylinders with a .75 cm cylindrical punch. Disks were submerged in 10 mL PBS at 37°C for atRA release studies. Eluates were collected and replaced at each time point and fluorescence intensity of atRA at 340 nm and BSA at 280 nm was collected with a NanoDrop™ 2000C Spectrophotometer (ThermoScientific™, Waltham, MA).

### 5.2.4 Scratch test migration assay

Human aortic smooth muscle cells (HASMC) (Lonza, Basel, Switzerland) (passage 5) were cultured in SmGM-2 media. All cells were cultured at 37°C in a humidified incubator containing 5% CO<sub>2</sub>. HASMCs (seeding density  $1 \times 10^4$  cells/cm<sup>2</sup>) were seeded onto TCP surfaces and grown until 90% confluent. Cell culture media was changed every 2 days until confluence after which serum-free SmGM-2 media was used to create a nutrient starved environment for 24 hrs. A vertical scratch was made with a sterile 200 uL pipette tip in the confluent HASMC layer, rinsed with warm PBS, and replaced with 1 mL SmGM-2 media. The

underside of the dish was marked near the wound area to aid in identification. Wells were randomly placed into 4 groups which received either a 100 uL dose of eluted material from atRA loaded PBSA or TBSA release study at day 10, a 100 uL dose of 24 ng atRA dissolved in PBS, or a control 100 uL of PBS. A light microscope (Nikon Eclipse TE2000-U) was used to capture images using Image Pro 5.0 software (MediaCybernetics, Bethesda, MD) of the wound area immediately at day 0 and at various times until the control wound closed at 24 hrs. Wound areas were determined using an automated wound area measurement macro with the ImageJ 1.43r software (NIH, Bethesda, MD). The measurement of migration was determined by subtracting the cell-free area at day 0 from the cell-free area at 24 hrs. Data were presented as means ± SD of several independent experiments from each atRA-loaded hydrogel replicate.

#### 5.2.4.1 Data Analysis

Data analysis was performed using Microsoft® Excel software. Data from independent experiments were quantified and analyzed for each variable. Comparisons between multiple treatments were made with a students t-test. A p-value of <0.05 was considered to be statistically significant.

### 5.2.5 Hydrogel degradation after atRA loading

PBSA and TBSA hydrogel disks that were loaded with 8:1 molar ratio of atRA:albumin from previous release studies were exposed to urea and SDS at the conclusion of the release study. By this timepoint, both PBSA and TBSA hydrogel disks have been releasing atRA into PBS for 14 days. The hydrogel disks were exposed to 6M urea for 48 hrs, followed by exposure

to 10% SDS for 2 months, followed by 8M urea for 1 month. Photographs were taken over the three month period to document the extent of PBSA and TBSA gel degradation.

## 5.3 Results

### 5.3.1 atRA binds to both F-form albumin and N-form albumin

Tryptophan fluorescence at 340 nm changes upon atRA binding to BSA (Fig. 5). One of the two tryptophans in BSA (TRP 213) is located deep within the globin fold in domain II and fluorescence signal from this tryptophan is reduced when bound to atRA (Fig. 5.1A). Without added atRA, N-form albumin exhibits higher initial fluorescence intensity over F-form albumin (Fig. 5.1B). Upon addition of atRA, the tryptophan fluorescence signal at 340 nm is rapidly quenched for both N-form albumin and F-form albumin. As a fraction of the initial fluorescence signal, N-form albumin exhibits greater fluorescence quenching than F-form albumin (Fig. 5.1D) that may be due to the altered conformation state of F-form albumin and shifting atRA binding sites to other locations not dominated by the TRP 213 residue. Fluorescence quenching continues to increase as the system reaches equilibrium, increasing significantly within the first 2 hours and then more slowly over the next 24 hours (Fig. 5.2). PBSA and TBSA hydrogels loaded with atRA demonstrate a small initial burst release of atRA followed by linear release over 10 days in PBS at 37°C (Fig. 5.1C).

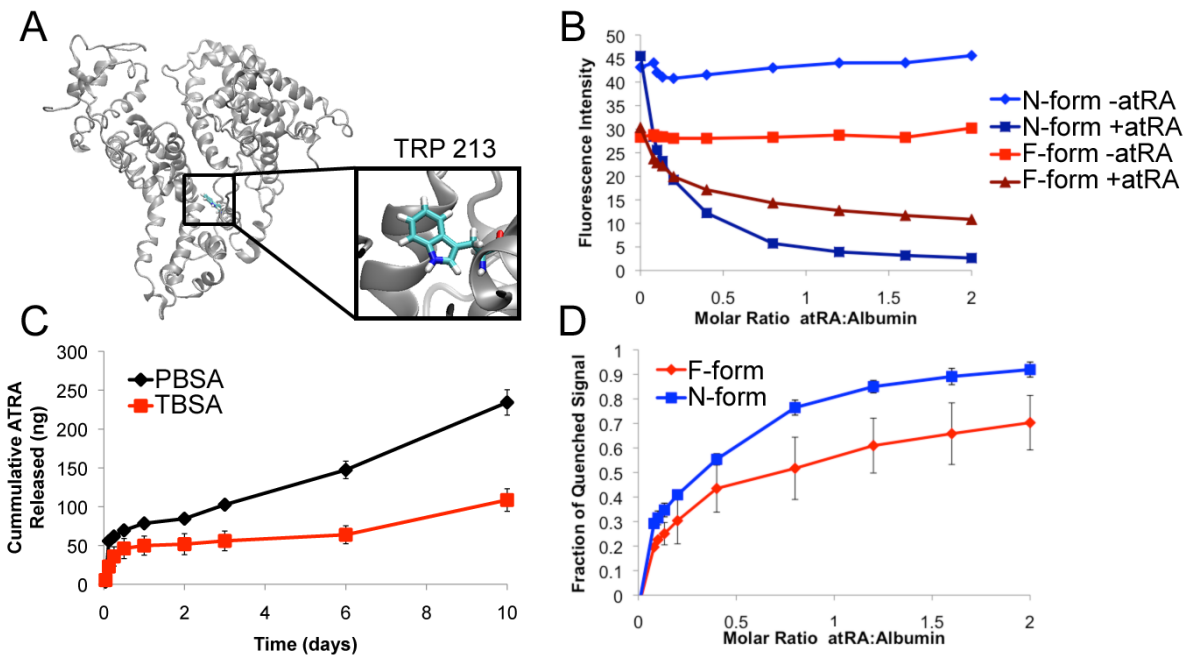


**Figure 5.1** atRA binding to N-form albumin and F-form albumin measured via fluorescence quenching of tryptophan residue TRP 213 at 340 nm (a). Fluorescence intensity for N-form BSA and F-form BSA is consistent before addition of atRA (b). Addition of increasing molar concentration of atRA quenches both N-form albumin and F-form albumin fluorescence intensity. d, A greater fraction of initial fluorescence is quenched in N-form albumin than in F-form albumin indicating altered binding affinity. c, Release of atRA into PBS at 37°C from F-form albumin and TBSA hydrogels.

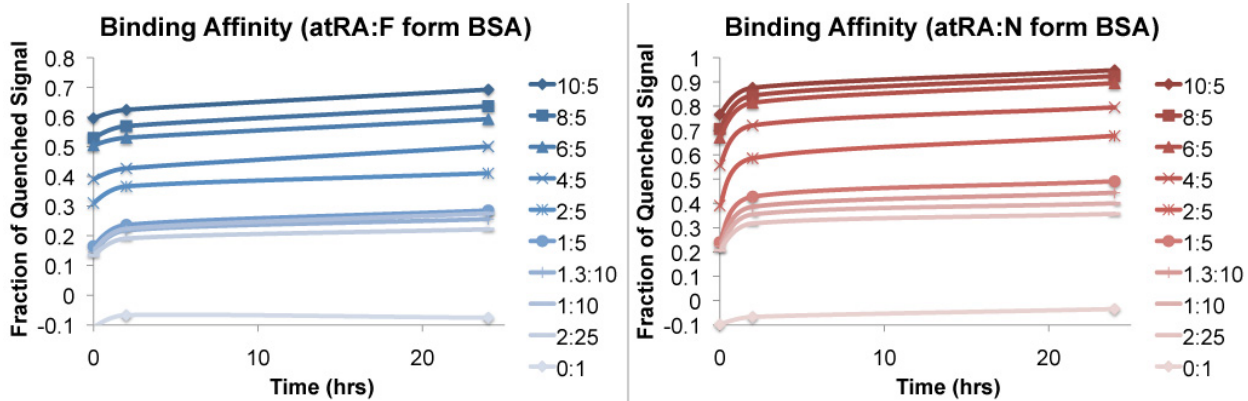


**Figure 5.2** Time evolution of atRA binding to N-form albumin and F-form albumin measured via fluorescence quenching of tryptophan residue TRP 213 at 340 nm. Within the first two hours, the degree of fluorescence quenching increases more in N-form albumin than in F-form albumin. Addition of increasing molar concentration of atRA quenches both N-form albumin and F-form albumin fluorescence intensity and increases slightly over 24 hours.

### 5.3.2 atRA binding sites determined by molecular dynamics

Computational molecular dynamics enables atomic level resolution of the interaction between albumin and atRA during several binding events. Initial random placement of atRA molecules in albumin models for N-form albumin and F-form albumin structures allow for unbiased exploration and binding of atRA molecules to the protein surfaces. Snapshots showing the progression of atRA binding to F-form and N-form albumin can be found in Appendix G and H. Final configurations after 100 ns of unconstrained simulations of atRA on N-form albumin and F-form albumin conformations are depicted in Fig. 5.3. For both structures, there are sites on the protein that were bound to a single atRA molecule (FSite1, FSite2, FSite3, NSite1, NSite2, and NSite3) and areas where clusters of atRA molecules formed an aggregate (FSite4 Cluster, NSite4 Cluster). These clusters were not formed in the water phase but rather formed after an initial atRA molecule became bound to the cluster site. In N-form albumin, atRA molecules were bound to all three domains while F-form albumin had no atRA molecules bound to domain 3 (Fig. 6, top purple). This finding is consistent with the greater effective degree of denaturation during the N-F transition on domain 3. atRA binding events on both N-form albumin and F-form albumin were, within the timescale of the simulation, irreversible. When an atRA molecule would approach the surface of the protein near a binding site, it would remain localized to that site as quantified by the successive drop in the separation distance between each atRA molecule and its nearest protein residue surface (Fig. 4.3A and B). Within 80 ns, 9 out of 10 atRA molecules were bound to the F-form albumin protein surface while all 10 atRA molecules were bound to the N-form albumin surface.

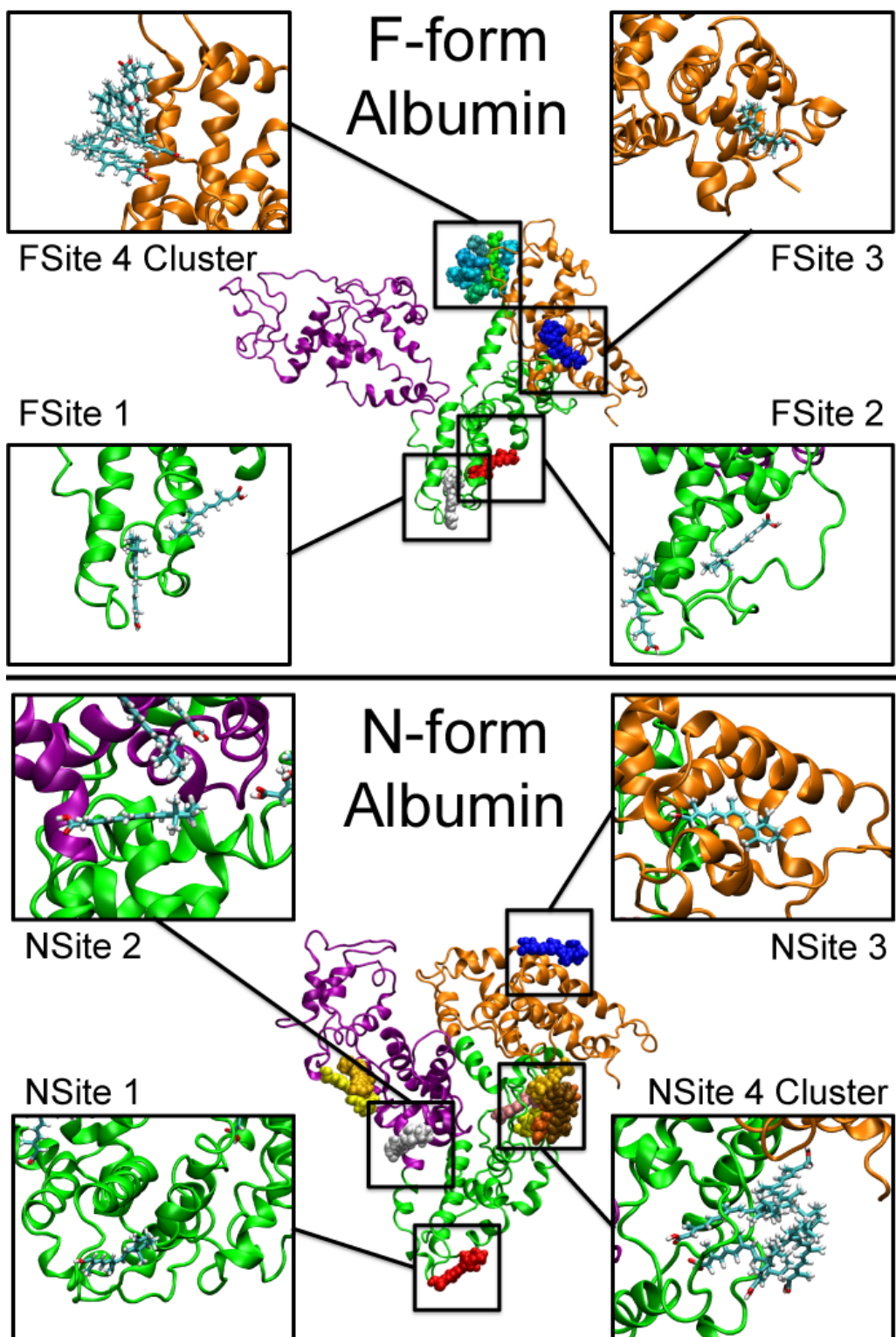
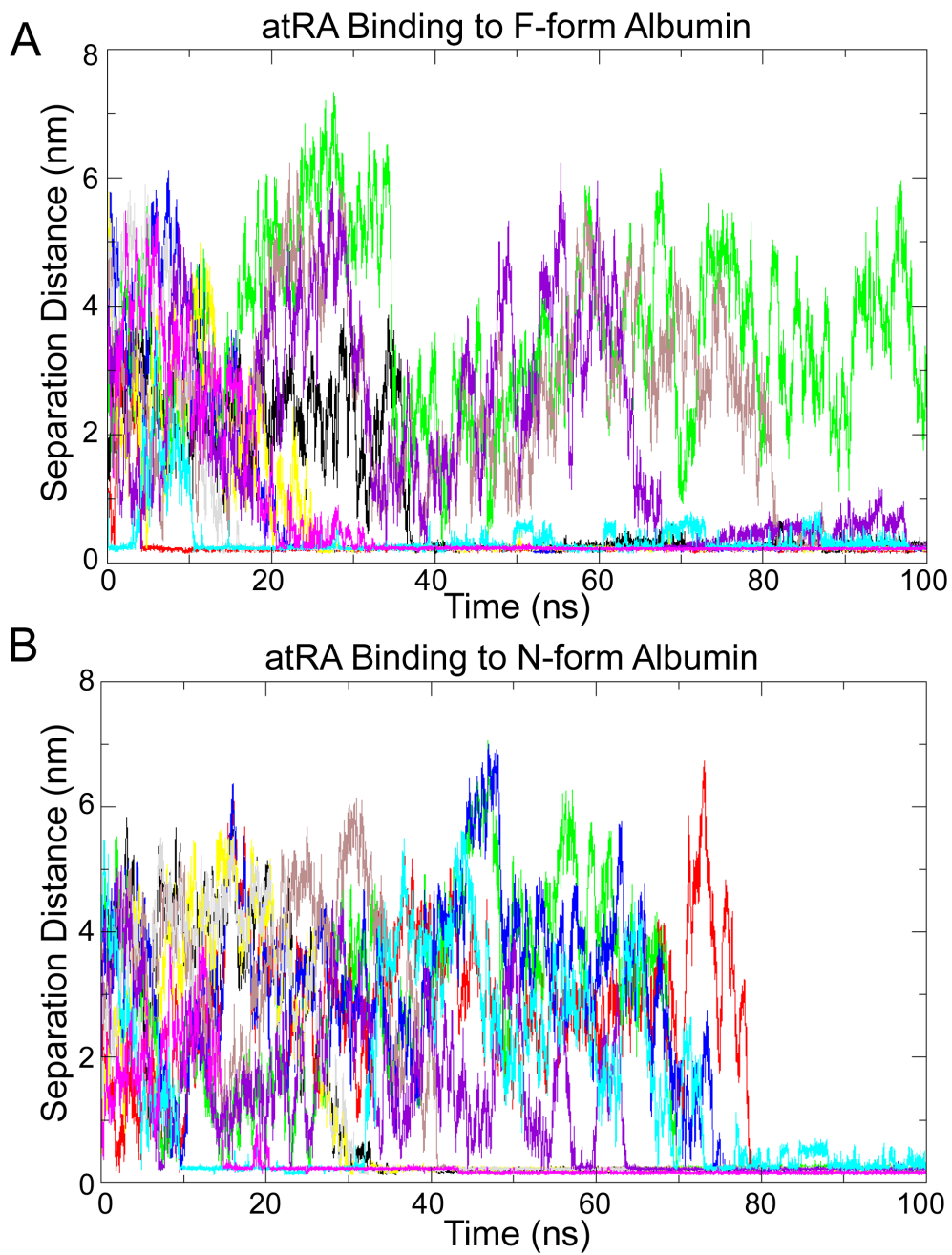


Figure 5.3 Localization of 10 atRA molecules binding to F-form albumin and N-form albumin after fully atomistic MD simulations for 100 ns. Top panel depicts F-form albumin binding sites located primarily in

domain I (orange) and II (green). Clusters of atRA also formed aggregates on the protein surface. Bottom panel depicts N-form albumin binding sites located in all three domains.



**Figure 5.4** Separation distance between individual atRA molecules and their nearest protein surface residues during 100 ns MD simulations for both F-form albumin (A) and N-form albumin (B). Each individual atRA molecule is uniquely colored and becomes bound to the protein surface when the separation distance drops below 0.14 nm. atRA molecules that bind to the surface become effectively immobilized within 100 ns timescale of the simulation. At the end of the simulation, 9/10 atRA molecules are bound to F-form albumin while 10/10 atRA molecules are bound to N-form albumin.

To ensure sufficient sampling over the entire protein surface, we can analyze the minimum distance between each residue to the nearest atRA molecule at anytime during the simulation (Fig. 5.5, bottom). Small distances  $< 0.5$  nm to the surface of a residue are used as a cutoff distance that indicate an area was visited by a nearby atRA molecule and colored in red on the protein surface (Fig. 5.5, top). With this analysis, we can immediately appreciate the red areas that match up with the observed locations identified in Figure 5.3. However, there are several areas of the protein that did not receive a visit by an atRA molecule less than 0.5 nm away so potential interactions in those regions might have been missed.

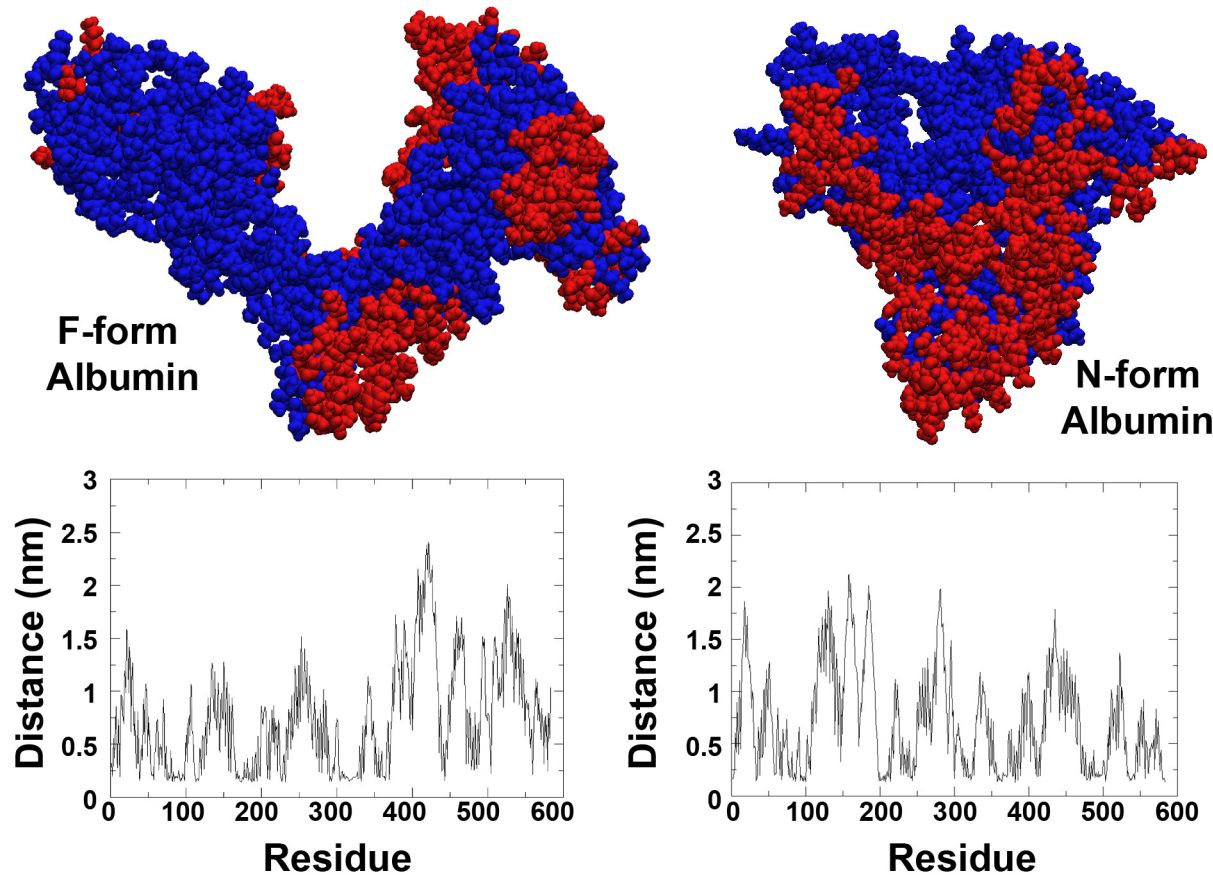


**Figure 5.5 Minimum distance mapping to nearest atRA molecule throughout the simulation.** Surface representation of F-form albumin and N-form albumin are colored red if atRA passed within  $< 0.5$  nm of the surface and blue if the distance was  $> 0.5$  nm. Distances between atRA and all residues are shown in the plots below each model.

### 5.3.3 Potential of mean force calculation for atRA binding to FSite1 and NSite1

The potential of mean force (PMF) is the free energy of interaction between two molecules. It represents the interaction between the molecules at a fixed separation averaged over all the degrees of freedom of the system, e.g. water molecules, intermolecular and intramolecular interactions and possible rotation and conformations of the protein and the atRA. Therefore, it provides the value for the work required to bring an atRA molecule from the bulk to a distance  $z$  from a BSA binding site. The potential of mean-force difference between infinity

separation, defined as zero, and that of the minimum represents the free energy of binding.

Our objective in calculating the PMF for FSite1 and NSite1 is to evaluate whether the F-form albumin conformations locked in the PBSA hydrogels retain atRA binding affinity comparable to N-form albumin. Literature estimates the binding energy for the fluorescence-quenching TRP 213 atRA binding site on N-form albumin are -31.7 kJ/mol<sup>75</sup>. Our PMF calculations show the FSite1 has a binding energy of -41 kJ/mol and the NSite1 has a binding energy of -13 kJ/mol (Fig. 5.6). The optimal separation distance between the center of mass of atRA and the center of mass on FSite1 is 0.32 nm and with NSite1 it is 0.48 nm. Taken altogether, these results demonstrate that the F-form albumin conformation retains a strong binding affinity towards atRA.

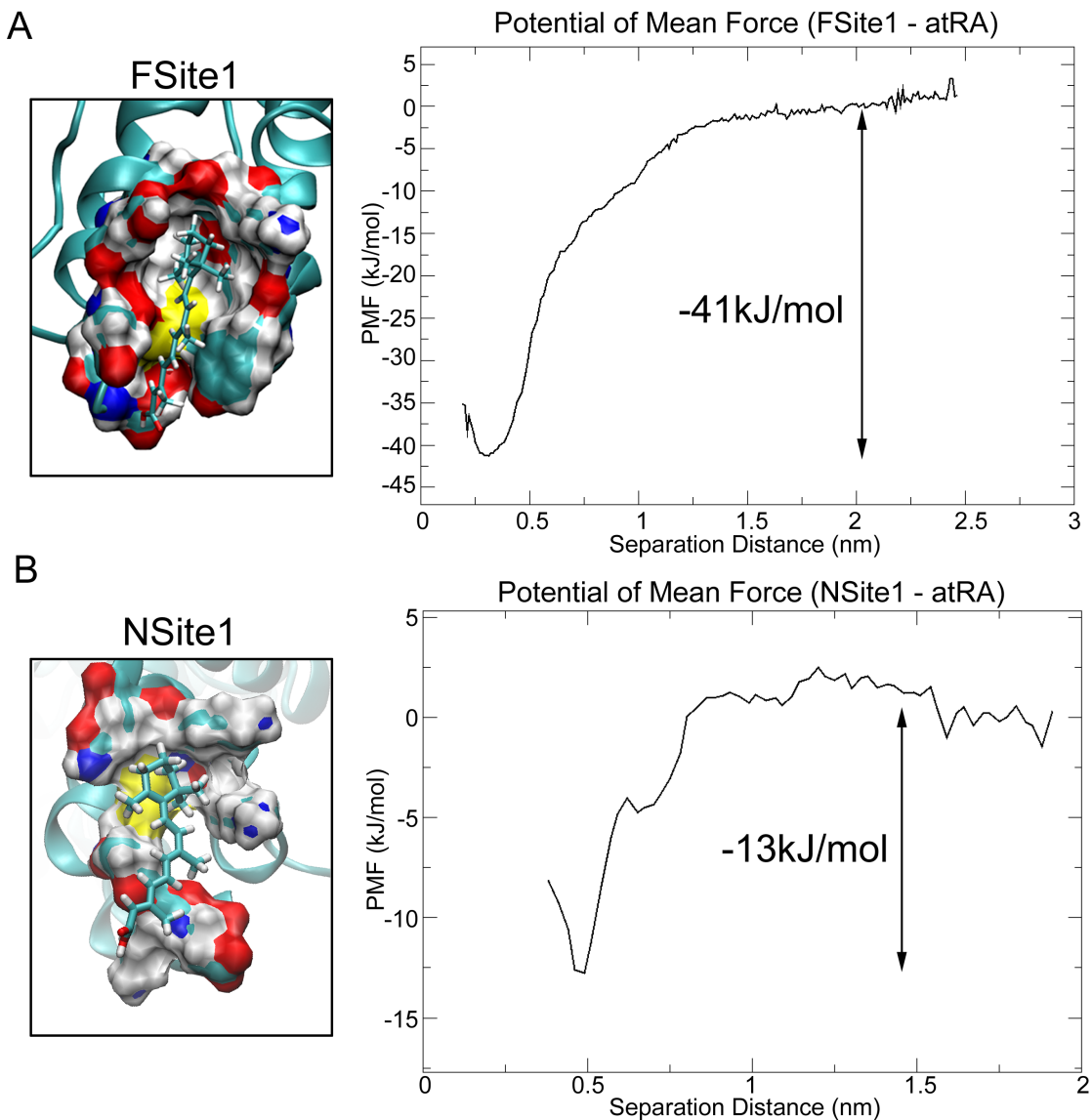


**Figure 5.6 Potential of Mean Force calculations from umbrella sampling simulations for atRA molecules entering Site 1 on both F-form albumin and N-form albumin. In this particular site, the  $\Delta G = -41 \text{ kJ/mol}$  for Site 1 on F-form albumin (a) and  $\Delta G = -13 \text{ kJ/mol}$  for Site 1 on N-form albumin (b).**

### 5.3.4 Released atRA inhibits HASMC migration

The bioactivity of atRA released from PBSA or TBSA gels was evaluated in a scratch wound assay. After allowing HASMCs to grow to 90% confluence and migration priming in serum-starved media, elution from day 10 of the release study was added to the cell culture. As

expected, the migration of positive control cells exposed directly to 25 ng/mL atRA added in the media was inhibited in comparison to the negative control cells (Fig. 5.7). This result confirms the initial bioactivity of the atRA to inhibit HASMC migration. HASMC migration for cells receiving atRA released from PBSA and TBSA gels was also inhibited and significantly different from the negative control.

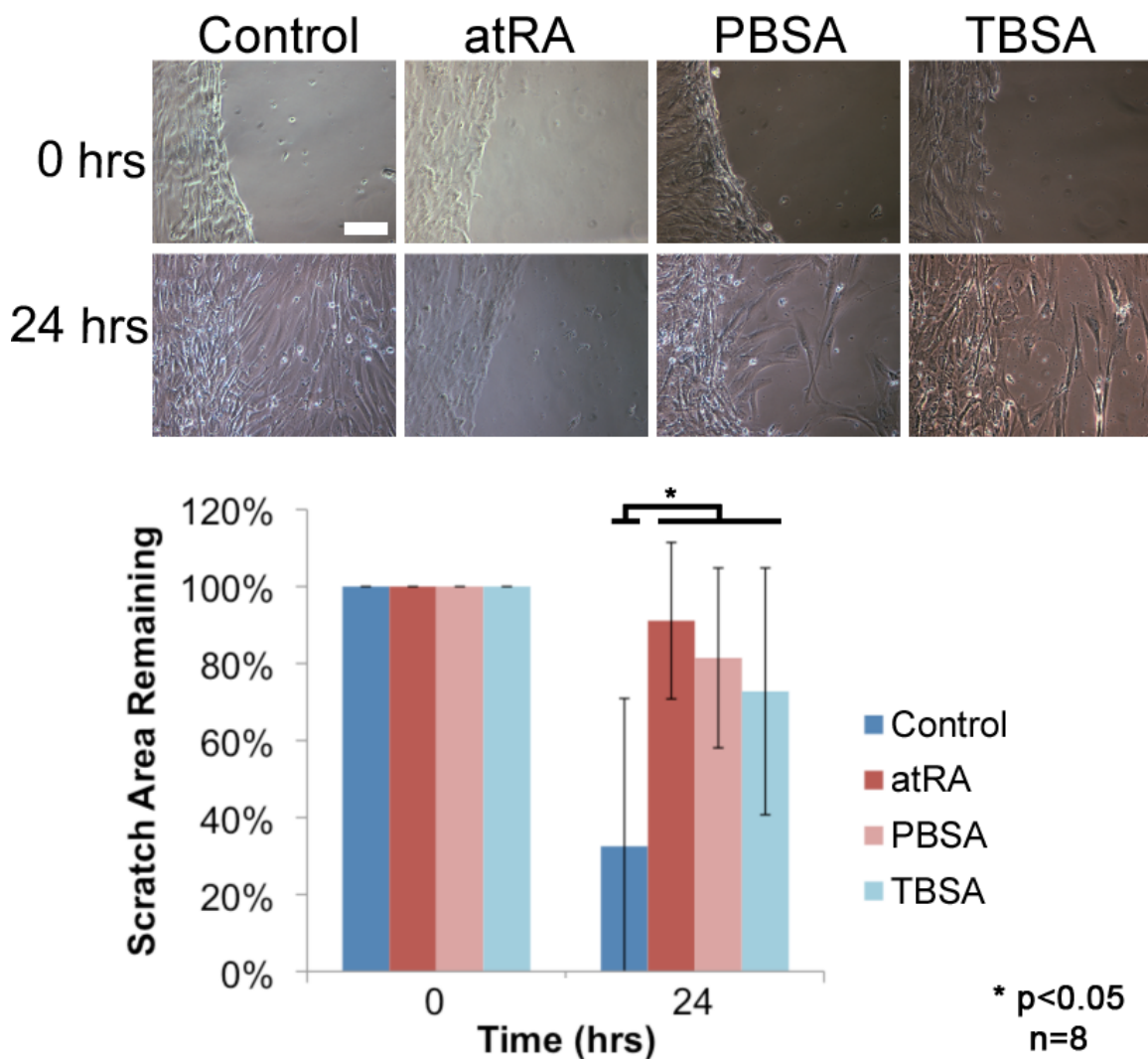


**Figure 5.7** atRA released from PBSA and TBSA hydrogels remains bioactive and reduces the migration of smooth muscle cells as evaluated by a 24 hr scratch wound assay. All cultures are serum starved to limit

proliferation. Compared to controls, all cells exposed to atRA (direct atRA, eluted from PBSA, and eluted from TBSA) exhibited a significant ( $p < 0.05$ ) reduction in cell migration. Scale bar = 100  $\mu\text{m}$ .

### 5.3.5 PBSA resistance to SDS and urea degradation due to atRA binding

Repetition of the degradation conditions that disrupted the interactions in PBSA from earlier studies in Chapter 4 were performed to evaluate whether atRA conferred any additional stability to the PBSA and TBSA hydrogels. After the atRA release experiments, samples were placed in successive solutions of 6M urea for 48 hrs, then in 10% SDS for 2 months, and finally in 8M urea for 1 month (Fig. 5.8). Interestingly, loading of atRA into the PBSA hydrogels confers a significant degree of resistance to degradation by the same mechanisms (disruption of hydrophobic interactions by urea or SDS) that had previously disrupted the hydrogel in the absence of atRA (Fig. 4.10). At the final time point, a few samples from both PBSA and TBSA were contaminated so they were not included in the final photograph. A significant degree of hydrogel swelling can be observed between the initial and the final time point. TBSA hydrogels swelled to fill the entire volume of the 24 well while the PBSA hydrogels were also swollen but not to the same extent. Sharp edges of the PBSA hydrogels became rounded while TBSA hydrogels retained their initial shape. There was also a loss of yellow coloration in the TBSA hydrogel when compared to the PBSA hydrogel.

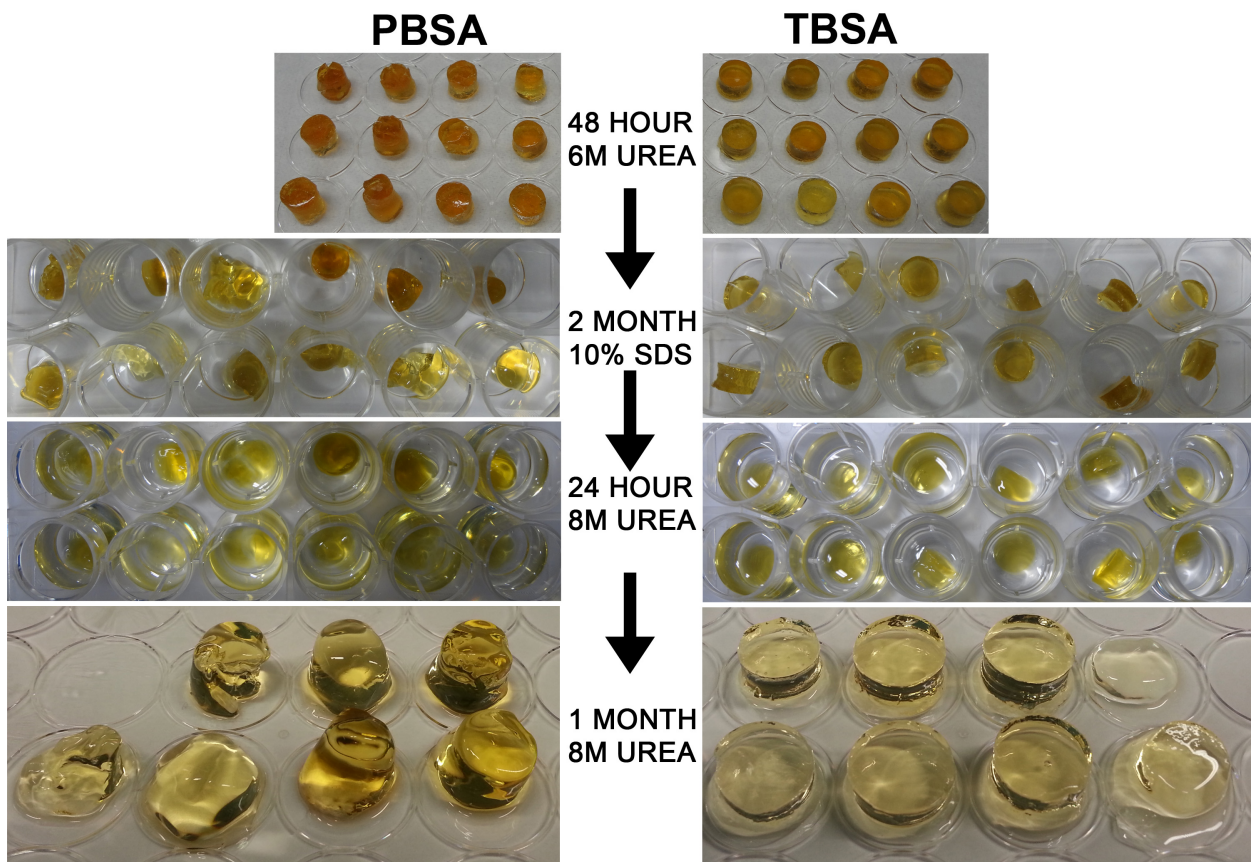


**Figure 5.8 Resistance of atRA-loaded and released PBSA and TBSA hydrogel disks to degradation by successive exposures to 6M urea, 10% SDS and 8M urea. Circles around the samples from 24 well plate are identical and are used to compare the extent of swelling.**

## 5.4 Discussion

Albumin's ability to bind therapeutic molecules is very well documented under physiological conditions, and as such has recently gained importance as a component of diagnostic and therapeutic products. For circulating albumin, the binding interactions to therapeutic molecules are a major challenge for drug development because they are rapidly cleared from circulation<sup>201</sup>. For N-form albumin, many sites have been identified including the well-known Sudlow site I and Sudlow site II located in region IIA and IIIA<sup>202</sup>.

Despite the wealth of information for N-form albumin, the interactions between F-form albumin and therapeutic molecules are limited to studies that explore albumin's denaturation resistance upon binding. The binding affinity for atRA to its preferred binding pocket on N-form albumin has been well documented<sup>75</sup>. Maiti et al.<sup>75</sup> observed via fluorescence quenching that all-*trans* retinoic acid hydrogen bonded with Trp 214 and Asp 451 residues of subdomain IIA and IIIA of albumin, respectively. Our fluorescence quenching measurements of atRA binding to F-form albumin demonstrate that there exists residual binding affinity after the N-F transition. The total fraction of fluorescence quenching is decreased in F-form albumin in comparison to N-form albumin. This may suggest the presence of alternative binding sites that limited the ability of F-form albumin to bind atRA. Further analysis by computational methods elucidates the differences in preferred atRA binding sites for both albumin forms.

The primary objective of the simulation calculations was to determine whether F-form albumin has any binding affinity for atRA. Our computational results are consistent with our experimental results and demonstrate atRA-binding affinity in both cases. The binding sites identified by the simulations were not in the same locations in the F-form compared to the N-form albumin. Binding sites for atRA on N-form albumin were located in IA, IIA, IIB, and IIIA while binding sites for F-form albumin were located in IA, IB, and IIB. Proper identification of the N-form binding sites IIA (NSite 4 Cluster) and IIIA (NSite 2) are encouraging as a validation for this approach. The binding sites identified on F-form albumin may be indicative of new undiscovered binding sites of F-form albumin. However, it is possible that incomplete sampling of the protein surface (Fig. 5.5) may hide additional sites not explored within the timescale of these simulations. With the data available, it is notable that no atRA molecules were bound to

domain 3 in the F-form (Fig. 5.3). This may be due to the disproportionate loss of secondary structure in this domain. The possible loss of the IIA and IIIA binding sites in the F-form albumin transition may help explain the decreased fluorescence quenching observed experimentally (Fig. 5.1).

Specific binding interactions are explored using the potential of mean force calculations. The observation that 9 out of 10 atRA molecules became bound to the F-form albumin and the large calculated FSite1 binding energy (-41 kJ/mol) is encouraging as evidence that F-form albumin has significant residual binding affinity for atRA. There appears to be a critical balance between the forces that govern protein structural integrity with protein functionality as reported by others<sup>150</sup>. While protein destabilization is required for hydrogel formation, too much denaturation becomes a hindrance to protein functionality and biocompatibility.

It is not unexpected that the NSite1 binding energy is not as large as the binding site reported in the literature because they are not in the same location. atRA molecules that became bound to the site reported in the literature near the TRP 213 are bound as a part of a cluster in the simulations (Fig. 5.3, NSite 4 Cluster). Calculation of a PMF for the atRA bound at this site becomes increasingly difficult due to the number of elements that need to be pulled off to generate the proper umbrella sampling. Furthermore, it is very likely that cooperative binding effects due to the presence of other atRA molecules in the cluster at the site could skew the PMF calculation away from literature values.

These binding simulations also serve as a 100 ns extension of the N-F transition (albeit in the presence of atRA). The maintenance of the F-form conformation shape (simulated for a total

of 200 ns) in the simulation is encouraging evidence to support the F-form albumin structure described in Chapter 3.

Surprisingly, the addition of atRA conferred a great deal of resistance to chemical degradation by urea or SDS. PBSA and TBSA hydrogels loaded with atRA were stable for up to three months in concentrated urea and 10% SDS, conditions that rapidly degrade PBSA hydrogels without atRA loading. These findings suggest stabilization of the PBSA hydrogel is due to the presence of atRA molecules incorporated within the hydrogel network. While this stabilization has been shown in the literature for other drugs bound to N-form albumin, this is the first report of such stabilization for atRA in F-form albumin hydrogels. This stabilization may be useful for tuning degradation behavior and modulating long-term drug release *in vivo*.

Ultimately, the released atRA from within PBSA and TBSA hydrogels demonstrated inhibition of smooth muscle cell migration in a scratch wound assay. This result suggests retained bioactivity of the atRA after release and supports the potential use of F-form albumin as a carrier of therapeutic molecules for drug delivery.

## 5.5 Conclusions

Due to albumin's versatility to bind a wide range of molecules and its intrinsic biocompatibility, it could potentially be an interesting building block for novel drug-eluting hydrogels<sup>35</sup>. However, to maintain a high degree of biocompatibility and maximize binding site functionality it is desirable not to chemically modify the protein with cross linkers to form the gels. We describe the application of partially denatured albumin hydrogels that retain intrinsic binding affinities associated with the normal configuration. We have shown that intrinsic drug

binding properties of albumin to atRA are conserved in the N-F transformation using atomistic molecular dynamics simulations and *in vitro* by fluorescence quenching. Most importantly, atRA released from PBSA hydrogels remain bioactive. While this work only explores atRA binding, it is very likely that additional binding sites are available on domains 1 and 2 for numerous other therapeutic molecules that have a natural affinity for the N-form or new affinity for the F-form.

## CHAPTER 6: THESIS SUMMARY AND RECOMMENDATIONS

### 6.1 Summary of thesis work

The main objectives of this work were to 1) develop a new crystal structure for F-form albumin to understand the effect of the N-F transition on the secondary and tertiary structure properties of albumin, 2) to determine and characterize the optimal conditions needed to fabricate partially denatured albumin hydrogels without thermal denaturation, and 3) evaluate the drug binding affinity of partially denatured albumin hydrogels. Many types of protein-based hydrogels have been described that utilize extreme denaturation conditions to promote aggregation or chemical crosslinking. However, the preservation of albumin's secondary structure and intrinsic drug binding affinity was not a focus nor factor in any of these systems.

In this work, we developed and validated an approach to generate a new crystal structure for F-form albumin. The N-F transition resulted in interdomain repulsions that exposed buried hydrophobic regions. Analysis of the F-form crystal structure showed that secondary structures were preserved in domains 1 and 2, which are critical for several classic drug-binding interactions with N-form albumin. We exploited this intrinsic partial denaturation mechanism to fabricate a new type of hydrogel driven by hydrophobic surface interactions and counter ion neutralization of protonated residues. New quaternary assemblies of aggregated F-form albumin were more compact than thermally denatured albumin hydrogels and preserved intrinsic binding affinity for atRA within unchanged protein domains 1 and 2. After release from the hydrogel,

atRA remained bioactive and inhibited the migration of smooth muscle cells *in vitro*. The resulting hydrogel was also biocompatible and exhibited rapid post-gelation degradation after *in vivo* implantation. This interdisciplinary work lays a foundation for the development of novel biocompatible albumin hydrogel drug delivery systems.

## 6.2 Recommendations for future work

This work identified several areas of inquiry that could benefit from further study; they range from improving our understanding of the F-form albumin to developing potentially new and transformative clinical and research applications. The following additional studies are recommended:

### 6.2.1 Effect of urea on the binding of atRA to F-form albumin

The stabilizing effect of atRA on the degradation of PBSA hydrogels was investigated only by experimentation in urea and SDS. With the availability of the F-form albumin crystal structures with and without the binding of atRA molecules as described in Chapter 5, it is possible to probe the effect of urea on the binding affinity of atRA computationally. Competitive binding inhibition between urea and atRA could be explored by randomly adding 10 urea molecules to the simulated model system prior to the binding of atRA to F-form albumin. Exchange interactions of atRA could be investigated by randomly adding 10 urea molecules to the model system after the binding of atRA to F-form albumin. Exchange or competitive binding for urea over atRA would indicate stripping of bound atRA molecules over time and provide an estimate for the degradation of the drug-loaded hydrogel system. Differences between this

estimate and experimental degradation rates should provide insight into the contribution of several F-form albumin molecules bundled together to protect the atRA cargo.

There are also many potential studies that could be explored to investigate the mechanisms behind the atRA stabilization effect experimentally. As a first step, mechanical characterization (via indentation testing) and rheological measurements should be performed to evaluate whether the incorporation of the atRA has any effect on the Young's modulus of the resulting drug-loaded hydrogels. If the drug loaded albumin hydrogels have an increased Young's modulus over unloaded albumin, it may suggest that the atRA is interacting with multiple partially denatured albumin molecules rather than a single albumin.

An extension of the 8M urea degradation studies is to explore the effect of the molar ratio of atRA to albumin. In this thesis, essentially two ratios were tested 0:1 (Fig. 4.10) and 8:1 (Fig. 5.8). Varying this molar ratio will likely provide an ability to modulate rate of PBSA degradation when exposed to 8M urea (ranging from 17 hrs to 1-2 months). While the results of this experiment may be interesting fundamentally, a more relevant approach will include a study of the degradation of the drug-loaded hydrogel *in vivo*. The expectation would be that an increasing concentration of hydrophobic drug would stabilize the PBSA hydrogel and result in slower *in vivo* degradation rates than the one observed in Figure 4.11. For this experiment, a substitute for atRA could be made with another hydrophobic molecule like LCFA to isolate the effect of the stabilizing hydrophobic moiety without the confounding factor of atRA release *in vivo*. Consequently, inclusion of LCFA as the model hydrophobic "drug" should be tested first to confirm that this molecule also has a stabilizing effect on PBSA hydrogels when exposed to 8M urea. Beyond atRA and LCFA, there are a number of additional therapeutic molecules that have

a binding affinity to HSA and BSA as discussed in Chapter 2. These molecules are discussed in the next section and could serve as alternative hydrogel stabilizing molecules for different applications. Preliminary work with HSA shows that while they can form PHSA hydrogels successfully, they are weaker than the PBSA hydrogels and as a result may require the presence of a stabilizing molecule for any clinical application.

### 6.2.2 F-form crystal structure for HSA and other drug interactions

While HSA and BSA are close homologs (85.5% structural similarity, 75.6% sequence identity match)<sup>171</sup> and can provide high-level prediction of comparable crystal structure conformations, the clinically relevant molecule for use in humans is HSA or the cheaper transgenic rice recombinant HSA (rHSA) substitute<sup>34,203-205</sup>. Preliminary experiments using the methods described in Chapter 4 successfully fabricated PHSA hydrogels similar to the PBSA described in this work. MD simulations should be performed on N-form crystal structures of HSA and rHSA to determine their partially denatured F-form crystal structures. With these new F-form crystal structures it will be possible to further characterize the drug binding interactions and potentially identify new binding sites for a variety of other therapeutic molecules not explored here<sup>32,33</sup>. Potential candidates for further drug-F-form albumin interaction studies include cisplatin<sup>68</sup>, warfarin<sup>51</sup>, phenylbutazone<sup>51</sup>, azapropazone<sup>52</sup>, indomethacin<sup>53,54</sup>, tolbutamide<sup>55</sup>, iodipamide<sup>51</sup>, iophenoxic acid<sup>55</sup>, furosemide<sup>56</sup>, bucolome<sup>56</sup>, sulfisoxazole<sup>57</sup>, diazepam<sup>51</sup>, diflunisal<sup>58</sup>, ibuprofen<sup>51</sup>, ketoprofen<sup>59</sup>, naproxen<sup>60</sup>, 6-MNA<sup>61</sup>, diclofenac<sup>61</sup>, etodolac<sup>62</sup>, clofibrate<sup>63</sup>, iopanoic acid<sup>55</sup>, probenecid<sup>70</sup>, amitriptyline<sup>70</sup>, debrisoquine<sup>70</sup>, digitoxin<sup>71,72</sup>, propofol<sup>64</sup>, fusidic acid<sup>65</sup>, lidocaine<sup>66</sup>, bicalutamide<sup>32</sup>, camptothecin<sup>32</sup>, 9-amino

camptothecin<sup>32</sup>, idarubicin<sup>32</sup>, teniposide<sup>32</sup>, and etoposide<sup>32</sup>. Combination of these MD simulations with AutoDock studies can also be performed as was done with HSA and betulinic acid (-35 kJ/mol)<sup>206</sup>. Interaction with these therapeutic molecules and the PBSA or PHSA systems may confer additional degradation resistance as shown by the atRA example in Chapter 5. Exploration of binding interactions between the therapeutic molecules listed here and F-form should also consider the change in degradation rates when exposed to urea (as a comparison to earlier work) and also in physiological conditions (i.e. exposure to proteases or *in vivo* implantation).

### 6.2.3 F-form albumin microparticle fabrication for drug delivery

We have also developed a preliminary scalable and inexpensive technique to prepare albumin microparticles that exploit the F-form albumin structures. As a proof of concept, a simple automotive paint sprayer aerosolizes a solution of albumin at physiological pH 7.4 (Fig. 6.1, left). The particle spray falls into a bath at pH 3.5 resulting in immediate partial denaturation of the albumin and formation of spherical particles (ranging from 100 nm - 2.5 µm in diameter) from the spray (Fig. 6.1, right). Through this partial denaturation procedure, therapeutic molecules could be bound to albumin at different stages, either prior to aerosolization or after gelation. After particle formation, the acid used in the spray bath can be neutralized without altering the microparticles.

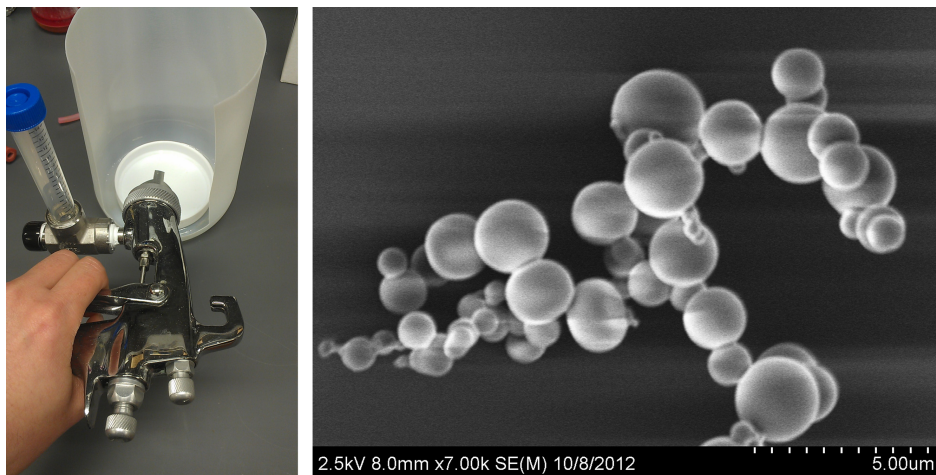


**Figure 6.1 Preliminary PBSA microparticle fabrication setup.**

The main goal of such a project would be to develop fabrication parameters utilizing a more sophisticated spray system and characterize the pharmacokinetic profile of several molecules entrapped in the albumin microparticles. This work could include optimization of process parameters such as the pH of bath solution, height of spray, spray pressure, nozzle geometry, protein concentration, therapeutic molecule of interest, and the bath temperature to control microparticle formation, geometry, size distribution, and storage stability. Success would be determined by the establishment of process parameter guidelines that result in fabrication of reproducible particle properties and the confirmed bioactivity of therapeutic molecules with desired pharmacokinetic profiles.

Finally, the previous discussion of atRA, LCFA, or potentially other therapeutic molecules demonstrating a stabilizing effect on the PBSA hydrogel could also be application to the stabilization of a nanoparticle PBSA formulation. Therapeutics could either be added into the solution of albumin prior to aerosolization or into the low pH bath for loading into the hydrogels. In the first case, therapeutics added to the pre-aerosolized albumin solution would bind to N-form binding sites, which may stabilize the albumin during partial degradation to the F-form. If

this is the case, lowering the pH of the bath could induce the necessary partial denaturation of the albumin. In the second case, the therapeutics should be stable in a low pH environment and will bind to the F-form albumin as it is sprayed into the bath. In either case, inclusion of therapeutics may be able to further stabilize the PBSA nanoparticle system as observed preliminarily in the bulk PBSA hydrogel observations.

#### **6.2.4 Summary and Outlook**

We have demonstrated that albumin can form hydrogels via low-pH electrostatically triggered self-assembly and that the resulting neutralized hydrogels are biocompatible and biodegradable when studied in a rat subcutaneous pocket implant model. We have also demonstrated the feasibility of forming albumin microparticles that exploit this property using a proof of concept spray technique. Residual binding affinity of albumin preserved in the N-F transition may yield novel drug binding interactions that could be exploited for drug release from F-form albumin microparticles. This work could become the basis for a highly versatile drug delivery platform.

## REFERENCES

- 1 Elzoghby, A. O., Samy, W. M. & Elgindy, N. A. Protein-based nanocarriers as promising drug and gene delivery systems. *J Control Release* **161**, 38-49, doi:Doi 10.1016/J.Jconrel.2012.04.036 (2012).
- 2 Elzoghby, A. O., Samy, W. M. & Elgindy, N. A. Albumin-based nanoparticles as potential controlled release drug delivery systems. *J Control Release* **157**, 168-182, doi:Doi 10.1016/J.Jconrel.2011.07.031 (2012).
- 3 Doi, E. Gels and Gelling of Globular-Proteins. *Trends Food Sci Tech* **4**, 1-5 (1993).
- 4 Barone, G. *et al.* Thermal denaturation of bovine serum albumin and its oligomers and derivatives pH dependence. *J Therm Anal* **45**, 1255-1264 (1995).
- 5 Baier, S. K., Decker, E. A. & McClements, D. J. Impact of glycerol on thermostability and heat-induced gelation of bovine serum albumin. *Food Hydrocolloid* **18**, 91-100, doi:Doi 10.1016/S0268-005x(03)00046-8 (2004).
- 6 Davila, E., Pares, D., Cuvelier, G. & Relkin, P. Heat-induced gelation of porcine blood plasma proteins as affected by pH. *Meat Sci* **76**, 216-225, doi:Doi 10.1016/J.Meatsci.2006.11.002 (2007).
- 7 Gosal, W. S. & Ross-Murphy, S. B. Globular protein gelation. *Curr Opin Colloid In* **5**, 188-194 (2000).
- 8 Murata, M., Tani, F., Higasa, T., Kitabatake, N. & Doi, E. Heat-Induced Transparent Gel Formation of Bovine Serum-Albumin. *Biosci Biotech Bioch* **57**, 43-46 (1993).
- 9 Navarra, G. *et al.* Thermal aggregation and ion-induced cold-gelation of bovine serum albumin. *Eur Biophys J Biophy* **38**, 437-446, doi:Doi 10.1007/S00249-008-0389-6 (2009).
- 10 Ross-Murphy, S. B. Physical gelation of biopolymers. *Food Hydrocolloid* **1**, 485-495 (1987).

- 11 Gan, C. Y., Alkarkhi, A. F. M. & Easa, A. M. Using response surface methodology to optimize process parameters and cross-linking agents for production of combined-cross-linked bovine serum albumin gels. *J Biosci Bioeng* **107**, 366-372, doi:Doi 10.1016/J.Jbiosc.2008.12.007 (2009).
- 12 Gan, C. Y. et al. Combined cross-linking treatments of bovine serum albumin gel beadlets for controlled-delivery of caffeine. *Food Hydrocolloid* **23**, 1398-1405, doi:Doi 10.1016/J.Foodhyd.2008.09.009 (2009).
- 13 Iemma, F. et al. Radical cross-linked albumin microspheres as potential drug delivery systems: Preparation and in vitro studies. *Drug Deliv* **12**, 229-234, doi:Doi 10.1080/10717540590952690 (2005).
- 14 Taguchi, K. et al. Superior Plasma Retention of a Cross-Linked Human Serum Albumin Dimer in Nephrotic Rats as a New Type of Plasma Expander. *Drug Metab Dispos* **38**, 2124-2129, doi:Doi 10.1124/Dmd.109.031989 (2010).
- 15 Yamazoe, H., Oyane, A., Nashima, T. & Ito, A. Reduced platelet adhesion and blood coagulation on cross-linked albumin films. *Mat Sci Eng C-Mater* **30**, 812-816, doi:Doi 10.1016/J.Msec.2010.03.015 (2010).
- 16 Zhang, S. G. Fabrication of novel biomaterials through molecular self-assembly. *Nat Biotechnol* **21**, 1171-1178, doi:Doi 10.1038/Nbt874 (2003).
- 17 Peppas, N. A., Hilt, J. Z., Khademhosseini, A. & Langer, R. Hydrogels in biology and medicine: From molecular principles to bionanotechnology. *Adv Mater* **18**, 1345-1360, doi:Doi 10.1002/Adma.200501612 (2006).
- 18 Slaughter, B. V., Khurshid, S. S., Fisher, O. Z., Khademhosseini, A. & Peppas, N. A. Hydrogels in Regenerative Medicine. *Adv Mater* **21**, 3307-3329, doi:Doi 10.1002/Adma.200802106 (2009).
- 19 Gupta, P., Vermani, K. & Garg, S. Hydrogels: from controlled release to pH-responsive drug delivery. *Drug Discov Today* **7**, 569-579, doi:Pii S1359-6446(02)02255-9 (2002).
- 20 Whitesides, G. M., Ostuni, E., Takayama, S., Jiang, X. Y. & Ingber, D. E. Soft lithography in biology and biochemistry. *Annual Review of Biomedical Engineering* **3**, 335-373, doi:Doi 10.1146/Annurev.Bioeng.3.1.335 (2001).

- 21 Hassan, C. M. & Peppas, N. A. Structure and morphology of freeze/thawed PVA hydrogels. *Macromolecules* **33**, 2472-2479, doi:Doi 10.1021/Ma9907587 (2000).
- 22 Huh, K. M. & Bae, Y. H. Synthesis and characterization of poly(ethylene glycol)/poly(L-lactic acid) alternating multiblock copolymers. *Polymer* **40**, 6147-6155, doi:Doi 10.1016/S0032-3861(98)00822-2 (1999).
- 23 Mikos, A. G. *et al.* Preparation and Characterization of Poly(L-Lactic Acid) Foams. *Polymer* **35**, 1068-1077, doi:Doi 10.1016/0032-3861(94)90953-9 (1994).
- 24 Wichterle, O. & Lim, D. Hydrophilic Gels for Biological Use. *Nature* **185**, 117-118, doi:Doi 10.1038/185117a0 (1960).
- 25 Merrill, E. W. *et al.* Platelet Retention on Polymer Surfaces - Some Invitro Experiments. *Adv Chem Ser*, 35-42 (1982).
- 26 Yang, J., Webb, A. R., Pickerill, S. J., Hageman, G. & Ameer, G. A. Synthesis and evaluation of poly(diol citrate) biodegradable elastomers. *Biomaterials* **27**, 1889-1898, doi:Doi 10.1016/J.Biomaterials.2005.05.106 (2006).
- 27 Arternova, N. V., Kasakov, A. S., Burnagina, Z. M., Lyutova, E. M. & Gurvits, B. Y. Protein aggregates as depots for the release of biologically active compounds. *Biochem Bioph Res Co* **377**, 595-599, doi:Doi 10.1016/J.Bbrc.2008.10.015 (2008).
- 28 Carter, D. C. in *Burger's Medicinal Chemistry, Drug Discovery, and Development* (ed Donald J. Abraham and David P. Rotella) (John Wiley and Sons, Inc., 2010).
- 29 Sleep, D., Cameron, J. & Evans, L. R. Albumin as a versatile platform for drug half-life extension. *Bba-Gen Subjects* **1830**, 5526-5534, doi:Doi 10.1016/J.Bbagen.2013.04.023 (2013).
- 30 Sulkowska, A. Interaction of drugs with bovine and human serum albumin. *J Mol Struct* **614**, 227-232, doi:Pii S0022-2860(02)00256-9  
Doi 10.1016/S0022-2860(02)00256-9 (2002).

- 31 Sulkowska, A., Rownicka, J., Bojko, B. & Sulkowski, W. Interaction of anticancer drugs with human and bovine serum albumin. *J Mol Struct* **651**, 133-140, doi:Pii S0022-2860(02)00642-7  
Doi 10.1016/S0022-2860(02)00642-7 (2003).
- 32 Wang, Z. M. *et al.* Structural studies of several clinically important oncology drugs in complex with human serum albumin. *Bba-Gen Subjects* **1830**, 5356-5374, doi:Doi 10.1016/J.Bbagen.2013.06.032 (2013).
- 33 Yamasaki, K., Chuang, V. T. G., Maruyama, T. & Otagiri, M. Albumin-drug interaction and its clinical implication. *Bba-Gen Subjects* **1830**, 5435-5443, doi:Doi 10.1016/J.Bbagen.2013.05.005 (2013).
- 34 Fanali, G. *et al.* Human serum albumin: From bench to bedside. *Molecular Aspects of Medicine* **33**, 209-290, doi:Doi 10.1016/J.Mam.2011.12.002 (2012).
- 35 Peters, T. *All About Albumin*. 1-432 (Elsevier, 1995).
- 36 Geisow, M. Serum-Albumin Structure and Function. *Nature* **270**, 476-477, doi:Doi 10.1038/270476a0 (1977).
- 37 Peters, T. & Stewart, A. J. Albumin research in the 21st century Preface. *Bba-Gen Subjects* **1830**, 5351-5353, doi:Doi 10.1016/J.Bbagen.2013.05.012 (2013).
- 38 Carter, D. C. & Ho, J. X. Structure of Serum-Albumin. *Advances in Protein Chemistry, Vol 45* **45**, 153-203 (1994).
- 39 Gelamo, E. L., Silva, C. H. T. P., Imasato, H. & Tabak, M. Interaction of bovine (BSA) and human (HSA) serum albumins with ionic surfactants: spectroscopy and modelling. *Bba-Protein Struct M* **1594**, 84-99 (2002).
- 40 Michnik, A., Michalik, K., Kluczewska, A. & Drzazga, Z. Comparative DSC study of human and bovine serum albumin. *J Therm Anal Calorim* **84**, 113-117, doi:Doi 10.1007/S10973-005-7170-1 (2006).
- 41 Waldmann, T. A. *Albumin Structure, Function and Uses*. 255-273 (Pergamon, 1977).

- 42 Reed, R. G. Location of Long-Chain Fatty Acid-Binding Sites of Bovine Serum-Albumin by Affinity Labeling. *J Biol Chem* **261**, 5619-5624 (1986).
- 43 Leggio, C., Galantini, L. & Pavel, N. V. About the albumin structure in solution: cigar Expanded form versus heart Normal shape. *Phys Chem Chem Phys* **10**, 6741-6750, doi:Doi 10.1039/B808938h (2008).
- 44 Hilger, C. *et al.* Differential binding of IgG and IgA antibodies to antigenic determinants of bovine serum albumin. *Clin Exp Immunol* **123**, 387-394 (2001).
- 45 Mcardle, C. Disulphide Bonds and Secondary Structure of Human Serum Albumin. *Biochem J* **101**, P10-& (1966).
- 46 Paris, G., Kraszewski, S., Ramseyer, C. & Enescu, M. About the structural role of disulfide bridges in serum albumins: Evidence from protein simulated unfolding. *Biopolymers* **97**, 889-898, doi:Doi 10.1002/Bip.22096 (2012).
- 47 Bohme, U., Scheler, U. Effective charge of bovine serum albumin determined by electrophoresis NMR. *Chem. Phys. Lett.* **435**, 342-345, doi:doi:10.1016/j.cplett.2006.12.068 (2007).
- 48 Fujiwara, S. & Amisaki, T. Fatty acid binding to serum albumin: Molecular simulation approaches. *Bba-Gen Subjects* **1830**, 5427-5434, doi:Doi 10.1016/J.Bbagen.2013.03.032 (2013).
- 49 Brandt, J., Fredriks.M & Andersso.Lo. Coupling of Dyes to Biopolymers by Sensitized Photooxidation - Affinity Labeling of a Binding-Site in Bovine Serum-Albumin. *Biochemistry-Us* **13**, 4758-4764 (1974).
- 50 Militello, V., Vetri, V. & Leone, M. Conformational changes involved in thermal aggregation processes of bovine serum albumin. *Biophys Chem* **105**, 133-141, doi:Doi 10.1016/S0301-4622(03)00153-4 (2003).
- 51 Yamasaki, K., Maruyama, T., KraghHansen, U. & Otagiri, M. Characterization of site I on human serum albumin: Concept about the structure of a drug binding site. *Bba-Protein Struct M* **1295**, 147-157, doi:Doi 10.1016/0167-4838(96)00013-1 (1996).

- 52 Kragh-Hansen, U. Evidence for a Large and Flexible Region of Human-Serum Albumin Possessing High-Affinity Binding-Sites for Salicylate, Warfarin, and Other Ligands. *Mol Pharmacol* **34**, 160-171 (1988).
- 53 Montero, M. T., Pouplana, R., Valls, O. & Garcia, S. On the Binding of Cinmetacin and Indomethacin to Human-Serum Albumin. *J Pharm Pharmacol* **38**, 925-927 (1986).
- 54 Zini, R., Dathis, P., Barre, J. & Tillement, J. P. Binding of Indomethacin to Human-Serum Albumin - Its Non Displacement by Various Agents, Influence of Free Fatty-Acids and the Unexpected Effect of Indomethacin on Warfarin-Binding. *Biochem Pharmacol* **28**, 2661-2665, doi:Doi 10.1016/0006-2952(79)90043-1 (1979).
- 55 Vallner, J. J. Binding of Drugs by Albumin and Plasma-Protein. *J Pharm Sci-US* **66**, 447-465, doi:Doi 10.1002/Jps.2600660402 (1977).
- 56 Takamura, N. *et al.* Bucolome, a potent binding inhibitor for furosemide, alters the pharmacokinetics and diuretic effect of furosemide: Potential for use of bucolome to restore diuretic response in nephrotic syndrome. *Drug Metab Dispos* **33**, 596-602, doi:Doi 10.1124/Dmd.104.002782 (2005).
- 57 Anton, A. H. Increasing Activity of Sulfonamides with Displacing Agents - Review. *Annals of the New York Academy of Sciences* **226**, 273-292, doi:Doi 10.1111/J.1749-6632.1973.Tb20490.X (1973).
- 58 Verbeeck, R. K., Boel, A., Buntinx, A. & Deschepper, P. J. Plasma-Protein Binding and Interaction Studies with Diflunisal, a New Salicylate Analgesic. *Biochem Pharmacol* **29**, 571-576, doi:Doi 10.1016/0006-2952(80)90378-0 (1980).
- 59 Chuang, V. T. G. *et al.* Helix 6 of subdomain III A of human serum albumin is the region primarily photolabeled by ketoprofen, an arylpropionic acid NSAID containing a benzophenone moiety. *Bba-Protein Struct M* **1434**, 18-30, doi:Doi 10.1016/S0167-4838(99)00174-0 (1999).
- 60 Honore, B. & Brodersen, R. Albumin Binding of Anti-Inflammatory Drugs - Utility of a Site-Oriented Versus a Stoichiometric Analysis. *Mol Pharmacol* **25**, 137-150 (1984).
- 61 Setoguchi, N. *et al.* A diclofenac suppositorynabumetone combination therapy for arthritic pain relief and a monitoring method for the diclofenac binding capacity of HSA

- site II in rheumatoid arthritis. *Biopharm Drug Dispos* **34**, 125-136, doi:Doi 10.1002/Bdd.1829 (2013).
- 62 Mignot, I. *et al.* Albumin binding sites for etodolac enantiomers. *Chirality* **8**, 271-280, doi:Doi 10.1002/(Sici)1520-636x(1996)8:3<271::Aid-Chir7>3.0.Co;2-K (1996).
- 63 Meisner, H. & Neet, K. Competitive Binding of Long-Chain Free Fatty-Acids, Octanoate, and Chlorophenoxyisobutyrate to Albumin. *Mol Pharmacol* **14**, 337-346 (1978).
- 64 Bhattacharya, A. A., Curry, S. & Franks, N. P. Binding of the general anesthetics propofol and halothane to human serum albumin - High resolution crystal structures. *J Biol Chem* **275**, 38731-38738, doi:Doi 10.1074/Jbc.M005460200 (2000).
- 65 Zunszain, P. A., Ghuman, J., McDonagh, A. F. & Curry, S. Crystallographic analysis of human serum albumin complexed with 4Z,15E-bilirubin-IX alpha. *J Mol Biol* **381**, 394-406, doi:Doi 10.1016/J.Jmb.2008.06.016 (2008).
- 66 Hein, K. L. *et al.* Crystallographic analysis reveals a unique lidocaine binding site on human serum albumin. *J Struct Biol* **171**, 353-360, doi:Doi 10.1016/J.Jsb.2010.03.014 (2010).
- 67 Sudlow, G., Birkett, D. J. & Wade, D. N. Spectroscopic Techniques in Study of Protein-Binding - Fluorescence Technique for Evaluation of Albumin Binding and Displacement of Warfarin and Warfarin-Alcohol. *Clin Exp Pharmacol P* **2**, 129-140, doi:Doi 10.1111/J.1440-1681.1975.Tb01826.X (1975).
- 68 Ivanov, A. I. *et al.* Cisplatin binding sites on human albumin. *J Biol Chem* **273**, 14721-14730, doi:Doi 10.1074/Jbc.273.24.14721 (1998).
- 69 Keaney, J. S., DI; Stamler, JS, et al. NO Forms an Adduct with Serum-Albumin that has Endothelium Derived Relaxing Factor-Like Properties. *Journal of Clinical Investigation* **91**, 1582-1589 (1993).
- 70 Sudlow, G., Birkett, D. J. & Wade, D. N. Further Characterization of Specific Drug Binding-Sites on Human-Serum Albumin. *Mol Pharmacol* **12**, 1052-1061 (1976).

- 71 Kragh-Hansen, U. Relations between High-Affinity Binding-Sites of Markers for Binding Regions on Human-Serum Albumin. *Biochem J* **225**, 629-638 (1985).
- 72 Sjoholm, I. *et al.* Binding of Drugs to Human-Serum Albumin .11. Specificity of 3 Binding-Sites as Studied with Albumin Immobilized in Microparticles. *Mol Pharmacol* **16**, 767-777 (1979).
- 73 Fogh-Andersen, N. E., I; Lokkegaard, H, et al. Changes in blood and plasma volume during treatment with recombinant human erythropoietin. . *Scand. J. Clin. Lab Invest. Suppl* **214**, 61-65 (1993).
- 74 Jin, Y. J., Li, W.L., Wang, Q.R. Tb(III) as a Fluorescent Probe for the Structure of Bovine Serum Albumin. *Biochem. Biophys. Res. Commun.* **177**, 474-479 (1991).
- 75 Maiti, T. K., Ghosh, K. S., Debnath, J. & Dasgupta, S. Binding of all-trans retinoic acid to human serum albumin: Fluorescence, FT-IR and circular dichroism studies. *Int J Biol Macromol* **38**, 197-202, doi:Doi 10.1016/J.Ijb biomac.2006.02.015 (2006).
- 76 Ozpolat, B. & Lopez-Berestein, G. Liposomal-all-trans-retinoic acid in treatment of acute promyelocytic leukemia. *Leukemia Lymphoma* **43**, 933-941, doi:Doi 10.1080/10428190290021678 (2002).
- 77 Bargetzi, M. J., Tichelli, A., Gratwohl, A. & Speck, B. Oral all-trans retinoic acid (ATRA): Administration in intubated patients with acute promyelocytic leukemia. *Schweiz Med Wschr* **126**, 1944-1945 (1996).
- 78 Lefebvre, P. *et al.* Pharmacokinetics of Oral All-Trans Retinoic Acid in Patients with Acute Promyelocytic Leukemia. *Leukemia* **5**, 1054-1058 (1991).
- 79 Muindi, J. R. F. *et al.* Clinical-Pharmacology of Oral All-Trans Retinoic Acid in Patients with Acute Promyelocytic Leukemia. *Cancer Res* **52**, 2138-2142 (1992).
- 80 Saiag, P. *et al.* Treatment of early AIDS-related Kaposi's sarcoma with oral all-trans-retinoic acid: results of a sequential non-randomized phase II trial. *Aids* **12**, 2169-2176 (1998).

- 81 Choi, Y. *et al.* Inhibition of tumor growth by biodegradable microspheres containing all-trans-retinoic acid in a human head-and-neck cancer xenograft. *Int J Cancer* **107**, 145-148, doi:Doi 10.1002/Ijc.11354 (2003).
- 82 Um, S. J. *et al.* Antiproliferative mechanism of retinoid derivatives in ovarian cancer cells. *Cancer Lett* **174**, 127-134 (2001).
- 83 Hameed, D. A. & El-Metwally, T. H. The effectiveness of retinoic acid treatment in bladder cancer - Impact on recurrence, survival and TGF alpha and VEGF as end-point biomarkers. *Cancer Biol Ther* **7**, 92-100 (2008).
- 84 Reynolds, C. P., Matthay, K. K., Villablanca, J. G. & Maurer, B. J. Retinoid therapy of high-risk neuroblastoma. *Cancer Lett* **197**, 185-192, doi:Doi 10.1016/S0304-3835(03)00108-3 (2003).
- 85 Shatokhin, Y. V., Smolyantiskaya, P. G., Snezhko, I. V. & Shatokhina, O. N. Cyclosporin and vesanoid therapy of myelodysplastic syndrome. *Gematol Transfuziol* **51**, 22-28 (2006).
- 86 Bryan, M. *et al.* A pilot phase II trial of all-trans retinoic acid (Vesanoid) and paclitaxel (Taxol) in patients with recurrent or metastatic breast cancer. *Invest New Drug* **29**, 1482-1487, doi:Doi 10.1007/S10637-010-9478-3 (2011).
- 87 Mao, J. T. *et al.* A pilot study of all-trans-retinoic acid for the treatment of human emphysema. *Am J Resp Crit Care* **165**, 718-723, doi:Doi 10.1164/Rccm.2106123 (2002).
- 88 Roth, M. D. *et al.* Feasibility of retinoids for the treatment of emphysema study. *Chest* **130**, 1334-1345, doi:Doi 10.1378/Chest.130.5.1334 (2006).
- 89 Cortes-Franco, J. *et al.* A Phase II Study of Oral Tamibarotene in Acute Promyelocytic Leukemia (APL) Patients (PTS) Who Have Received Prior Therapy with All-Trans Retinoic Acid and Arsenic Trioxide (STAR-1 trial). *Blood* **114**, 809-810 (2009).
- 90 Errico, C., Gazzarri, M. & Chiellini, F. A Novel Method for the Preparation of Retinoic Acid-Loaded Nanoparticles. *Int J Mol Sci* **10**, 2336-2347, doi:Doi 10.3390/Ijms10052336 (2009).

- 91 Stratigos, A. J. & Katsambas, A. D. The role of topical retinoids in the treatment of photoaging. *Drugs* **65**, 1061-1072, doi:Doi 10.2165/00003495-200565080-00003 (2005).
- 92 Huang, M. E. *et al.* Use of All-Trans Retinoic Acid in the Treatment of Acute Promyelocytic Leukemia. *Blood* **72**, 567-572 (1988).
- 93 Sanz, M. A. Risk-adapted treatment of acute promyelocytic leukemia with AIDA derived regimens: The Pethema experience. *Ann Hematol* **85**, 98-99 (2006).
- 94 Kratz, F. Albumin as a drug carrier: Design of prodrugs, drug conjugates and nanoparticles. *J Control Release* **132**, 171-183, doi:Doi 10.1016/J.Jconrel.2008.05.010 (2008).
- 95 Desai, N. T., C.: Yang, A.; Louie, L.; Yao, Z.; Soon-Shiong, P.; Magdassi, S. Protein Stabilized Pharmacologically Active Agents, Methods for the Preparation Thereof and Methods for the Use Thereof. US6749868 (2004).
- 96 Szuts, E. Z. & Harosi, F. I. Solubility of Retinoids in Water. *Arch Biochem Biophys* **287**, 297-304, doi:Doi 10.1016/0003-9861(91)90482-X (1991).
- 97 Anand, U. & Mukherjee, S. Binding, unfolding and refolding dynamics of serum albumins. *Bba-Gen Subjects* **1830**, 5394-5404, doi:Doi 10.1016/J.Bbagen.2013.05.017 (2013).
- 98 Michnik, A., Michalik, K. & Drzazga, Z. Stability of bovine serum albumin at different pH. *J Therm Anal Calorim* **80**, 399-406, doi:Doi 10.1007/S10973-005-0667-9 (2005).
- 99 Muzammil, S., Kumar, Y. & Tayyab, S. Molten globule-like state of human serum albumin at low pH. *Eur J Biochem* **266**, 26-32, doi:Doi 10.1046/J.1432-1327.1999.00810.X (1999).
- 100 Huai, Q., He, Y. L., Sheng, F. L. & Tao, Z. Y. Effects of pH and metal ions on the conformation of bovine serum albumin in aqueous solution - An Attenuated Total Reflection (ATR) FTIR Spectroscopic study. *Spectrochim Acta A* **52**, 1795-1800 (1996).

- 101 Sadler, P. J. & Tucker, A. Ph-Induced Structural Transitions of Bovine Serum-Albumin - Histidine Pka Values and Unfolding of the N-Terminus during the N to F Transition. *Eur J Biochem* **212**, 811-817, doi:Doi 10.1111/J.1432-1033.1993.Tb17722.X (1993).
- 102 Bloomfie.V. Structure of Bovine Serum Albumin at Low Ph. *Biochemistry-US* **5**, 684-&, doi:Doi 10.1021/Bi00866a039 (1966).
- 103 Foster, J. F. *Albumin Structure, Function and Uses.* 53-84 (Pergamon, 1977).
- 104 Carson, M. Ribbon Models of Macromolecules. *J Mol Graphics* **5**, 103-&, doi:Doi 10.1016/0263-7855(87)80010-3 (1987).
- 105 Carson, M. & Bugg, C. E. Algorithm for Ribbon Models of Proteins. *J Mol Graphics* **4**, 121-&, doi:Doi 10.1016/0263-7855(86)80010-8 (1986).
- 106 Era, S., Sogami, M., Kuata, K., et al. H-1-NMR Studies on Cross-Relaxation Phenomena in Bovine Mercaptalbumin (BMA) Solution and Partially Hydrolyzed Bovine Plasma-Albumin (BPA-STAR) Gel. *Int J Pept Prot Res* **33**, 214-222 (1989).
- 107 Brahma, A., Mandal, C. & Bhattacharyya, D. Characterization of a dimeric unfolding intermediate of bovine serum albumin under mildly acidic condition. *Bba-Proteins Proteom* **1751**, 159-169, doi:Doi 10.1016/J.Bbapap.2005.06.007 (2005).
- 108 Aoki, K., Nagaoka, S. Conformational change of Bovine Serum-Albumin Induced by 0.10 M TRIS-EDTA-BORIC Acid Buffer at pH 9. *Biochim Biophys Acta* **328**, 334-337 (1973).
- 109 Katchalski, E., Benjamin, G.S., Gross, V. The Availability of the Disulphide Bonds of Human and Bovine Serum Albumin and of Bovine Gamma-Globulin to Reduction by Thioglycolic Acid. *J Am Chem Soc* **79**, 4096-4099 (1957).
- 110 Estey, T., Kang, J., Schwendeman, S. P. & Carpenter, J. F. BSA degradation under acidic conditions: A model for protein instability during release from PLGA delivery systems. *J Pharm Sci-US* **95**, 1626-1639, doi:Doi 10.1002/Jps.20625 (2006).

- 111 Giancola, C., DeSena, C., Fessas, D., Graziano, G. & Barone, G. DSC studies on bovine serum albumin denaturation - Effects of ionic strength and SDS concentration. *Int J Biol Macromol* **20**, 193-204 (1997).
- 112 Yamasaki, M., Yano, H. & Aoki, K. Differential Scanning Calorimetric Studies on Bovine Serum-Albumin .1. Effects of Ph and Ionic-Strength. *Int J Biol Macromol* **12**, 263-268 (1990).
- 113 Kazitzina, S. Y. & Sochava, I. V. Scanning Calorimetry Development of Structural Transitions of Bovine Serum-Albumin. *Biofizika+* **35**, 212-216 (1990).
- 114 Murayama, K. & Tomida, M. Heat-induced secondary structure and conformation change of bovine serum albumin investigated by Fourier transform infrared spectroscopy. *Biochemistry-US* **43**, 11526-11532, doi:Doi 10.1021/Bi0489154 (2004).
- 115 Vetri, V., Librizzi, F., Leone, M. & Militello, V. Thermal aggregation of bovine serum albumin at different pH: comparison with human serum albumin. *Eur Biophys J Biophys* **36**, 717-725, doi:Doi 10.1007/S00249-007-0196-5 (2007).
- 116 Militello, V. *et al.* Aggregation kinetics of bovine serum albumin studied by FTIR spectroscopy and light scattering. *Biophys Chem* **107**, 175-187, doi:Doi 10.1016/J.Bpc.2003.09.004 (2004).
- 117 San Biagio, P. L. *et al.* Interacting processes in protein coagulation. *Proteins-Structure Function and Genetics* **37**, 116-120 (1999).
- 118 SanBiagio, P. L., Bulone, D., Emanuele, A. & Palma, M. U. Self-assembly of biopolymeric structures below the threshold of random cross-link percolation. *Biophys J* **70**, 494-499 (1996).
- 119 Tanaka, H. & Nishikawa, Y. Viscoelastic phase separation of protein solutions. *Phys Rev Lett* **95**, -, doi:Artn 078103  
Doi 10.1103/Physrevlett.95.078103 (2005).
- 120 Bulone, D., Martorana, V. & San Biagio, P. L. Effects of intermediates on aggregation of native bovine serum albumin. *Biophys Chem* **91**, 61-69 (2001).

- 121 Manno, M., San Biagio, P. L. & Palma, M. U. The role of pH on instability and aggregation of sickle hemoglobin solutions. *Proteins* **55**, 169-176, doi:Doi 10.1002/Prot.10648 (2004).
- 122 Clark, A. H., Judge, F. J., Richards, J. B., Stubbs, J. M. & Suggett, A. Electron-Microscopy of Network Structures in Thermally-Induced Globular Protein Gels. *Int J Pept Prot Res* **17**, 380-392 (1981).
- 123 Veerman, C., Sagis, L. M. C., Heck, J. & van der Linden, E. Mesostructure of fibrillar bovine serum albumin gels. *Int J Biol Macromol* **31**, 139-146, doi:Pii S0141-8130(02)00074-0 (2003).
- 124 Boye, J. I., Kalab, M., Alli, I. & Ma, C. Y. Microstructural properties of heat-set whey protein gels: Effect of pH. *Lebensm-Wiss Technol* **33**, 165-172, doi:Doi 10.1006/Fstl.2000.0646 (2000).
- 125 Weijers, M., Sagis, L. M. C., Veerman, C., Sperber, B. & van der Linden, E. Rheology and structure of ovalbumin gels at low pH and low ionic strength. *Food Hydrocolloid* **16**, 269-276, doi:Pii S0268-005x(01)00097-2 (2002).
- 126 Lefebvre, J., Renard, D. & Sanchez-Gimeno, A. C. Structure and rheology of heat-set gels of globular proteins - I. Bovine serum albumin gels in isoelectric conditions. *Rheol Acta* **37**, 345-357 (1998).
- 127 Haque, Z. Z. & Aryana, K. J. Effect of copper, iron, zinc and magnesium ions on bovine serum albumin gelation. *Food Sci Technol Res* **8**, 1-3 (2002).
- 128 Renard, D. & Lefebvre, J. Gelation of Globular-Proteins - Effect of Ph and Ionic-Strength on the Critical Concentration for Gel Formation - a Simple-Model and Its Application to Beta-Lactoglobulin Heat-Induced Gelation. *Int J Biol Macromol* **14**, 287-291 (1992).
- 129 Koseki, T., Kitabatake, N. & Doi, E. Irreversible thermal denaturation and formation of linear aggregates of ovalbumin. *Food Hydrocolloid* **3**, 123-134 (1989).
- 130 Richardson, R. K. & Rossmurphy, S. B. Mechanical-Properties of Globular Protein Gels .1. Incipient Gelation Behavior. *Int J Biol Macromol* **3**, 315-322 (1981).

- 131 Park, H. Y., Song, I. H., Kim, J. H. & Kim, W. S. Preparation of thermally denatured albumin gel and its pH-sensitive swelling. *Int J Pharm* **175**, 231-236 (1998).
- 132 Kolthoff, I. M., Anastasi, A. & Tan, B. H. Reactivity of Sulphydryl and Disulfide in Proteins .5. Reversal of Denaturation of Bovine Serum Albumin in 4-M Guanidine Hydrochloride or 8-M Urea and of Splitting of Disulfide Groups in 4-M Ghcl. *J Am Chem Soc* **82**, 4147-4151 (1960).
- 133 Chmelik, J., Anzenbacher, P., Chmelikova, J., Matejckova, M. & Kalous, V. Mechanism of Denaturation of Human-Serum Albumin by Urea. *Collect Czech Chem C* **53**, 411-422 (1988).
- 134 Maurer, P. H. Modified Bovine Serum Albumin .6. Immunochemical and Physicochemical Properties of Bovine Serum Albumin Denatured by Various Agents. *Arch Biochem Biophys* **79**, 13-26 (1959).
- 135 Rosenberg, R. M., Rogers, D. W., Steck, T. L. & Haebig, J. E. Interaction of Serum Albumin with Ethanol. *Arch Biochem Biophys* **97**, 433-& (1962).
- 136 Iemma, F. *et al.* Synthesis and release profile analysis of thermo-sensitive albumin hydrogels. *Colloid Polym Sci* **287**, 779-787, doi:Doi 10.1007/S00396-009-2027-Y (2009).
- 137 Iemma, F. *et al.* pH-Sensitive hydrogels based on bovine serum albumin for oral drug delivery. *Int J Pharm* **312**, 151-157, doi:Doi 10.1016/J.IJpharm.2006.01.010 (2006).
- 138 Iemma, F. *et al.* Spherical hydrophilic microparticles obtained by the radical copolymerisation of functionalised bovine serum albumin. *Colloid Polym Sci* **283**, 250-256, doi:Doi 10.1007/S00396-004-1071-X (2004).
- 139 Tsai, Y. M. *Characterization of Novel Self-Assembling Albumin Hydrogels* Masters thesis, Northwestern University, (2009).
- 140 Barnhart, J. L. *et al.* Albunex Microsphere Shells, the Unique Feature of a New Ultrasound Contrast Agent. *Int Congr Ser* **976**, 147-155 (1991).

- 141 Klein, A. L. *et al.* Delivery Techniques of Albunex to Monitor Myocardial Perfusion - Intracoronary Vs Aortic Root - Hand Vs Power. *Circulation* **86**, 573-573 (1992).
- 142 Christiansen, C., Kryvi, H., Sontum, P. C. & Skotland, T. Physical and Biochemical-Characterization of Albunex(Tm), a New Ultrasound Contrast Agent Consisting of Air-Filled Albumin Microspheres Suspended in a Solution of Human Albumin. *Biotechnol Appl Bioc* **19**, 307-320 (1994).
- 143 Christiansen, C. *et al.* Lack of an Immune-Response to Albunex(R), a New Ultrasound Contrast Agent Based on Air-Filled Albumin Microspheres. *Int Arch Allergy Imm* **104**, 372-378 (1994).
- 144 Rubino, O. P., Kowalsky, R. & Swarbrick, J. Albumin Microspheres as a Drug-Delivery System - Relation among Turbidity Ratio, Degree of Cross-Linking, and Drug-Release. *Pharmaceut Res* **10**, 1059-1065 (1993).
- 145 Sheu, M. T. & Sokoloski, T. D. Entrapment of Bioactive Compounds within Native Albumin Beads .4. Characterization of Drug Release from Polydisperse Systems. *Int J Pharm* **71**, 7-18 (1991).
- 146 Pande, S., Vyas, S. P. & Dixit, V. K. Localized Rifampicin Albumin Microspheres. *J Microencapsul* **8**, 87-93 (1991).
- 147 Cassidy, J., Poole, C., Sharkie, E., Steward, W. P. & Kaye, S. B. The Importance of Added Albumin during Continuous Intravenous-Infusion of Interleukin-2 with Alpha-Interferon. *Eur J Cancer* **27**, 1633-1634 (1991).
- 148 Sugio, S., Kashima, A., Mochizuki, S., Noda, M. & Kobayashi, K. Crystal structure of human serum albumin at 2.5 angstrom resolution. *Protein Eng* **12**, 439-446 (1999).
- 149 Bujacz, A. Structures of bovine, equine and leporine serum albumin. *Acta Crystallogr D* **68**, 1278-1289, doi:Doi 10.1107/S0907444912027047 (2012).
- 150 El Kadi, N. *et al.* Unfolding and refolding of bovine serum albumin at acid pH: ultrasound and structural studies. *Biophys J*, 402A-402A (2007).

- 151 Dockal, M., Carter, D. C. & Ruker, F. Conformational transitions of the three recombinant domains of human serum albumin depending on pH. *J Biol Chem* **275**, 3042-3050, doi:Doi 10.1074/jbc.275.5.3042 (2000).
- 152 Galantini, L., Leggio, C. & Pavel, N. V. Human Serum Albumin Unfolding: A Small-Angle X-ray Scattering and Light Scattering Study. *J Phys Chem B* **112**, 15460-15469, doi:Doi 10.1021/jp806821e (2008).
- 153 Nielsen, M., Lundsgaard, C., Lund, O., Petersen, T.N. CpHModels-3.0. Remote homology modeling using structure guided profile sequence alignment and double-sided baseline corrected scoring scheme. *Abstract at the CASP8 Conference* **193** (2008).
- 154 Nielsen, M., Lundsgaard, C., Lund, O., Petersen, T.N. CPHmodels-3.0 - Remote homology modeling using structure guided sequence profiles. *Nucl. Acids Res.* **38**, doi:10.1093/nar/gkq535 (2010).
- 155 Vorobjev, Y. N., Vila, J. A. & Scheraga, H. A. FAMBE-pH: A fast and accurate method to compute the total solvation free energies of proteins. *J Phys Chem B* **112**, 11122-11136, doi:Doi 10.1021/jp709969n (2008).
- 156 Vorobjev, Y. N. Advances in Implicit Models of Water Solvent to Compute Conformational Free Energy and Molecular Dynamics of Proteins at Constant Ph. *Adv Protein Chem Str* **85**, 281-322, doi:Doi 10.1016/B978-0-12-386485-7.00008-9 (2011).
- 157 Berendsen, H. J., Van Gunsteren, W. F., Zwinderman, H. R. & Geurtsen, R. G. Simulations of proteins in water. *Ann N Y Acad Sci* **482**, 269-286 (1986).
- 158 Berendsen, H. J. C., Vandervelpen, D. & Vandrunen, R. Gromacs - a Message-Passing Parallel Molecular-Dynamics Implementation. *Comput Phys Commun* **91**, 43-56 (1995).
- 159 Hess, B., Kutzner, C., van der Spoel, D. & Lindahl, E. GROMACS 4: Algorithms for highly efficient, load-balanced, and scalable molecular simulation. *J Chem Theory Comput* **4**, 435-447, doi:Doi 10.1021/Ct700301q (2008).
- 160 Lindahl, E., Hess, B. & Van Der Spoel, D. GROMACS 3.0: a package for molecular simulation and trajectory analysis. *J Mol Model* **7**, 306-317 (2001).

- 161 Van der Spoel, D. *et al.* Gromacs: Fast, Flexible, and Free. *J Comput Chem* **26**, 1701-1718, doi:Doi 10.1002/Jcc.20291 (2005).
- 162 Jorgensen, W. L., Maxwell, D. S. & TiradoRives, J. Development and testing of the OPLS all-atom force field on conformational energetics and properties of organic liquids. *J Am Chem Soc* **118**, 11225-11236 (1996).
- 163 Heinig, M. & Frishman, D. STRIDE: a web server for secondary structure assignment from known atomic coordinates of proteins. *Nucleic Acids Res* **32**, W500-W502, doi:Doi 10.1093/Nar/Gkh429 (2004).
- 164 Sereda, T. J., Mant, C. T., Sonnichsen, F. D. & Hodges, R. S. Reversed-Phase Chromatography of Synthetic Amphipathic Alpha-Helical Peptides as a Model for Ligand/Receptor Interactions Effect of Changing Hydrophobic Environment on the Relative Hydrophilicity/Hydrophobicity of Amino-Acid Side-Chains. *J Chromatogr A* **676**, 139-153, doi:Doi 10.1016/0021-9673(94)00371-8 (1994).
- 165 Baker, N. A., Sept, D., Joseph, S., Holst, M. J. & McCammon, J. A. Electrostatics of nanosystems: Application to microtubules and the ribosome. *P Natl Acad Sci USA* **98**, 10037-10041, doi:Doi 10.1073/Pnas.181342398 (2001).
- 166 Pettersen, E. F. *et al.* UCSF chimera - A visualization system for exploratory research and analysis. *J Comput Chem* **25**, 1605-1612, doi:Doi 10.1002/Jcc.20084 (2004).
- 167 Humphrey, W., Dalke, A. & Schulten, K. VMD: Visual molecular dynamics. *J Mol Graph Model* **14**, 33-38, doi:Doi 10.1016/0263-7855(96)00018-5 (1996).
- 168 Tanford, C., Buzzell, J. G., Rands, D. G. & Swanson, S. A. The Reversible Expansion of Bovine Serum Albumin in Acid Solutions. *J Am Chem Soc* **77**, 6421-6428, doi:Doi 10.1021/Ja01629a003 (1955).
- 169 Geisow, M. J. & Beaven, G. H. Physical and Binding Properties of Large Fragments of Human-Serum Albumin. *Biochem J* **163**, 477-484 (1977).
- 170 Khan, M. Y. Direct Evidence for the Involvement of Domain-Iii in the N-F Transition of Bovine Serum-Albumin. *Biochem J* **236**, 307-310 (1986).

- 171 Chruszcz, M. *et al.* Serum albumins-Unusual allergens. *Bba-Gen Subjects* **1830**, 5375-5381, doi:Doi 10.1016/J.Bbagen.2013.06.016 (2013).
- 172 Majorek, K. A. *et al.* Structural and immunologic characterization of bovine, horse, and rabbit serum albumins. *Mol Immunol* **52**, 174-182, doi:Doi 10.1016/J.Molimm.2012.05.011 (2012).
- 173 Geisow, M. J. & Beaven, G. H. Large Fragments of Human-Serum Albumin. *Biochem J* **161**, 619-625 (1977).
- 174 Bhattacharya, M., Jain, N., Bhasne, K., Kumari, V. & Mukhopadhyay, S. pH-induced Conformational Isomerization of Bovine Serum Albumin Studied by Extrinsic and Intrinsic Protein Fluorescence. *J Fluoresc* **21**, 1083-1090, doi:Doi 10.1007/S10895-010-0781-3 (2011).
- 175 Bhattacharya, M., Jain, N. & Mukhopadhyay, S. Insights into the Mechanism of Aggregation and Fibril Formation from Bovine Serum Albumin. *J Phys Chem B* **115**, 4195-4205, doi:Doi 10.1021/Jp111528c (2011).
- 176 Yasuda, K., Nakamura, R. & Hayakawa, S. Factors Affecting Heat-Induced Gel Formation of Bovine Serum-Albumin. *J Food Sci* **51**, 1289-1292, doi:Doi 10.1111/J.1365-2621.1986.Tb13107.X (1986).
- 177 Matsudomi, N., Rector, D. & Kinsella, J. E. Gelation of Bovine Serum-Albumin and Beta-Lactoglobulin - Effects of Ph, Salts and Thiol Reagents. *Food Chem* **40**, 55-69 (1991).
- 178 Bellare, J. R., Davis, H. T., Scriven, L. E. & Talmon, Y. Controlled Environment Vitrification System - an Improved Sample Preparation Technique. *J Electron Micr Tech* **10**, 87-111, doi:Doi 10.1002/Jemt.1060100111 (1988).
- 179 Lin, W. C., Otim, K. J., Lenhart, J. L., Cole, P. J. & Shull, K. R. Indentation fracture of silicone gels. *J Mater Res* **24**, 957-965, doi:Doi 10.1557/Jmr.2009.0128 (2009).
- 180 Shull, K. R., Ahn, D., Chen, W. L., Flanigan, C. M. & Crosby, A. J. Axisymmetric adhesion tests of soft materials. *Macromol Chem Physic* **199**, 489-511 (1998).

- 181 Babcock, J. J. & Brancaleon, L. Bovine serum albumin oligomers in the E- and B-forms at low protein concentration and ionic strength. *Int J Biol Macromol* **53**, 42-53, doi:Doi 10.1016/J.Ijb biomac.2012.10.030 (2013).
- 182 Kongraksawech, T., Vazquez-Landaverde, P., Huerta-Ruelas, J. & Torres, J. A. Ionic strength and pH effects on optical thermographs for bovine serum albumin (BSA). *Cienc Tecnol Aliment* **5**, 259-264 (2007).
- 183 Alizadeh-Pasdar, N. & Li-Chan, E. C. Y. Comparison of protein surface hydrophobicity measured at various pH values using three different fluorescent probes. *J Agr Food Chem* **48**, 328-334, doi:Doi 10.1021/Jf990393p (2000).
- 184 Takeda, K., Wada, A., Yamamoto, K., Moriyama, Y. & Aoki, K. Conformational Change of Bovine Serum-Albumin by Heat-Treatment. *J Protein Chem* **8**, 653-659, doi:Doi 10.1007/Bf01025605 (1989).
- 185 Haskard, C. A. & Li-Chan, E. C. Y. Hydrophobicity of bovine serum albumin and ovalbumin determined using uncharged (PRODAN) and anionic (ANS(-)) fluorescent probes. *J Agr Food Chem* **46**, 2671-2677, doi:Doi 10.1021/Jf970876y (1998).
- 186 Clark, A. H., Kavanagh, G. M. & Ross-Murphy, S. B. Globular protein gelation - theory and experiment. *Food Hydrocolloid* **15**, 383-400 (2001).
- 187 Baler, K. *et al.* Electrostatic Unfolding and Interactions of Albumin Driven by pH Changes: A Molecular Dynamics Study. *J Phys Chem B* **118**, 921-930, doi:10.1021/jp409936v (2014).
- 188 Wells, R. G. The role of matrix stiffness in regulating cell behavior. *Hepatology* **47**, 1394-1400, doi:Doi 10.1002/Hep.22193 (2008).
- 189 Day, Y. S. N. & Myszka, D. G. Characterizing a drug's primary binding site on albumin. *J Pharm Sci-US* **92**, 333-343, doi:Doi 10.1002/Jps.10293 (2003).
- 190 Ahmad, B., Parveen, S. & Khan, R. H. Effect of albumin conformation on the binding of ciprofloxacin to human serum albumin: A novel approach directly assigning binding site. *Biomacromolecules* **7**, 1350-1356, doi:Doi 10.1021/Bm050996b (2006).

- 191 Abou-Zied, O. K. & Al-Shihi, O. I. K. Characterization of subdomain IIA binding site of human serum albumin in its native, unfolded, and refolded states using small molecular probes. *J Am Chem Soc* **130**, 10793-10801, doi:Doi 10.1021/Ja8031289 (2008).
- 192 Lohner, K., Sen, A. C., Pranker, R., Esser, A. F. & Perrin, J. H. Effects of Drug-Binding on the Thermal-Denaturation of Human Serum-Albumin. *J Pharmaceut Biomed* **12**, 1501-1505, doi:Doi 10.1016/0731-7085(94)00094-8 (1994).
- 193 Sulkowska, A., Bojko, B., Rownicka, J., Pentak, D. & Sulkowski, W. Effect of urea on serum albumin complex with antithyroid drugs: fluorescence study. *J Mol Struct* **651**, 237-243, doi:Pii S0022-2860(02)00635-X  
Doi 10.1016/S0022-2860(02)00635-X (2003).
- 194 Varshney, A. *et al.* Ligand Binding Strategies of Human Serum Albumin: How Can the Cargo be Utilized? *Chirality* **22**, 77-87, doi:Doi 10.1002/Chir.20709 (2010).
- 195 Yadav, R. & Sen, P. Mechanistic investigation of domain specific unfolding of human serum albumin and the effect of sucrose. *Protein Sci* **22**, 1571-1581, doi:Doi 10.1002/Pro.2357 (2013).
- 196 Baier, S. K. & McClements, D. J. Combined influence of NaCl and sucrose on heat-induced gelation of bovine serum albumin. *J Agr Food Chem* **51**, 8107-8112, doi:Doi 10.1021/Jf034249m (2003).
- 197 Baier, S. K. & McClements, D. J. Impact of sorbitol on the thermostability and heat-induced gelation of bovine serum albumin. *Food Res Int* **36**, 1081-1087, doi:Doi 10.1016/J.Foodres.2003.09.003 (2003).
- 198 Hamilton, J. A., Era, S., Bhamidipati, S. P. & Reed, R. G. Locations of the 3 Primary Binding-Sites for Long-Chain Fatty-Acids on Bovine Serum-Albumin. *P Natl Acad Sci USA* **88**, 2051-2054 (1991).
- 199 Torrie, G. M. & Valleau, J. P. Monte-Carlo Free-Energy Estimates Using Non-Boltzmann Sampling - Application to Subcritical Lennard-Jones Fluid. *Chemical Physics Letters* **28**, 578-581, doi:Doi 10.1016/0009-2614(74)80109-0 (1974).

- 200 Hub, J. S., de Groot, B. L. & van der Spoel, D. g\_wham-A Free Weighted Histogram Analysis Implementation Including Robust Error and Autocorrelation Estimates. *J Chem Theory Comput* **6**, 3713-3720, doi:Doi 10.1021/Ct100494z (2010).
- 201 Ghuman, J. *et al.* Structural basis of the drug-binding specificity of human serum albumin. *J Mol Biol* **353**, 38-52, doi:Doi 10.1016/J.Jmb.2005.07.075 (2005).
- 202 Sudlow, G., Birkett, D. J. & Wade, D. N. Characterization of 2 Specific Drug Binding-Sites on Human-Serum Albumin. *Mol Pharmacol* **11**, 824-832 (1975).
- 203 He, Y. *et al.* Large-scale production of functional human serum albumin from transgenic rice seeds. *P Natl Acad Sci USA* **108**, 19078-19083, doi:Doi 10.1073/Pnas.1109736108 (2011).
- 204 Zhang, Q., Yu, H., Zhang, F. Z. & Shen, Z. C. Expression and purification of recombinant human serum albumin from selectively terminable transgenic rice. *J Zhejiang Univ-Sc B* **14**, 867-874, doi:Doi 10.1631/Jzus.B1300090 (2013).
- 205 Chen, Z., He, Y., Shi, B. & Yang, D. C. Human serum albumin from recombinant DNA technology: Challenges and strategies. *Bba-Gen Subjects* **1830**, 5515-5525, doi:Doi 10.1016/J.Bbagen.2013.04.037 (2013).
- 206 Malleda, C., Ahalawat, N., Gokara, M. & Subramanyam, R. Molecular dynamics simulation studies of betulinic acid with human serum albumin. *J Mol Model* **18**, 2589-2597, doi:Doi 10.1007/S00894-011-1287-X (2012).

## Appendix

### 8.1 Appendix A: Python script to calculate electrostatic surface potential

```

import math
import datetime
import sys
from decimal import *

__author__="galibaler"
__date__ =str(datetime.datetime.now())

title = '***\n Electrostatic Potential Summation\n version 4\n' + __date__ +
'\n***\n'
print title
inputpdb = raw_input("What is the name of the PDB file to analyze? ")
outputpdb = "OUT" + inputpdb
input = open(inputpdb, "r")
fout = open(outputpdb, "w")
atoms = 0
cutoff = 100.0 #Cutoff distance for atoms included in calculation
r = 0
master = []
xdim = 0
ydim = 0
zdim = 0

fout.write(title)

#This is the initial loop which collects all the x, y, z, and charge q values
for every atom into the master list for analysis
for line in input:
    if line[0:4]=='ATOM':
        res = line[17:21]
        atom = line[13:14]
        if atom != 'C' and atom != 'H' and atom != 'O' and atom != 'N' and atom
!= 'S' and res != 'DOT ':
            atom = 'H'
        x = float(line[31:38])
        y = float(line[39:46])
        z = float(line[47:54])
        q = float(line[61:66])
        list = [x,y,z,q,res,atom]
        atoms = atoms + 1
        master.append(list)
    elif line[0:4]=='CRYSTAL':
        xdim = float(line[7:15])
        ydim = float(line[15:24])
        zdim = float(line[24:33])

#This is the first level loop which runs over all the atom/dot entries in the

```

```

system
i = 0
input = open(inputpdb, "r")
for line in input:
    if line[0:4]!='ATOM':
        print line[0:69],
        fout.write(line[0:69])
    if line[0:4]=='ATOM':
        j = 0
        atomsum = 0
        neighbor = 0
        x1 = master[i][0]
        y1 = master[i][1]
        z1 = master[i][2]
        q1 = master[i][3]
        if master[i][4] == 'DOT ': #Check to see if atom is Connolly surface
            while j < atoms: #This is the second level loop taking an single
Connolly dot and analyzing all entries within the cutoff distance
            if master[j][4] != 'DOT ': #Avoid other surface points
                x2 = master[j][0]
                x2a = x2 + xdim
                x2b = x2 - xdim
                y2 = master[j][1]
                y2a = y2 + ydim
                y2b = y2 - ydim
                z2 = master[j][2]
                z2a = z2 + zdim
                z2b = z2 - zdim
                q2 = master[j][3]
                sdx1 = (x1-x2)*(x1-x2)
                sdx2 = (x1-x2a)*(x1-x2a)
                sdx3 = (x1-x2b)*(x1-x2b)
                sdyl = (y1-y2)*(y1-y2)
                sdya = (y1-y2a)*(y1-y2a)
                sdyb = (y1-y2b)*(y1-y2b)
                sdz1 = (z1-z2)*(z1-z2)
                sdza = (z1-z2a)*(z1-z2a)
                sdzb = (z1-z2b)*(z1-z2b)
                r0 = sdx1 + sdyl + sdz1
                rxa = sdx2 + sdyl + sdz1
                rxb = sdx3 + sdyl + sdz1
                rya = sdx1 + sdya + sdz1
                ryb = sdx1 + sdyb + sdz1
                rza = sdx1 + sdyl + sdza
                rzb = sdx1 + sdyl + sdzb
                r = [r0, rxa, rxb, rya, ryb, rza, rzb]
                if min(r) != 0:
                    excludedvolume = 0
                    if master[j][5] == 'C' and master[j][4] != 'CL- ':
                        excludedvolume = excludedvolume + 0.85
                    if master[j][5] == 'C' and master[j][4] == 'CL- ':
                        excludedvolume = excludedvolume + 0.875
                    if master[j][5] == 'H':
                        excludedvolume = excludedvolume + 0.5

```

```
if master[j][5] == 'O':
    excludedvolume = excludedvolume + 0.75
if master[j][5] == 'N':
    excludedvolume = excludedvolume + 0.8
if master[j][5] == 'S':
    excludedvolume = excludedvolume + 0.9
if min(r) >= excludedvolume and min(r) <= cutoff:
    neighbor = neighbor + 1
    atomsum = atomsum + q2/math.sqrt(min(r))
    print "interaction", i+1, "-", master[i][4],
"x", j+1, "-", master[j][4], 'q2', q2, ' r', min(r), "sum =", atomsum
    j = j + 1
#       print i, "neighbors =", neighbor, "atompot =", atomsum, "total
potsum =", potsum
#       print atomsum, "issurface", issurface
if atomsum < 0:
    string = '-##[0:2.2f]##-'.format(atomsum)
else:
    string = ' -##[0:2.2f]##-'.format(atomsum)
print line[0:55] + string + ' 2.00'
fout.write(line[0:55] + string + ' 2.00' + '\n')
else:
    print line[0:69],
    fout.write(line[0:69])
i = i + 1

#       print i, '/', atoms
fout.close()
```

## 8.2 Appendix B: Interspecies homology of serum albumins

**Table 8.1 Sequence identity and similarity between 18 different mammalian and avian serum albumins.** Sequence identity (blue) and similarity (red) are shown where higher percentages correspond to darker shading<sup>171</sup>.

	Similarity (%)								
	Human	Bovine	Cat	Dog	Donkey	Horse	Pig	Goat	Sheep
Identity (%)	Human	100.0	85.5	85.5	85.5	85.5	85.5	85.5	85.5
	Bovine	75.6	100.0	87.7	87.2	83.5	83.4	87.1	96.1
	Cat	81.7	77.7	100.0	92.8	86.3	85.6	87.2	87.8
	Dog	79.8	76.0	87.0	100.0	86.0	85.3	86.5	88.4
	Donkey	76.4	73.8	77.9	76.0	100.0	99.0	84.6	84.0
	Horse	76.1	73.9	77.6	75.7	98.6	100.0	83.9	84.2
	Pig	74.9	79.2	78.9	77.7	76.3	75.8	100.0	86.1
	Goat	74.5	92.1	76.4	77.6	75.1	75.1	77.7	100.0
	Sheep	74.7	92.1	76.7	77.6	75.5	75.5	77.5	98.5
	Rabbit	74.2	71.2	75.3	74.3	70.5	70.5	73.1	72.1
	Guinea pig	72.0	69.7	75.7	73.3	72.1	71.7	72.3	70.5
	Hamster	76.1	69.9	76.7	74.0	75.3	75.3	72.6	70.0
	Mouse	72.1	69.5	73.5	71.9	71.4	71.2	70.2	69.2
	Rat	73.2	70.0	75.2	72.9	72.4	72.4	72.3	69.7
	Chicken	46.1	43.2	45.1	45.8	42.7	42.7	41.9	43.4
	Duck	48.6	45.3	47.5	47.9	45.2	45.0	44.1	45.5
	Pigeon	46.5	43.5	45.7	46.5	44.1	44.1	42.1	44.1
	Turkey	47.2	44.8	46.0	46.8	43.8	43.6	42.9	45.0
Identity (%)	Rabbit	85.5	85.5	85.5	85.5	85.5	61.1	63.3	62.0
	Bovine	83.7	80.8	81.3	79.6	80.5	58.8	60.6	59.6
	Cat	86.6	85.8	86.1	83.6	84.8	59.6	61.5	60.1
	Dog	86.0	84.4	85.1	82.9	84.8	60.1	62.3	61.8
	Donkey	83.4	83.4	84.8	81.7	83.6	57.8	60.4	58.9
	Horse	82.9	82.7	84.2	81.3	83.0	57.8	60.1	58.7
	Pig	83.9	82.7	82.5	81.0	82.4	58.3	60.3	58.7
	Goat	84.1	81.7	81.7	80.1	80.8	59.1	61.1	60.4
	Sheep	83.6	81.5	81.2	80.0	80.7	59.0	61.0	60.3
	Rabbit	100.0	83.2	85.4	82.2	82.5	60.0	63.0	62.0
	Guinea pig	71.4	100.0	85.4	83.2	84.4	58.1	60.4	59.6
	Hamster	73.6	75.7	100.0	89.9	92.0	58.6	61.1	60.4
	Mouse	71.7	73.5	82.7	100.0	95.2	58.6	61.3	60.1
	Rat	72.3	73.8	84.2	89.6	100.0	59.0	61.3	60.6
	Chicken	44.9	43.2	42.4	43.2	43.8	100.0	88.3	85.0
	Duck	48.4	45.8	45.8	46.7	46.9	84.5	100.0	90.2
	Pigeon	46.3	44.8	45.3	45.2	46.0	79.6	84.2	100.0
	Turkey	46.3	44.1	43.8	45.0	45.0	87.2	86.4	81.2

### 8.3 Appendix C: Change in denaturation temperature with pH

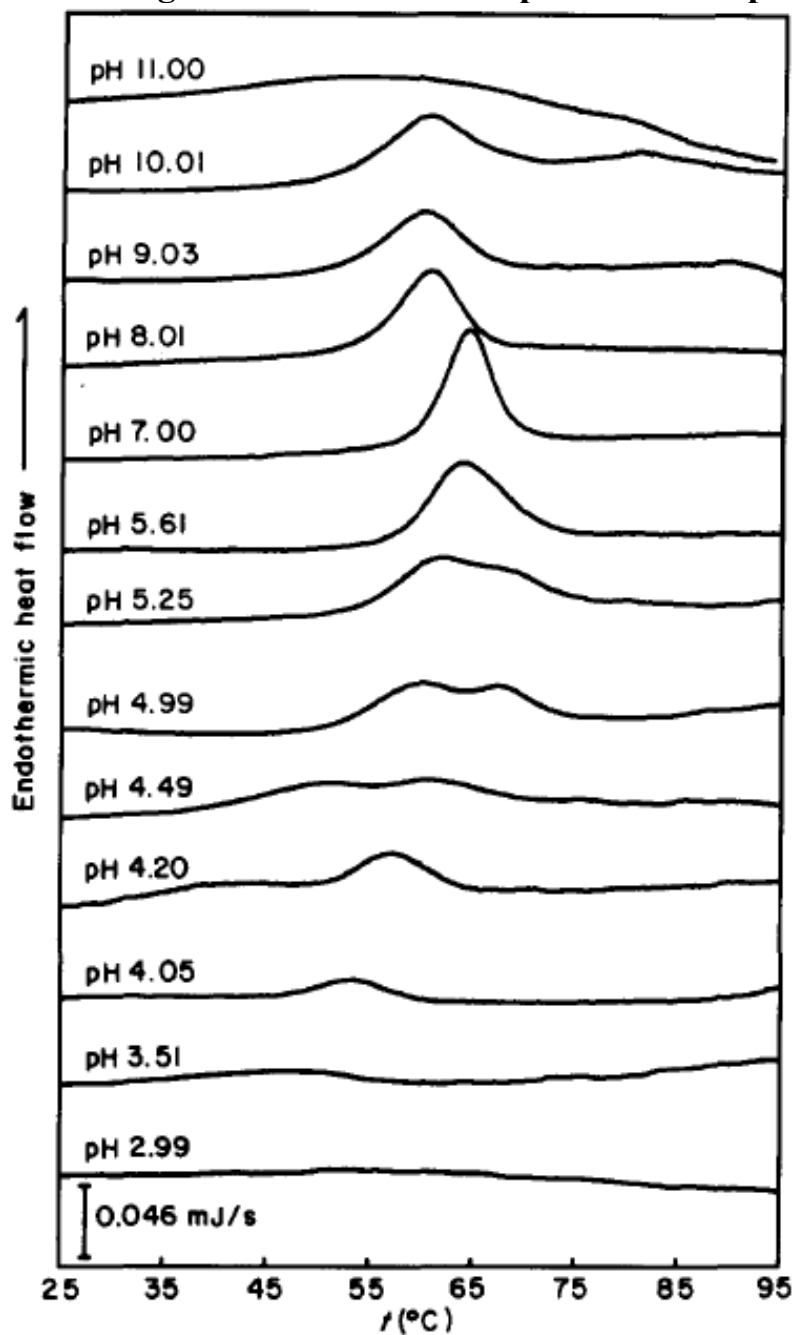


Figure 8.1 Shifting DSC curves of 2% BSA in 0.1 M NaCl at various pH values<sup>112</sup>.

## 8.4 Appendix D: PDB F-form Bovine Serum Albumin

TITLE Bovine Serum Albumin in F Isoform at pH 3.5  
 REMARK Please cite the following reference when using this work  
 REMARK Baler, K., et al. J. of Phys. Chem. B, 118(4), 921-930 (2014)  
 REMARK This file also includes 100 equilibrated chlorine ions  
 CRYST1 180.000 115.000 140.000 90.00 90.00 90.00 P 1 1  
 MODEL 1  
 ATOM 1 N ASP 1 84.830 21.680 38.020 1.00 0.00  
 ATOM 2 H1 ASP 1 84.860 22.740 37.910 1.00 0.00  
 ATOM 3 H2 ASP 1 84.820 21.320 37.130 1.00 0.00  
 ATOM 4 H3 ASP 1 83.940 21.460 38.510 1.00 0.00  
 ATOM 5 CA ASP 1 86.130 21.300 38.710 1.00 0.00  
 ATOM 6 HA ASP 1 85.970 20.230 38.940 1.00 0.00  
 ATOM 7 CB ASP 1 87.370 21.220 37.840 1.00 0.00  
 ATOM 8 HB1 ASP 1 88.200 20.790 38.420 1.00 0.00  
 ATOM 9 HB2 ASP 1 87.170 20.550 36.980 1.00 0.00  
 ATOM 10 CG ASP 1 87.950 22.590 37.360 1.00 0.00  
 ATOM 11 OD1 ASP 1 87.250 23.460 36.800 1.00 0.00  
 ATOM 12 OD2 ASP 1 89.310 22.630 37.450 1.00 0.00  
 ATOM 13 HD2 ASP 1 89.540 23.350 36.870 1.00 0.00  
 ATOM 14 C ASP 1 86.220 22.220 39.980 1.00 0.00  
 ATOM 15 O ASP 1 85.760 23.390 40.000 1.00 0.00  
 .... .. . .... . .... .... .... .... .... ....  
 .... .. . .... . .... .... .... .... .... ....  
 .... .. . .... . .... .... .... .... .... ....  
 ATOM 9325 N ALA 583 27.190 25.420 114.730 1.00 0.00  
 ATOM 9326 H ALA 583 26.230 25.110 114.540 1.00 0.00  
 ATOM 9327 CA ALA 583 28.040 25.150 113.600 1.00 0.00  
 ATOM 9328 HA ALA 583 29.130 25.080 113.740 1.00 0.00  
 ATOM 9329 CB ALA 583 27.410 23.890 112.980 1.00 0.00  
 ATOM 9330 HB1 ALA 583 26.400 23.950 112.600 1.00 0.00  
 ATOM 9331 HB2 ALA 583 28.100 23.480 112.280 1.00 0.00  
 ATOM 9332 HB3 ALA 583 27.360 23.100 113.760 1.00 0.00  
 ATOM 9333 C ALA 583 27.790 26.260 112.600 1.00 0.00  
 ATOM 9334 OT ALA 583 27.210 27.340 112.830 1.00 0.00  
 ATOM 9335 O ALA 583 28.400 25.990 111.410 1.00 0.00  
 ATOM 9336 HO ALA 583 28.500 26.730 110.790 1.00 0.00  
 TER  
 ENDMDL

## 8.5 Appendix E: Circular dichroism of albumin thermal denaturation.

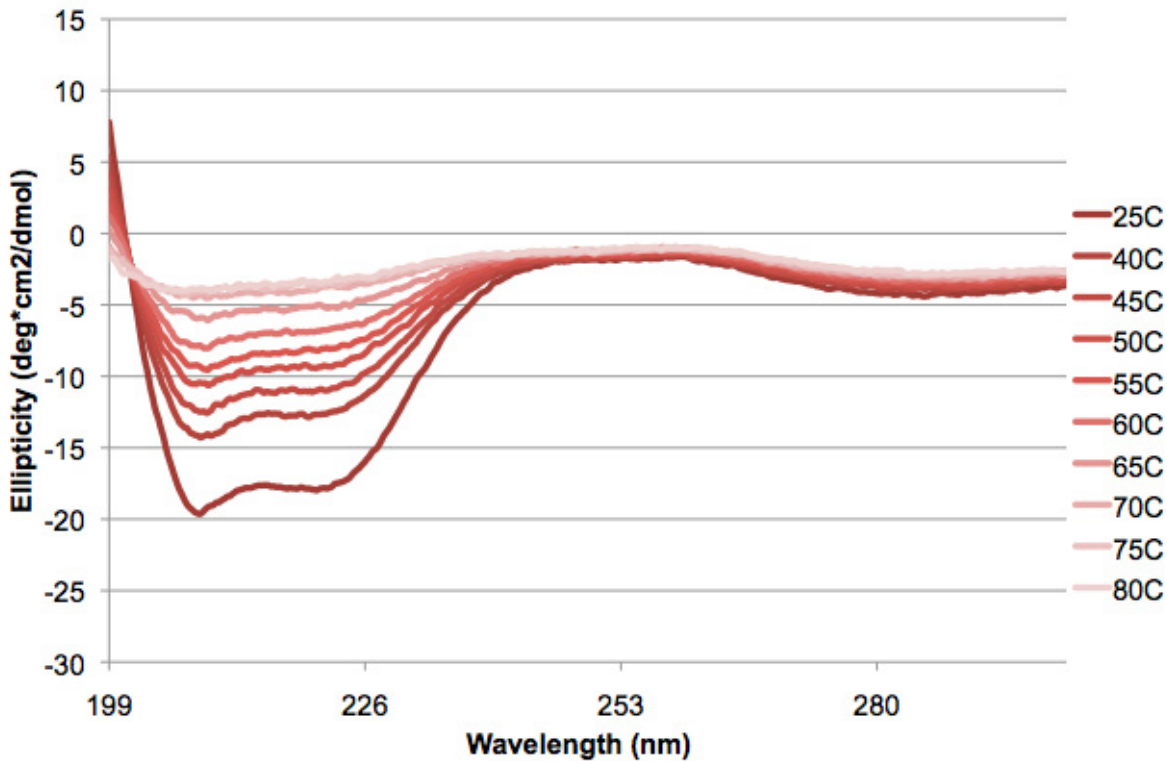


Figure 8.2 Circular Dichroism data of dilute solutions of BSA (0.005 wt%) at increasing temperature showing the loss of secondary structure during thermal denaturation.

## 8.6 Appendix G: Snapshots during atRA – F-form albumin binding simulation

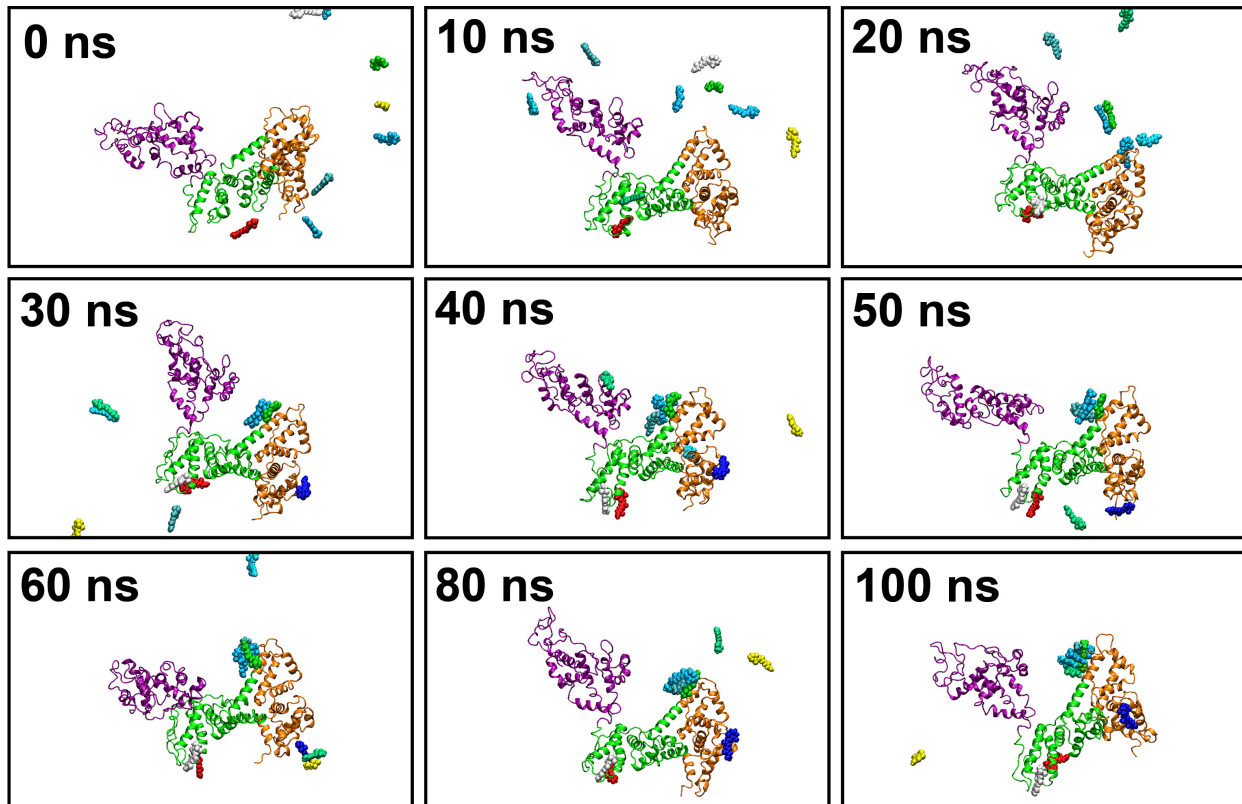


Figure 8.3 Snapshots of atRA binding to F-form albumin in fully atomistic MD simulations for 100ns. F-form albumin binding sites are located primarily in domain I (orange) and II (green). Clusters of atRA also formed aggregates on the protein surface.

## 8.7 Appendix H: Snapshots during atRA – N-form albumin binding simulation

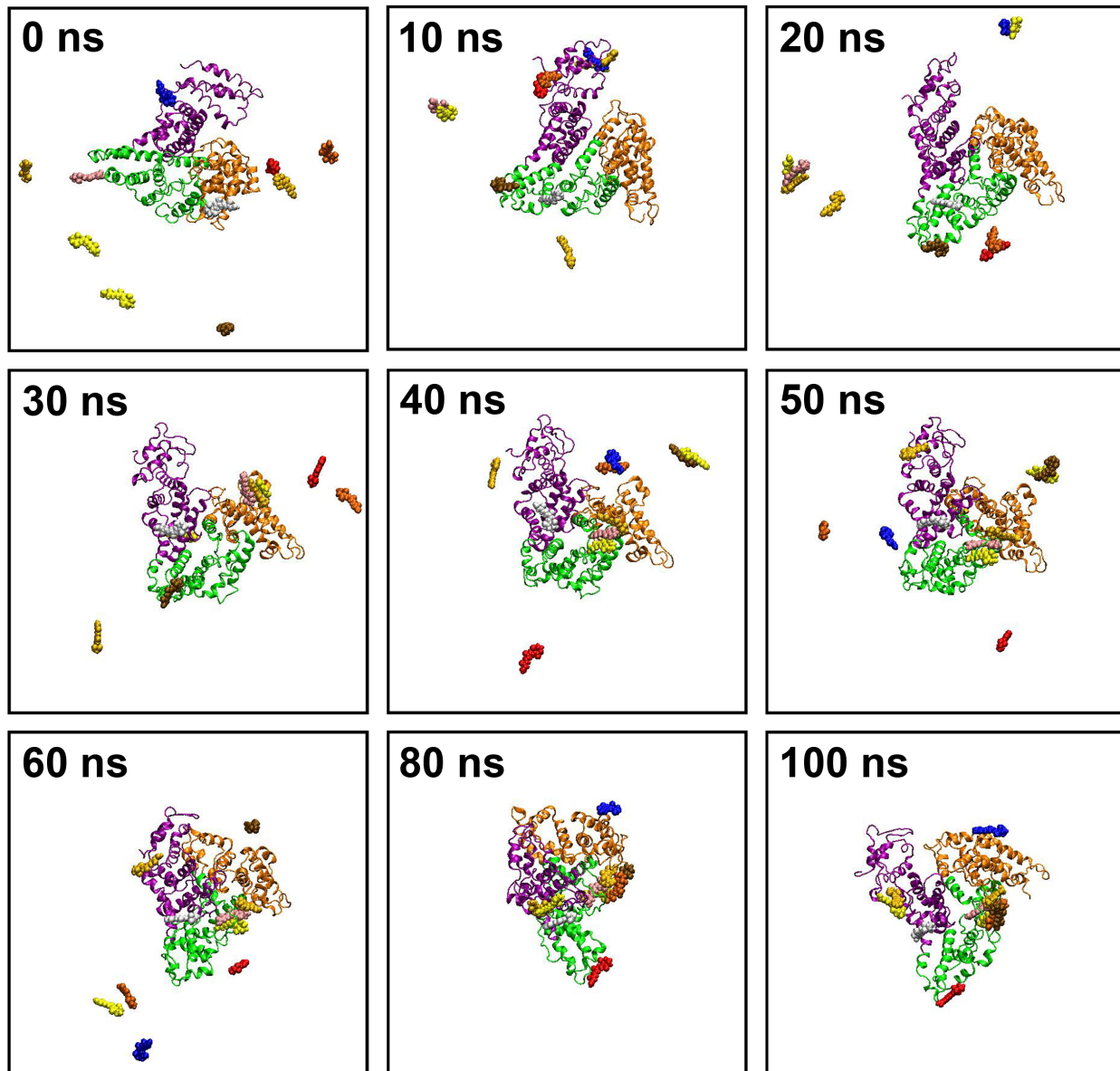


Figure 8.4 . Snapshots of atRA binding to N-form albumin in fully atomistic MD simulations for 100ns. N-form albumin binding sites are located in all three domains. Clusters of atRA also formed aggregates on the protein surface.